MASTER'S DEGREE IN INDUSTRIAL ENGINEERING

MASTER FINAL THESIS

CARAVACA II: ISLANDS WITH ENERGY STORAGE: INRUSH CURRENT

Autor: Gonzalo Tejero Calvo

Director: Jesús Varela Sanz

Co-Director: Lukas Sigrist

Madrid

Declaro, bajo mi responsabilidad, que el Proyecto presentado con el título

Caravaca II: Islands with Energy Storage: Inrush Current

en la ETS de Ingeniería - ICAI de la Universidad Pontificia Comillas en el

curso académico 2020/21 es de mi autoría, original e inédito y

no ha sido presentado con anterioridad a otros efectos.

El Proyecto no es plagio de otro, ni total ni parcialmente y la información que ha sido

tomada de otros documentos está debidamente referenciada.

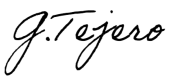

Fdo.: Gonzalo Tejero Calvo Fecha: 20/ 08/ 2021

Autorizada la entrega del proyecto

LOS DIRECTORES DEL PROYECTO

Fdo.: Jesús Varela Sanz Fecha: 20/ 08/ 2021

Fdo.: Lukas Sigrist Fecha: 20/ 08/ 2021

AUTORIZACIÓN PARA LA DIGITALIZACIÓN, DEPÓSITO Y DIVULGACIÓN EN RED DE PROYECTOS FIN DE GRADO, FIN DE MÁSTER, TESINAS O MEMORIAS DE BACHILLERATO

1º. Declaración de la autoría y acreditación de la misma.

El autor D Gonzalo Tejero Calvo

DECLARA ser el titular de los derechos de propiedad intelectual de la obra:

Caravaca II: Islands with Energy Storage: Inrush Current,

que ésta es una obra original, y que ostenta la condición de autor en el sentido que otorga la Ley de Propiedad Intelectual.

2º. Objeto y fines de la cesión.

Con el fin de dar la máxima difusión a la obra citada a través del Repositorio institucional de la Universidad, el autor **CEDE** a la Universidad Pontificia Comillas, de forma gratuita y no exclusiva, por el máximo plazo legal y con ámbito universal, los derechos de digitalización, de archivo, de reproducción, de distribución y de comunicación pública, incluido el derecho de puesta a disposición electrónica, tal y como se describen en la Ley de Propiedad Intelectual. El derecho de transformación se cede a los únicos efectos de lo dispuesto en la letra a) del apartado siguiente.

3º. Condiciones de la cesión y acceso

Sin perjuicio de la titularidad de la obra, que sigue correspondiendo a su autor, la cesión de derechos contemplada en esta licencia habilita para:

a) Transformarla con el fin de adaptarla a cualquier tecnología que permita incorporarla a internet y hacerla accesible; incorporar metadatos para realizar el registro de la obra e incorporar "marcas de agua" o cualquier otro sistema de seguridad o de protección.
b) Reproducirla en un soporte digital para su incorporación a una base de datos electrónica, incluyendo el derecho de reproducir y almacenar la obra en servidores, a los efectos de garantizar su seguridad, conservación y preservar el formato.
c) Comunicarla, por defecto, a través de un archivo institucional abierto, accesible de modo libre y gratuito a través de internet.
d) Cualquier otra forma de acceso (restringido, embargado, cerrado) deberá solicitarse expresamente y obedecer a causas justificadas.
e) Asignar por defecto a estos trabajos una licencia Creative Commons.
f) Asignar por defecto a estos trabajos un HANDLE (URL *persistente)*.

4º. Derechos del autor.

El autor, en tanto que titular de una obra tiene derecho a:

a) Que la Universidad identifique claramente su nombre como autor de la misma
b) Comunicar y dar publicidad a la obra en la versión que ceda y en otras posteriores a través de cualquier medio.
c) Solicitar la retirada de la obra del repositorio por causa justificada.
d) Recibir notificación fehaciente de cualquier reclamación que puedan formular terceras personas en relación con la obra y, en particular, de reclamaciones relativas a los derechos de propiedad intelectual sobre ella.

5º. Deberes del autor.

El autor se compromete a:

a) Garantizar que el compromiso que adquiere mediante el presente escrito no infringe ningún derecho de terceros, ya sean de propiedad industrial, intelectual o cualquier otro.
b) Garantizar que el contenido de las obras no atenta contra los derechos al honor, a la intimidad y a la imagen de terceros.
c) Asumir toda reclamación o responsabilidad, incluyendo las indemnizaciones por daños, que pudieran ejercitarse contra la Universidad por terceros que vieran infringidos sus derechos e intereses a causa de la cesión.

d) Asumir la responsabilidad en el caso de que las instituciones fueran condenadas por infracción de derechos derivada de las obras objeto de la cesión.

6º. Fines y funcionamiento del Repositorio Institucional.

La obra se pondrá a disposición de los usuarios para que hagan de ella un uso justo y respetuoso con los derechos del autor, según lo permitido por la legislación aplicable, y con fines de estudio, investigación, o cualquier otro fin lícito. Con dicha finalidad, la Universidad asume los siguientes deberes y se reserva las siguientes facultades:

- La Universidad informará a los usuarios del archivo sobre los usos permitidos, y no garantiza ni asume responsabilidad alguna por otras formas en que los usuarios hagan un uso posterior de las obras no conforme con la legislación vigente. El uso posterior, más allá de la copia privada, requerirá que se cite la fuente y se reconozca la autoría, que no se obtenga beneficio comercial, y que no se realicen obras derivadas.
- La Universidad no revisará el contenido de las obras, que en todo caso permanecerá bajo la responsabilidad exclusive del autor y no estará obligada a ejercitar acciones legales en nombre del autor en el supuesto de infracciones a derechos de propiedad intelectual derivados del depósito y archivo de las obras. El autor renuncia a cualquier reclamación frente a la Universidad por las formas no ajustadas a la legislación vigente en que los usuarios hagan uso de las obras.
- La Universidad adoptará las medidas necesarias para la preservación de la obra en un futuro.
- La Universidad se reserva la facultad de retirar la obra, previa notificación al autor, en supuestos suficientemente justificados, o en caso de reclamaciones de terceros.

Madrid, a 20 de Agosto de 2021

ACEPTA

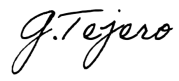

Fdo……

Motivos para solicitar el acceso restringido, cerrado o embargado del trabajo en el Repositorio Institucional:

MASTER'S DEGREE IN INDUSTRIAL ENGINEERING

MASTER FINAL THESIS

CARAVACA II: ISLANDS WITH ENERGY STORAGE: INRUSH CURRENT

Autor: Gonzalo Tejero Calvo

Director: Jesús Varela Sanz

Co-Director: Lukas Sigrist

Madrid

ACKNOWLEDGEMENTS

I could not have possibly ended this life stage without the support of my family and my closest friends, since they have supported me through the good and bad moments and have tough me to act with justice, perseverance, and wisdom in each step of the way, and to enjoy every little moment that life offers.

Special thanks to my directors, both the industrial, Jesús, and academic, Lukas, since they have guided me through the development of this thesis. With their support I have strengthen my passion for the engineering field, to look for solutions for the problems of the world.

I am very thankful for Luis Rouco, who has patiently helped me to understand the insights of the inrush current, and for Enrique Pedruelo, who made possible the fulfilling real tests experience.

CARAVACA II: ISLANDS WITH ENERGY STORAGE: INRUSH CURRENT

Autor: Tejero Calvo, Gonzalo.
Director: Varela Sanz, Jesús and Sigrist, Lukas.
Collaborating Entity: Iberdrola.

ABSTRACT

In this thesis, the islanding operation with energy storage is reviewed, with special focus on the inrush currents. A simulation is used to analyze this phenomenon and then contrasted to field experimentation results. Three possible solutions are also reviewed.

Keywords: Inrush Current, Transformer, Circuit Breaker, Battery, Voltage, Flux, Feeder.

1. INTRODUCTION

The objective to reach a net zero emissions environment for 2050 is leading to the development of smart solutions to increase the number of green energy sources, which has led to the increase of the distributed generation. In this scene, a BESS based island supposes a wide variety of benefits. However, it also implies several problems to be solved. Being one of these problems, the inrush current phenomenon that take place whenever a feeder is connected due to the energization of the consumption transformers.

2. OBJECTIVES

The main objective of this project is to study and analyze the inrush current phenomenon with the purpose of obtaining an accurate simulation capable of predicting the results for the energization of a feeder. Smaller objectives include the development of both a single transformer and a real feeder simulation, the comparison to the results obtained by the real experimental test and the analysis of possible solutions.

3. REAL FEEDER SIMULATION

A simulation of a real feeder from the Iberdrola BESS facility at Caravaca de la Cruz is built with the objective of analyzing the effects of energizing a whole feeder connected to a BESS.
Two main analyses are carried out. First, the effect of the voltage drop across the whole feeder is analyzed. Secondly, the effect of the closing instant of the circuit breaker for different initial flux conditions is going to be analyzed.
Figure I show the single-line diagram of the emulated feeder.

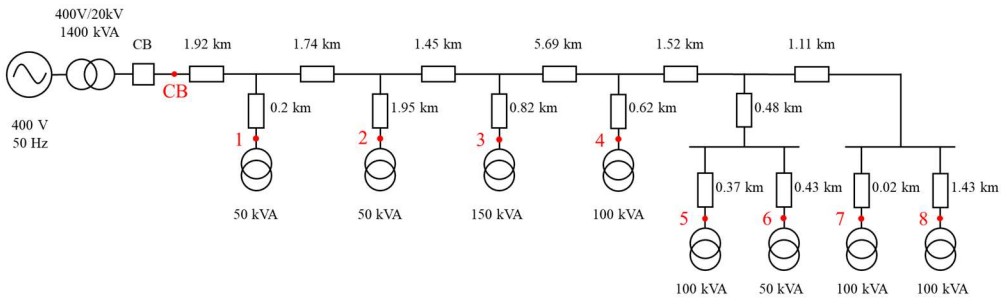

Figure I. Single-line diagram for a real feeder from the Iberdrola facility.

Table I shows the results of the simulation for the first analysis, where the relation between the voltage and the inrush current value is shown. The decrease of the voltage across the feeder leads to an overall inrush current value reduction of 24%.

Point	Description	Voltage (pu)	Estimated I (A)	Measured I (A)	Reduction (%)
1	Measurement of 50 kVA transformer	0.889	22	17.719	19.46%
2	Measurement of 50 kVA transformer	0.875	22	17.480	20.55%
3	Measurement of 150 kVA transformer	0.864	62	48.742	21.38%
4	Measurement of 100 kVA transformer	0.846	40	30.029	24.93%
5	Measurement of 100 kVA transformer	0.841	40	29.673	25.82%
6	Measurement of 50 kVA transformer	0.841	22	16.124	26.71%
7	Measurement of 100 kVA transformer	0.829	40	29.606	25.99%
8	Measurement of 100 kVA transformer	0.827	40	29.522	26.20%
CB	Measurement at the CB	0.902	288	219.070	23.93%

Table I. Simulation results for the voltage drop effect on the feeder

Results from the second simulation are shown in Table II, which shows the inrush current value for different closing instants of the circuit breaker for the six possible different initial flux cases. From these results, two main conclusions can be drowned. First, with the objective of minimizing the inrush current value, it is not possible to set a global instant to close the circuit breaker. Secondly, if we know the initial flux condition of the transformers at the feeder, it is possible to close the circuit breaker in an instant in which the inrush current effects are minimized, even removed.

		CB Triggering Steps											
		0º	30º	60º	90º	120º	150º	180º	210º	240º	270º	300º	330º
Initial Flux Condition	Case 1	30.941	0.314	27.497	85.181	139.190	159.287	197.952	219.070	203.876	153.424	137.280	87.820
	Case 2	141.481	91.810	31.261	0.307	28.356	84.094	140.043	159.451	201.937	223.718	208.175	159.246
	Case 3	212.963	164.240	141.336	90.387	30.335	0.293	29.248	90.925	145.057	165.057	207.445	228.950
	Case 4	207.896	228.536	213.285	163.351	135.118	85.960	23.944	0.298	34.328	96.577	150.288	170.530
	Case 5	149.937	169.269	200.800	222.945	207.914	159.057	131.473	81.365	25.606	0.318	34.103	94.512
	Case 6	33.972	88.617	142.794	163.455	197.965	219.437	203.537	154.124	132.718	81.600	25.681	0.312

Table II. Inrush current maximum value in A for each of the initial flux condition and circuit closing case.

4. FIELD TESTS

Seven different tests had been carried out, following the same structure. First, the system is operating in islanding mode with a determinate load that is going to be characterized by the total nominal load connected to the BESS. From this stable operating point, an additional feeder is connected to the BESS by closing a specific circuit breaker, which supposes the inclusion of an additional nominal power to the system. Besides, the manufacturer of the BESS has implemented an algorithm based on the battery output voltage variation to improve the robustness of the islanding operation mode for the connection of feeders with a larger consumption.

Three main conclusions can be made from these tests. First, the inrush current behavior analyzed both through the theory and the simulations is verified. Secondly, the benefits of applying a control voltage-based algorithm, as well as the strong voltage-inrush current relation is shown. And, thirdly, several repetition tests were made with the objective of verifying the results obtained from the Simulink simulations. However, the voltage algorithm applying leads to a loss of information since the current is limited to a certain value and therefore presents very similar values for all the cases. Therefore, further experimentation should be developed.

5. POSSIBLE SOLUTIONS

Three possible solutions are discussed in this thesis, including the use of PMU devices to perform the most efficient connection and energization of the island by first registering the voltage status when the island is disconnected and therefore de-energized, and secondly, and thanks to the use of a PMU integrated circuit breaker, by closing the breaker at the instant that minimizes the inrush effects. This first method is an effective method that could reduce the overall current value, even remove it. The second solution consist in the use of single-phase circuit breaker instead of a single three-phase circuit breaker. The main outcome from this solution is that the independent triggering of each circuit breaker results in a voltage reduction in the first energization instants that leads to a flux reduction, which corresponds to an overall reduction of around 50% of the inrush current value. Finally, the third solution consist in implementing a ramp shape voltage variation at the connection instant of the feeder. The results of programming a voltage ramp from a zero-voltage value to its nominal value results in the reduction of the magnetic flux, which leads to a maximum current value of 1.27 pu, thus representing a 90% reduction of the inrush current value.

6. CONCLUSIONS

Five main conclusions can be drawn from this thesis.

- First, through the combination of the offered tools both in Matlab and Simulink, the simulation of a transformer capable of reproducing the dynamic response that the energization of a feeder supposes has been achieved. The inclusion of the effect of the magnetizing characteristics of the transformer, which includes both the hysteresis and saturation curves, had been successfully achieved, which are the main causes for the inrush current apparition.
- An analysis of the transformers response when energized has been carried out. With this analysis, it can be verified that the transformers operation truly reproduces the inrush current behavior that has been reviewed in the investigation section of this project.
- Thirdly, the successful emulation of a real feeder has been achieved, obtaining an accurate estimation of the reached inrush current value that is produced when energizing a set of transformers connected by the distribution network. Besides, a precise inrush current estimation could be done for feeders with different configurations if needed.
- The simulation results show that it is possible to determine the initial flux status of the transformers of a feeder by keeping a voltage status register. Then, and knowing this initial status, it would be possible to trigger the circuit breaker in the optimum instant that could lead to the removal of the inrush current issue.
- The strong relation between the inrush current value and the voltage status at the connection instant has been proved both by the developed simulations and the field carried out experimental tests.

CARAVACA II: ISLANDS WITH ENERGY STORAGE: INRUSH CURRENT

Autor: Tejero Calvo, Gonzalo.
Director: Varela Sanz, Jesús and Sigrist, Lukas.
Entidad Colaboradora: Iberdrola.

RESUMEN

En esta tesis, se va a estudiar la operación en isla basada en un almacenamiento de energía, poniendo especial atención en la aparición de las corrientes de conexión o *inrush currents.* Se va a desarrollar un modelo de simulación que permita analizar este efecto y será posteriormente contrastado por experimentación en campo. Tres posibles soluciones van a ser también analizadas.

Palabras clave: Corriente de conexión, Transformador, Interruptor, Batería, Tensión, Flujo, Ramal.

1. INTRODUCCIÓN

El objetivo de cero emisiones netas para 2050 está conllevando el Desarrollo de soluciones inteligentes lo que está llevando al incremento de fuentes de energía renovables en la red de distribución. Con ello, una isla implementada mediante una batería supone un gran abanico de ventajas para la red eléctrica. Sin embargo, también conlleva algunos desafíos, siendo uno la aparición de las elevadas corrientes de conexión que tiene lugar con la magnetización de los transformadores cuando se conecta un ramal.

2. OBJECTIVOS

El objetivo principal de este proyecto es estudiar y analizar las corrientes de conexión con el propósito de obtener un modelo de simulación que permita estimar el valor de la corriente de entrada en la conexión de un ramal a la batería. Dentro de este objetivo se va a desarrollar tanto el modelo de un único transformador como de un ramal real. Los resultados serán comparados con los datos obtenidos en campo y posibles soluciones serán analizadas.

3. SIMULACION DE UN RAMAL REAL

Un modelo de simulación de uno de los ramales de la red de Iberdrola en Caravaca de la Cruz se ha llevado a cabo para analizar los efectos de energizar un ramal conectado a una batería. En la figura I se muestra el diagrama unifilar del ramal simulado.
Dos análisis se han llevado a cabo. En primer lugar, el efecto que la caída de tensión a lo largo del ramal tiene sobre el valor de la corriente de entrada obtenido va a ser estudiado. En segundo lugar, el efecto del momento de cierre del interruptor en relación con la posición de la tensión va a ser estudiado.

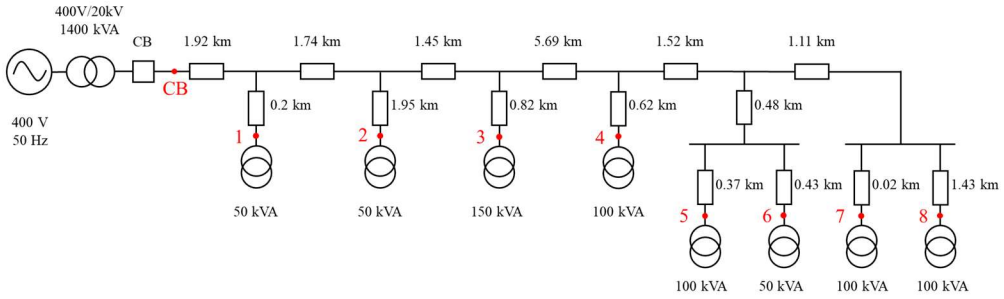

Figura I. Diagrama unifilar para el ramal de la red de Iberdrola en Caravaca de la Cruz.

En la tabla I se muestran los resultados de la simulación del primer análisis, dónde se puede observar la relación entre el valor de la tensión y el del valor máximo de la corriente de entrada obtenido. La reducción de la tensión a lo largo del ramal conlleva a una reducción total del valor de la corriente de entrada del 24% con respecto al valor esperado sin la inclusión de la red de distribución.

Punto	Descripción	Tensión (pu)	I estimada (A)	I medida (A)	Reducción (%)
1	Medida en el trafo de 50 kVA	0.889	22	17.719	19.46%
2	Medida en el trafo de 50 kVA	0.875	22	17.480	20.55%
3	Medida en el trafo de 150 kVA	0.864	62	48.742	21.38%
4	Medida en el trafo de 100 kVA	0.846	40	30.029	24.93%
5	Medida en el trafo de 100 kVA	0.841	40	29.673	25.82%
6	Medida en el trafo de 50 kVA	0.841	22	16.124	26.71%
7	Medida en el trafo de 100 kVA	0.829	40	29.606	25.99%
8	Medida en el trafo de 100 kVA	0.827	40	29.522	26.20%
CB	Medida en el interruptor	0.902	288	219.070	23.93%

Tabla I. Resultados de la simulación para analizar el efecto de la caída de tensión en el ramal.

Los resultados de la segunda simulación se muestran en la Tabla II, dónde se observa el valor máximo de la corriente de conexión para diferentes instantes de cierre del interruptor para los seis posibles casos de flujo residual en los transformadores del ramal. Los resultados muestran que no es posible establecer un instante común para el cierre del interruptor, y por otro lado, demuestran que es posible eliminar el efecto de las corrientes de entrada si se conoce el estado inicial y se controla el cierre del interruptor. El valor máximo de la corriente de entrada para diferentes configuraciones del ramal puede ser estimado mediante este modelo.

		Instante de cierre del Interruptor											
		0º	30º	60º	90º	120º	150º	180º	210º	240º	270º	300º	330º
Condicion de flujo inicial	Caso 1	30.941	0.314	27.497	85.181	139.190	159.287	197.952	219.070	203.876	153.424	137.280	87.820
	Caso 2	141.481	91.810	31.261	0.307	28.356	84.094	140.043	159.451	201.937	223.718	208.175	159.246
	Caso 3	212.963	164.240	141.336	90.387	30.335	0.293	29.248	90.925	145.057	165.057	207.445	228.950
	Caso 4	207.896	228.536	213.285	163.351	135.118	85.960	23.944	0.298	34.328	96.577	150.288	170.530
	Caso 5	149.937	169.269	200.800	222.945	207.914	159.057	131.473	81.365	25.606	0.318	34.103	94.512
	Caso 6	33.972	88.617	142.794	163.455	197.965	219.437	203.537	154.124	132.718	81.600	25.681	0.312

Tabla II. Corriente de entrada en función del caso de flujo inicial e instante de cierre del interruptor.

4. EXPERIMENTACIÓN EN CAMPO

Se han llevado a cabo siete experimentos con la misma estructura. En un primer momento, el Sistema se encuentra funcionando en modo isla caracterizado por la potencia nominal de la carga conectada. Desde este punto de operación estable se va a añadir cierta carga a la isla cerrando un interruptor determinado, e incluyendo así un

ramal con una potencia nominal determinada. Además, el fabricante de la batería ha implementado un algoritmo basado en la variación de tensión que puede mejorar la robustez de la isla, permitiendo conectar ramales de mayor tamaño.
Los resultados obtenidos muestran que las corrientes de entrada se comportan cualitativamente de manera similar al comportamiento analizado en la teoría. Además, se puede comprobar las ventajas de aplicar un algoritmo basado en la variación de tensión, así como la fuerte relación entre el valor de la corriente de entrada y la tensión.

5. POSIBLES SOLUCIONES

Tres posibles soluciones se han analizado en esta tesis. Estas incluyen la implementación de un Sistema PMU en los interruptores para conseguir optimizar la conexión del ramal mediante el registro y el control de la apertura y cierre del interruptor. Con este método se puede reducir e incluso eliminar el efecto de las corrientes de entrada. La segunda solución consiste en intercambiar el interruptor que actúa en las tres fases simultáneamente por tres interruptores, cada uno actuando en una fase independientemente. Con el cierre de cada fase por separado se puede conseguir una reducción de la tensión en los primeros instantes de la energización del transformador que conlleva una reducción del flujo magnético y en última instancia una reducción de la corriente de conexión de hasta el 50% según las simulaciones que se han realizado. En tercer lugar, se ha simulado el efecto de implementar una variación de la tensión en forma de rampa desde cero hasta su valor nominal, que conlleva a pico máximo de la corriente de conexión de 1.27 pu, representando una reducción del 90%.

6. CONCLUSIONES

- Primero, a través de las herramientas que Matlab y Simulink ofrecen, se ha conseguido obtener un modelo de simulación capaz de reproducir la respuesta dinámica de la conexión de un transformador. Se ha conseguido incluir las características magnéticas del transformador mediante las curvas de histéresis y saturación que son las principales causantes de la elevada corriente de conexión.
- Se ha realizado un análisis de la respuesta de la conexión de un transformador. Se ha realizado una comparación con la teoría presentada en la parte de investigación de esta tésis, verificando el comportamiento de las corrientes de entrada.
- Se ha conseguido exitosamente emular el funcionamiento de un ramal real, obteniendo una estimación precisa del valor máximo que se puede dar en la conexión de un conjunto de transformadores conectados al ramal. Además, con el modelo desarrollado se podría emular ramales con diferentes características.
- Con las simulaciones se ha podido comprobar que es posible determinar el estado de flujo inicial de los transformadores del ramal mediante el registro de la tensión aguas arriba del ramal. Así, y conociendo este estado inicial, se podria cerrar el interruptor en el instante óptimo que permita eliminar las corrientes de conexión.
- La fuerte relación entre el valor de la tension aplicada al transformador y el valor de la corriente de conexión ha sido demostrado mediante tanto los resultados de las simulaciones como los resultados de la experimentación llevada a cabo en la instalación de Iberdrola en Caravaca de la Cruz.

INDEX

FIGURES INDEX

TABLES INDEX

1. PROJECT CONTEXT & JUSTIFICATION

With the huge increase of distributed generation in the power grid, mainly consisting of renewable power generation, the electric power system paradigm has changed. Traditionally, generation was situated far from consumption, connected by the power grid, based on transmission and distribution lines, which stablished a one-way power flow, from the generation at the top, to the consumers at the bottom of the electric power system. The development of renewable energy sources has made possible to situate generation closer to consumers, mainly in the distribution grid, therefore reducing transmission losses. Distributed generation raises some challenges. This project mainly focuses on one of these challenges, the generation of islands, or islanding. Islanding takes place when a section of the power grid keeps energized even though the grid is supposed to disconnect due to a hazardous condition at the power grid. This event occurs in presence of a distributed generator in that section. Islanding keeps distribution lines and loads energized when they should be disconnected, therefore presenting two main problems. First, a dangerous situation can be raised for line and maintenance operators who count on a de-energized grid, and, secondly, if the reconnection to the power grid is carried out while the island has been operating independently, it may have gotten out of synchronization, therefore resulting in short-circuits that can be a problem to the main grid. However, islanding also implies that certain sections of the main power grid can operate as a microgrid, presenting some benefits listed below [1]:

- Microgrids increases the reliability of the grid by improving the continuity of the local power supply in case of contingencies in the electrical network, therefore improving the operation of the main power grid.
- Black-start restoration. In case of a black start, the presence of microgrid eases the restoration of the power grid, since microgrids can start operating independently from the network, and then, reconnect to the main grid.
- The integration of a Battery Energy Storage System (BESS) in the microgrid enable the addition of further services such as generation scheduling optimization, reactive power supply or voltage and frequency regulation, as well as imbalance compensation and spinning reserve operation. In addition, peak-shaving operation, optimization of wind and solar cycles and back-up system to the microgrid are also considered.

Although islanding operation is still prohibited, the clear advantages that it offers is boosting its investigation to solve the mentioned problems to benefit from the islanding mode of operation. Thus, Iberdrola has developed the Caravaca project, a BESS based microgrid to study and analyze the islanding operation mode. The battery supports the operation of four independent feeders.

When connecting and re-energizing each of the four feeders, huge current peaks appear, known as inrush current. Inrush currents appear due to the magnetization of the transformers connected to the feeders. Basically, inrush currents can reach peak values of 12 times the nominal current and are generally extinguished in less than a second. The main problem with the inrush currents is that, although being an instantaneous phenomenon, it is seen as a fault by the electrical protections, which will open the circuit breakers, hindering the feeder's connection process.

Therefore, the main objective is to analyze the inrush currents phenomenon to obtain a precise simulation of the energization of a feeder to ensure the island operation mode.

2. SDG ALIGNMENT

The development of this project is mainly related to two Sustainable Development Goals, shown in Figure 1.

Figure 1. SDG alignment.

- 7: Affordable and clean energy. The main objective of this goal is to ensure access to affordable, reliable, sustainable, and modern energy for all.
- 13: Climate Action. The main objective of this goal is to take urgent action to combat climate change and its impacts.

The operation of microgrids is based on distributed generation, which is mostly based on renewable energy sources (RES), especially wind and solar sources. The main issue with solar and wind power is its volatile nature since the generation depends on the winds or solar irradiation at each moment. Therefore, the inclusion of BESS in the grid seeks to offer a higher reliability to a power system based on renewable energy sources. Additionally, the RES power generation is cheaper since it does not depend upon an external fuel source, which will eventually make the purchase of electricity cheaper and more affordable. The main problem with the RES generation, which is maintaining the non-renewable generation power plants in operation is the poor reliability and continuity of the RES generation. However, the development of the combined operation of renewable generation with BESS can solve this issue and is, therefore, the next step in the decarbonization on the energy sector and the fight against climate change, supposing a great ally against the global objective of net zero emissions by 2050.

3. PROJECT OBJECTIVES

The main objective of this project is to study and analyze the inrush current phenomenon with the purpose of obtaining an accurate simulation capable of predicting the outcome for the energization of a feeder. If this objective if fulfilled, an estimation of the size of the feeders that can be energized by the battery without triggering protections can be done with the developed simulation. The completion of this objective is divided in 5 smaller objectives that are presented below:

- First, an in-depth analysis of the inrush current phenomenon and the inverter operation is going to be carried out. Both topics are reviewed through scientific papers, the theory material presented in some of the subjects of the industrial engineering degree and both industrial engineering and smart grid masters, and with the support of both the industrial and academic directors of the project. For the inrush currents, the transformer principles and operation are reviewed. The main operation principles of the power inverters are going to be analyzed, with special focus on the use of the filter, the PWM control and the dq-axis control. Additionally, the voltage source-controlled inverter is analyzed since it represents the control implemented in the BESS.

- The second step of this project is to model a three-phase transformer that can emulate the energizing transient in addition to the steady-state operation. This simulation is carried out in Simulink. The special focus of this part of the project is to include the hysteresis and saturation B-H curve in the transformer model, which is the main cause of the elevated peak inrush current values. Several transformers are going to be modelled with different parameters to have transformers with different power characteristics, with the objective of modelling and analyzing a real feeder.

- Thirdly, one of the four feeders from the Caravaca facility is modeled. This simulation includes a wider number of elements to emulate the feeder as close as the reality as possible. The objective of this simulation will be to analyze the operation of the feeder under different initial conditions to obtain an estimation of the inrush current value that will appear when energizing the feeder. Additionally, an accurate estimation of the inrush current transient extinguishing times can be obtained. This simulation will include the protection installed at the Caravaca microgrid. Thus, it is possible to check if the connection of the simulated feeder will trigger the electric protections.

- Fourthly, after all the required simulations have been carried out to analyze the connection of the feeder, a further analysis will be done in-site, where the results of the simulations will be compared to the real measures obtained from the Caravaca facility to analyze the accuracy of the model.

- Finally, and taking advantage of all the inrush current knowledge obtained through the whole project, an analysis of some possible solutions is made supported by the developed models to study the possible effects of each proposed solution.

4. STATE OF THE ART

4.1. Inrush Current

In this section, an in-depth analysis of the inrush current when energizing a transformer is going to be made, for which, first, the fundamentals and operation of a transformer is going to be reviewed.

The operation of a power transformer is mainly based on the electromagnetic induction, which is the process by which a changing magnetic field can induce a flowing current through a conductor. To understand electromagnetic induction, the Faraday and Lenz laws must be reviewed.

- Faraday Law: States that the electro-motive force (ε) induced in a coil formed by N turns, is related to the rate of change of the magnetic flux (ϕ) through the coil by (1).

$$\varepsilon = N \cdot \frac{d\phi}{dt} \tag{1}$$

  The electromotive force refers to the potential difference across the coil, and therefore can be understood as the voltage across the coil, also measured in volts. Thus, the faraday law relates the induced voltage across a coil with the variation of the magnetic flux passing through it.
  The magnetic flux density, or magnetic field describes the density and direction of the magnetic field lines. It is represented by the symbol B and measured in Teslas [T].
  The magnetic flux (ϕ), measured in Tm^2 can be understood as the magnetic flux density (B) that goes through an imaginary section S [m^2], as shown in (2).

$$d\phi = B \cdot dS \tag{2}$$

- Lenz Law: It is a consequence of applying the energy conservation principle to electromagnetic induction. It states that the magnetic field generated by an induced current is always going to oppose to the change of the magnetic flux, therefore determining the direction of the induced current of the coil. Lenz law is added to the Faraday law by adding a negative sign, resulting in (3).

$$\varepsilon = -N \cdot \frac{d\phi}{dt} \tag{3}$$

Additionally, for the comprehension of the operation of transformers it is useful to understand the Ampere law.

- Ampere Law: This law relates the magnetic field formed around a conductor with the current flowing through it. The most basic form of the Ampere's Law, for magnetic fields that have a slow variation in time is presented in (4).

$$\oint H \cdot dl = \sum_k N_k I_k \tag{4}$$

The previous equation states that the magnetic field strength, represented by the symbol H and measured in amps·turns/meters [At/m], depends on the length of the magnetic path (l) [m], the number of turns (N_k) and the current flowing through the conductor (I_k) [A]. The relation shown in (5) between the B and H depends on the permeability of the core material (μ) [T·m/A], that is obtained from the relative permeability (μ_r) and the permeability of free space (μ_0), by (6). μ_0 also known as vacuum permeability is a constant equal to $4\pi \cdot 10^{-7}$, on the other hand, μ_r is different for each material, and attending to its value, materials can be divided in ferromagnetic materials ($\mu_r > 1$), paramagnetic materials ($\mu_r = 1$) and diamagnetic materials ($\mu_r < 1$).

Additionally, in (7) the relation between the magnetic flux (ϕ) and the magnetic flux density (B) is presented.

$$B = \mu \cdot H \tag{5}$$

$$\mu = \mu_r \cdot \mu_0 \tag{6}$$

$$\phi = B \cdot S \tag{7}$$

Therefore, (4) can be rearranged through the Hopkinson law as shown in (8), where $\Re_M$ is the magnetic reluctance and l the length of the magnetic path.

$$\frac{l}{\mu S}\phi_M = \sum_k N_k I_k \xrightarrow{\frac{l}{\mu S}=\Re_M} \Re_M \phi_M = \sum_k N_k I_k \tag{8}$$

The basic structure of a transformer is composed by two coils rolled around the same ferromagnetic core as shown in Figure 2.

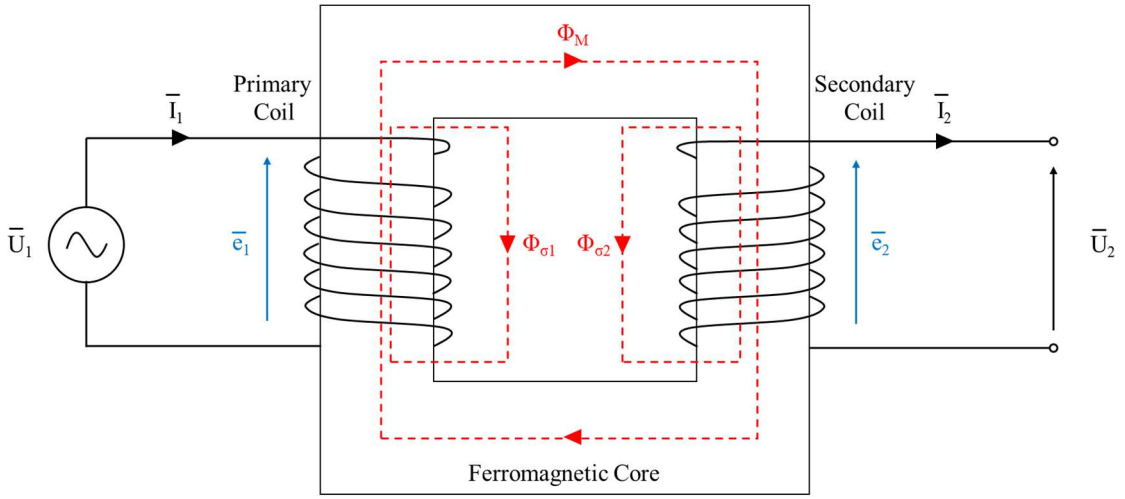

Figure 2. Basic physical structure of a single-phase power transformer.

When an alternate voltage (U_1) is applied to the primary coil, an alternate current (I_1) flows through the coil, which establishes a magnetic flux (ϕ_M). The presence of the magnetic core facilitates a magnetic low reluctance path for the magnetic flux to link both primary and secondary coils. Following the Faraday and Lenz laws, the presence of a variable magnetic flux through the

secondary coil, leads to the apparition of an electromotive force (e_2) that is going to oppose to the variation of the flux. Thus, the induced current (I_2) is obtained at the secondary coil. Additionally, the current flowing through both the primary and secondary coils is going to generate unwanted flux leakages represented by the dispersion flow through the air ($\phi_{\sigma 1}$ and $\phi_{\sigma 2}$), which produces an electromotive force in each coil ($e_{\sigma 1}$ and $e_{\sigma 2}$). The described operation of the transformer shown in Figure 2, is further analyzed by (9) and (10).

$$U_1 = R_1 I_1 + e_{\sigma 1} + e_1 \tag{9}$$

$$U_2 = e_2 - R_2 I_2 - e_{\sigma 2} \tag{10}$$

Where R1 and R2 correspond to the cupper losses in the primary and secondary coils, respectively.

Applying Faraday's Law to (9) and (10), (11) and (12) are obtained.

$$U_1 = R_1 I_1 + N_1 \frac{d\phi_M}{dt} + N_1 \frac{d\phi_{\sigma 1}}{dt} \tag{11}$$

$$U_2 = N_2 \frac{d\phi_M}{dt} - R_2 I_2 - N_2 \frac{d\phi_{\sigma 2}}{dt} \tag{12}$$

Finally, and by assuming that dispersion fluxes are proportional to the current at normal load condition [1], (13) can be applied, where $L_{\sigma 1}$ and $L_{\sigma 2}$ are the equivalent inductances for the primary and secondary windings, respectively. Finally, (14) and (15) are obtained.

$$N \cdot \phi = L_\sigma \cdot I \tag{13}$$

$$U_1 = R_1 I_1 + N_1 \frac{d\phi_M}{dt} + L_{\sigma 1} \frac{dI_1}{dt} \tag{14}$$

$$U_2 = N_2 \frac{d\phi_M}{dt} - R_2 I_2 - L_{\sigma 2} \frac{dI_2}{dt} \tag{15}$$

On the other hand, if we apply the Ampere's law to the magnetic circuit presented in Figure 2, equation (16) is obtained.

$$N_1 I_1 - N_2 I_2 = \Re_m \phi_M \tag{16}$$

Rearranging (16), (17) is obtained.

$$I_1 = \frac{N_2}{N_1} I_2 + \frac{\Re_M \phi_M}{N_1} = \frac{N_2}{N_1} I_2 + I_M \tag{17}$$

As seen in (17), the current flowing from the primary side can be divided in two terms, the current that is flowing to the secondary side, and the magnetic current, that is flowing through the magnetic core. This magnetic current is also going to produce some conduction losses on the iron core. However, the magnetic current is usually very low in comparison with the current flowing

through the primary to the secondary side, so under normal conditions, it is usually neglected. With relation to the inrush current, it is important to highlight that, when no load is connected to the secondary side (being I_2=0), the current flowing through the primary side is going to be equal to the magnetic current.

The previous analysis of the transformer can be represented as an equivalent circuit following the equations presented above, and it is shown in Figure 3.

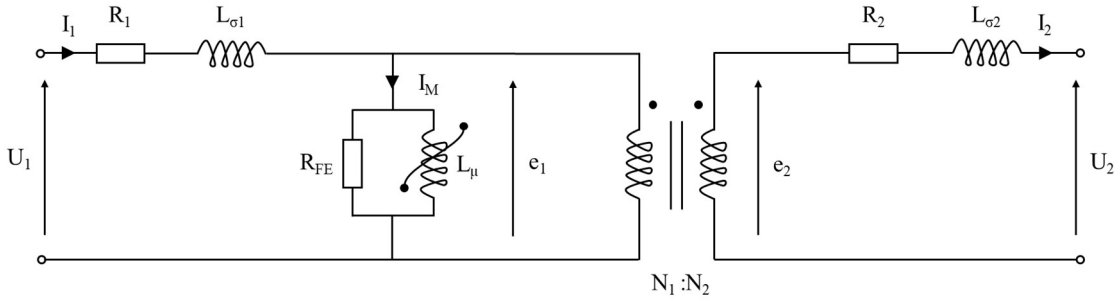

Figure 3. Equivalent circuit for a single-phase power transformer.

In Figure 3, R_1 and R_2 represent the conduction losses at both primary and secondary windings. $L_{\sigma 1}$ and $L_{\sigma 2}$ correspond to the equivalent inductances that represent the effect of the flux leakage in both windings. The parallel branch corresponds to the effects of the magnetizing current. R_{FE} represent the conduction losses from the magnetic current at the iron core. L_μ is the equivalent to the magnetic circuit in charge of generating e_1. The superimposed parabolic line stands for the non-lineal nature of the magnetic core. The relation between e_1 and e_2 is depicted as two ideal coils and is obtained from (18) and (19).

$$\frac{d\phi_M}{dt} = \frac{e_1}{N_1} = \frac{e_2}{N_2} \tag{18}$$

$$\frac{e_1}{e_2} = \frac{N_1}{N_2} \tag{19}$$

As previously discussed, the relation between the B and H depends on the permeability of the core material (μ). In Figure 4 [3], the B-H curves for different core materials is presented.

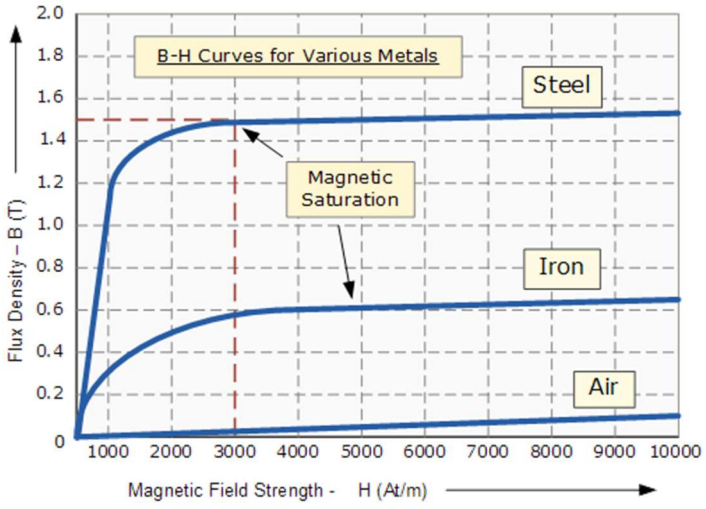

Figure 4. B-H curves for different core materials.

While the B-H relation is constant for air cored magnets, for ferromagnetic cored magnets, the B-H relation is not constant. For those materials, the initial slope reaches a saturation point, from where the B-H relation is like the air-cored magnets. Although in Figure 4 the B-H relation is shown as the combination of two lines with different slopes this relation is more like a curve.

Once the saturation point (a) is reached, if the magnetizing current that was generating the magnetic field is removed, the magnetic flux will not disappear completely, since the ferromagnetic core material will retain some of its magnetism (b). This phenomenon is known as residual magnetism (B_r) or residual flux (ϕ_r), and, if we consider the electromagnet formed by many little magnets, after a magnetizing field is applied to the electromagnet, some of these little magnets remain in the same position when the magnetizing field is removed. It can be understood as some type of "memory". Some materials have high residual flux values, making them suitable for permanent magnets, while others have low residual flux, making them suitable for electromagnets. To remove this residual flux, a negative magnetizing current can be applied to the magnet (c), known as Coercive Force (H_c).

If this negative magnetizing current is increased further, the flux density will also increase in the reverse direction, reaching the reverse saturation point (d). If the magnetizing current is removed, the reverse residual point will be reached (e). In an AC system, the magnetic flux will constantly be varying though the positive and negative curve, following the magnetic hysteresis loop, shown in Figure 5 [3].

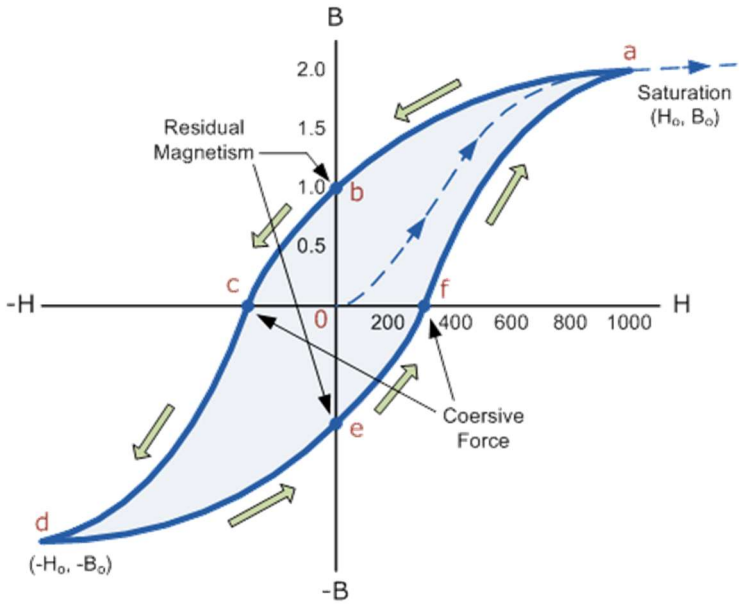

Figure 5. Hysteresis loop for a ferromagnetic core of a power transformer.

As seen in (4), H is directly related to the current flowing through the magnetic core, while B is directly related to the magnetic flux density of the magnetic core. That is the reason of the non-linear nature of the L_μ presented in Figure 3.

Once the main features of the transformer had been reviewed, the energization of the transformer going to be analyzed, since the connection of the transformer gives rises to the high-peak inrush current. To give a first overview of what happens when a transformer in energized, the following simplifications have been made:

- It is supposed that the transformer is energized with no load connected to the secondary side, therefore, no current flows through this side (I_2=0), and therefore both R_2 and $L_{\sigma 2}$ can be neglected.
- Supported by [4], both R_1 and $L_{\sigma 1}$, as well as R_{FE} have two main effects on the inrush current. First, R_{FE} represent the losses produced by the magnetizing current (I_M), therefore reducing the peak value of the inrush current, and secondly, R_1 and $L_{\sigma 1}$, have a damping effect on the inrush current. Theoretically, and for a single-phase transformer, the inrush current is extinguished following a damping factor equal to $R_1/L_{\sigma 1}$, which is obtained from the integration of the complete equation characterizing the transformer operation, presented in [4]. However, for a first approximation to the problem, which will serve to get an overall understanding of the inrush current phenomenon, R_1 and $L_{\sigma 1}$ and R_{FE} are being neglected. Besides, this simplification supposes the most unfavorable situation.

With the abovementioned simplifications, Figure 6 shows the resulting circuit.

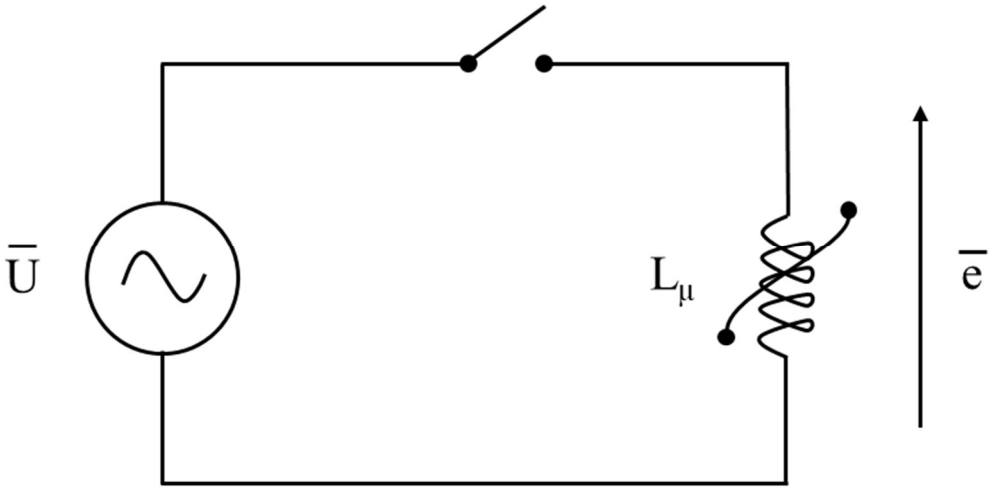

Figure 6. Equivalent circuit of a power transformer after simplification for first analysis.

Considering U as an AC voltage source following a sinusoidal curve function of time (20), being U_p the peak voltage value, ω the angular frequency [2πf] and θ, in this case, being the angular point at which the switch is closed, and therefore the transformer energized.

$$U = U_p \cdot sin(\omega t + \theta) \tag{20}$$

In this simplified case, U=e therefore obtaining (21).

$$N_1 \frac{d\phi}{dt} = U_p \cdot sin(\omega t + \theta) \tag{21}$$

Rearranging (21) to obtain the value of the magnetic flux, (22) is obtained.

$$\phi = \frac{U_p}{N_1} \int \sin(\omega t + \theta) \cdot dt \tag{22}$$

Solving equation, the expression for the magnetic flux can be obtained (23), where the peak value for the flux is represented by (24).

$$\phi = -\phi_p \cdot \cos(\omega t + \theta) + \phi_t \tag{23}$$

$$\phi_p = \frac{U_p}{N_1 \omega} \tag{24}$$

As depicted by (23), the flux is delayed 90º with respect to the applied voltage that generates the flux. ϕ_t represents a transitory component of the magnetic flux, that appears at the connection of the transformer, and is the responsible of the high inrush current peaks. For the determination of the transitory term, it is crucial to look at the initial conditions. For the initial instant t=0, therefore obtaining (25), where ϕ_0 represents the residual flux and ϕ_{t0} represents the initial value for the transitory component of (23).

$$\phi_0 = -\phi_p \cdot cos\theta + \phi_{t0} \tag{25}$$

For the general case, where $\phi_0 = \phi_r$, (26) is obtained, representing the flux at the connection instant.

$$\phi = -\phi_p \cdot \cos(\omega t + \theta) + \phi_p \cdot cos\theta + \phi_r \tag{26}$$

In (26), it is shown that the flux generated at the energization of a transformer depends on the residual flux in the magnetic core, the voltage angle at which the transformer is energized, and the peak flux value, which, as seen in (24), is affected by the peak voltage value and the number of turns of the primary winding.

There are two interesting initial conditions to be considered, the best- and worst-case scenarios.

- The best-case scenario takes place when there is no residual flux ($\phi_r = 0$), and the transformer is energized when the voltage reaches its maximum value ($\theta = 90º$). Under these conditions, the initial value for the transitory component is equal to zero ($\phi_{t0} = 0$), and therefore, as seen in Figure 7, the flux is going to be equal to the steady-state flux, and no over fluxes or currents are going to appear.

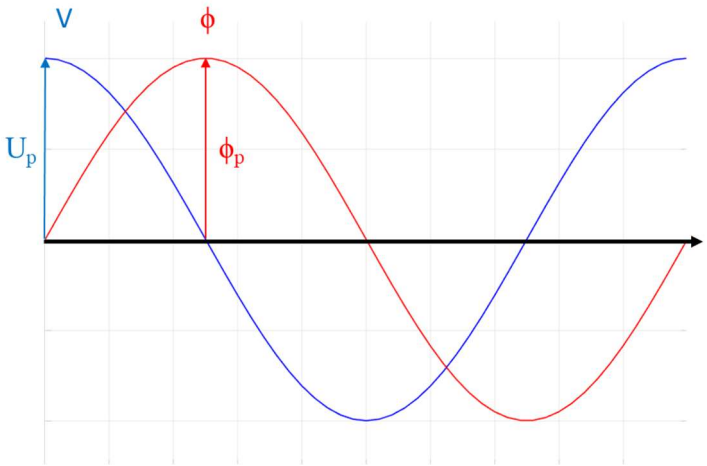

Figure 7. Best-case scenario for the energization of a power transformer, including both the voltage (blue) and the flux (red).

- The worst-case scenario takes place when the magnetic core presents a residual flux ($\phi_r \neq 0$), and the transformer is energized when the voltage is equal to zero ($\theta = 0^o$). Under these conditions, the initial value for the transitory component is composed by the residual flux plus the peak flux value. As seen in Figure 8, the flux curve is vertically displaced a total value equal to ϕ_{t0}.

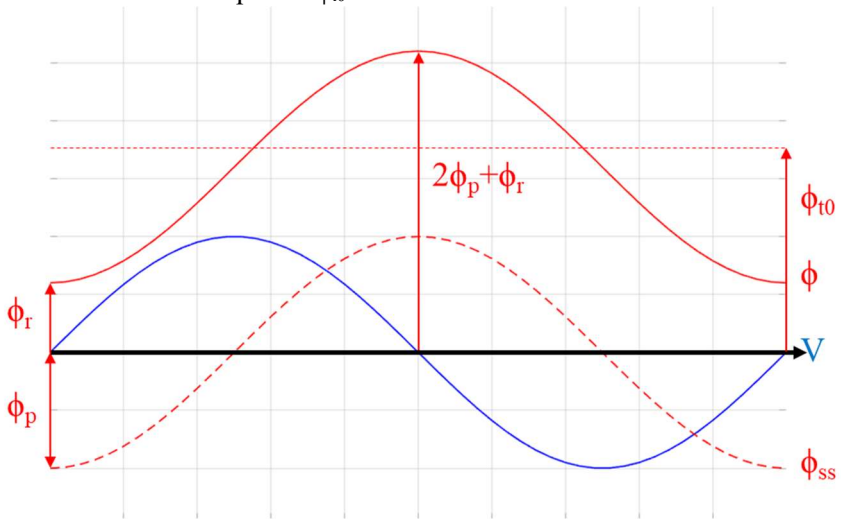

Figure 8. Worst-case scenario for the energization of a power transformer, including the voltage (blue), the total flux (red), and the steady-state flux (stripped red).

In Figure 8, the vertical displacement due to the transformer being energized when the voltage is zero is represented by the ϕ_p vertical displacement, while the effect of the residual flux is shown by the ϕ_r vertical displacement. The flux reaches a peak of two times the flux peak in steady state plus the residual flux, therefore, at least doubling the total flux presented in the previous case.

In the two previous cases, the reached peak values have been discussed. Additionally, it is important to analyze the transient affecting the flux variation to know for how long these high peak values are going to be maintained. As seen in (27), the flux expression is formed by a steady state and a transient term. The transient term is exponentially reduced following a damping factor that is related to the series impedance of the primary winding [4].

$$\phi = -\phi_p \cdot \cos(\omega t + \theta) + \left[\phi_p \cdot cos\theta + \phi_r\right] \cdot e^{\frac{-R_1}{L_{\sigma 1}}t} \quad (27)$$

As seen in Figure 9 [4], the total flux (ϕ_T) is composed by the steady-state flux (ϕ_{ss}), which is the sinusoidal part of the flux and a transitory term that is extinguished following the exponential function presented in (27). Therefore, the damping factor ($R_1/L_{\sigma 1}$) determines for how long the inrush effect is going to affect the system.

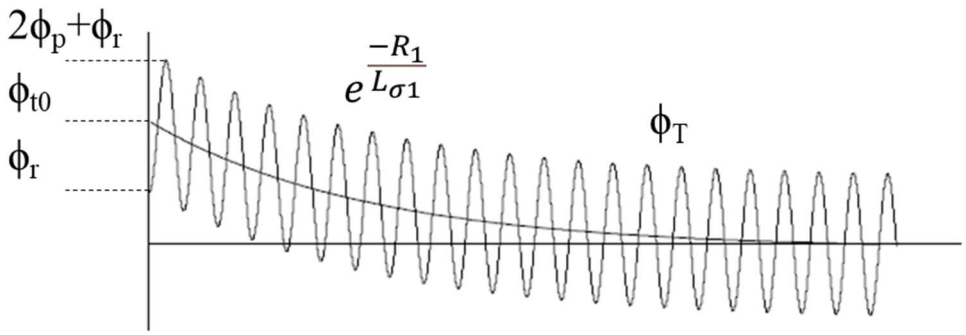

Figure 9. Total flux at the energization instant, composed by a steady state flux and a transitory term that is extinguished following a $R_1/L_{\sigma 1}$ factor.

The expression obtained (27), has been theoretically obtained by considering linear magnetic characteristics and neglecting the core losses. However, in practice, the time constant (L/R) is not constant since the inductance value changes with the magnetic flux density value. In the first cycles, where the magnetic core is in a high saturation level, the L value is small. When both the winding and core losses damp the circuit and the flux value decreases, the L value increases. Therefore, for the first cycles, the decay rate is higher than for the later cycles.

For three-phase transformers the extinguishing time is more complex to obtain and depends on the construction of the transformer among other factors. The in-depth analysis of three-phase transformers is presented in [6] and [6].

The inrush current phenomenon last for an approximate time of a few seconds [4].

Once the flux has been determined, the current can be obtained thanks to the magnetizing curve B-H. Figure 10 [7] (a) presents the relation between the magnetizing current and the magnetic flux at the transformer core, which is an equivalent from the B-H curve of the ferromagnetic material. In Figure 10 [7] (b), the inrush current curve obtained from the total flux wave is shown. The high peak obtained results from the saturation that the flux-current presents. In the non-saturated zone, for a big change in the magnetic flux, the current is going to present a slight change in its value. However, once the saturation point is reached, for each little increase in the flux value, a huge increase in the current is going to appear. That is the reason for the high peak values of the inrush current.

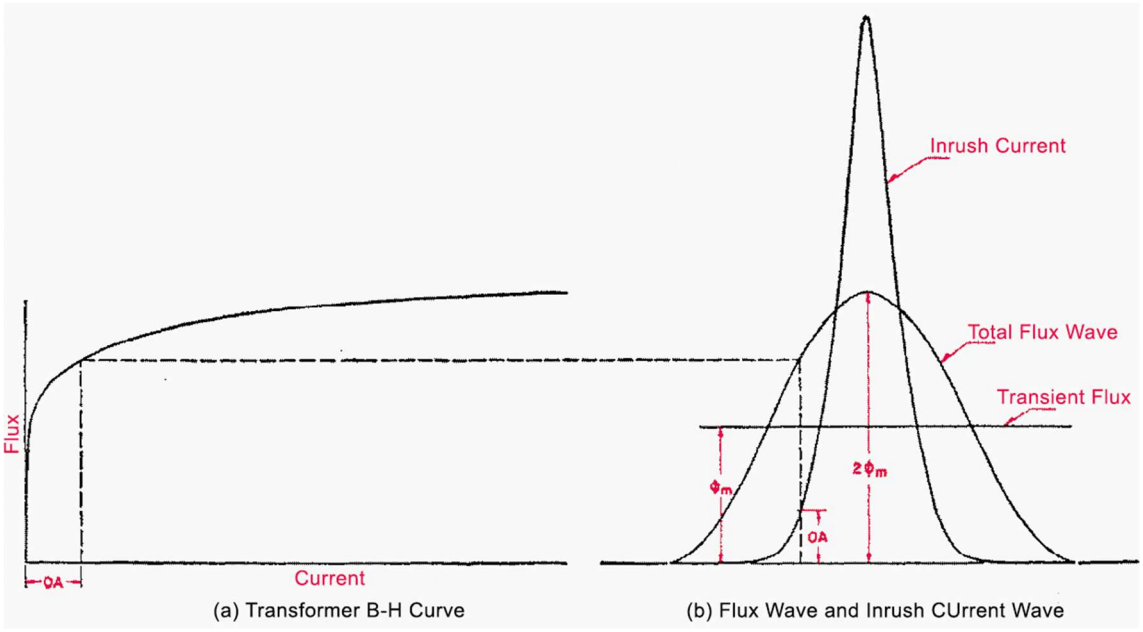

Figure 10. Transformer B-H curve (a), showing the relation between the magnetic flux and current. Inrush current generated by the flux wave (b).

A typical inrush current transient is shown in Figure 11 [4], where the inrush current peaks are all positive since the flux does not reach a zero value until the transient is almost fully extinguished.

Figure 11. Typical inrush current transient for a power transformer.

For the whole previous analysis, the source connected to the transformer has not been taken into consideration. An estimation for the computation of the effect of the source impedance is presented in [7], which consist in (28).

$$I = \frac{I_0}{1 + I_0 X} \tag{28}$$

Where I_0 corresponds to the inrush current without the source impedance and X represents the effective source reactance, both measured in pu's referred to the transformer bases.

For the understanding of the inrush phenomenon, the operation while energizing a single-phase transformer has been analyzed. However, it is also important to see what happens when energizing a three-phase transformer. The main difference with a single-phase transformer, is that it is not possible to energize the transformer with the objective of minimizing the inrush effect (at the maximum voltage value), since the three-phase system is composed of three voltage signals lagging 120º each one to each other.

Now, it is important to see how a three-phase transformer affects the previously analyzed results for a single-phase transformer. Looking at the results shown at [8], it can be stated that, the best- and worst-case scenario still coincides with one of the three phases being at the maximum and

zero voltage values, respectively. Additionally, [8] shows a high value for the DC component and a high 2nd harmonic content.

Considering a three-phase transformer, and supported by [4], three cases can be distinguished:

- If the primary side of the transformer is following a delta connection, each phase is independently connected to the network, and the inrush phenomenon of each phase behaves as an independent single-phase transformer, so, the inrush current through each winding is going to be equal to the inrush current of a single-phase transformer. During a normal condition operation, the line current is √3 times the phase current, as seen in Figure 12, however, during the energization of a three-phase transformer, only one phase is switched near the worst-case condition (voltage at a zero value), while the other two phases are near the best-case condition. Thus, the line inrush current is almost equal to the phase inrush current of the worst-case phase, therefore presenting an inrush line current reduced by a factor of √3 (~0.577).

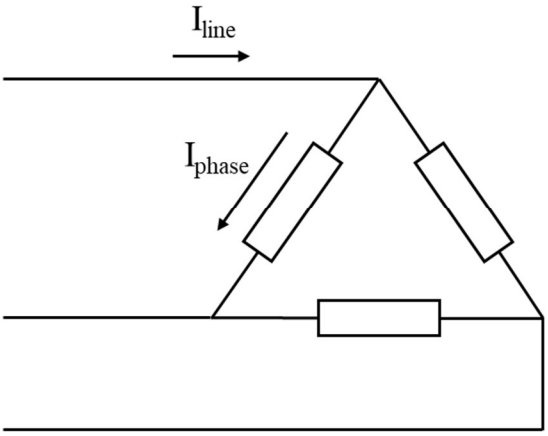

$$I_{Line} = \sqrt{3} I_{Phase}$$

Figure 12. Relation between the line and phase current in a delta connected power transformer.

- For three single-phase transformers with independent magnetic circuits and a star-delta connection, the inrush currents remain as shown in Figure 13, where I_0 represents the maximum inrush current of a single-phase transformer.

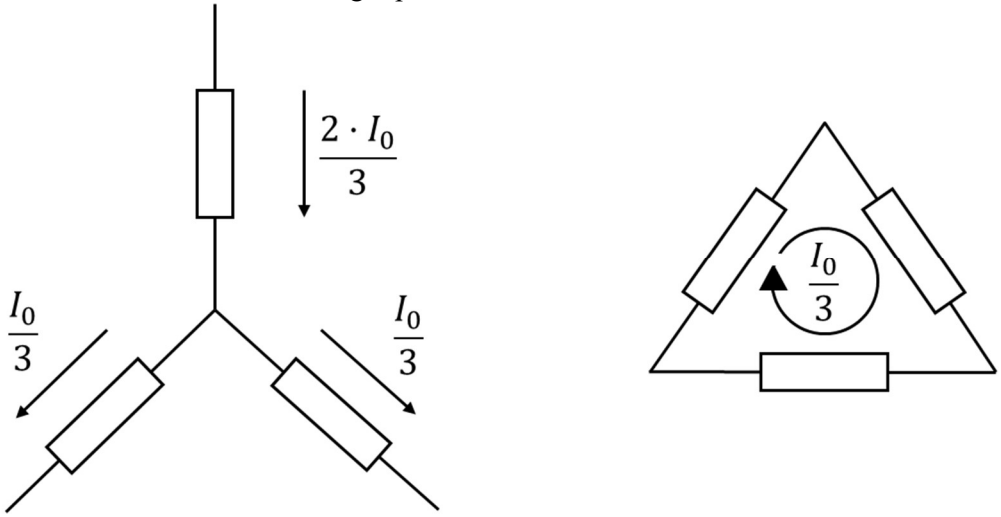

Figure 13. Inrush currents for a star-delta connected power transformer in relation to the single-phase transformer inrush current.

- For a three-phase three-legged transformer (with an interconnected magnetic circuit), three independent single-phase transformers can be considered [5]. If the primary side is star connected, and independently of the connection of the secondary side, the inrush currents remain as shown in Figure 13, with a maximum value of 2/3 of the inrush current of a single-phase transformer.

Finally, in [9], three different models for the non-linear ferromagnetic core are simulated, including:

- A linear resistance for R_{FE} and a non-linear inductor L_{μ}.
- A non-linear resistance for R_{FE} and a non-linear inductor L_{μ}.
- A linear resistance for R_{FE} and a non-linear inductor L_{μ} including the hysteresis loop.

The conclusions extracted from these three simulations are that the best results are obtained with the third model, although the first one being the simpler one.

4.2. Power Inverter

First, it is important to distinguish the different devices used in power systems to carry out a power conversion. In Figure 14, the main power electronic devices to perform a power conversion are mentioned. However, the term "converter" is usually used indistinctly for all the devices.

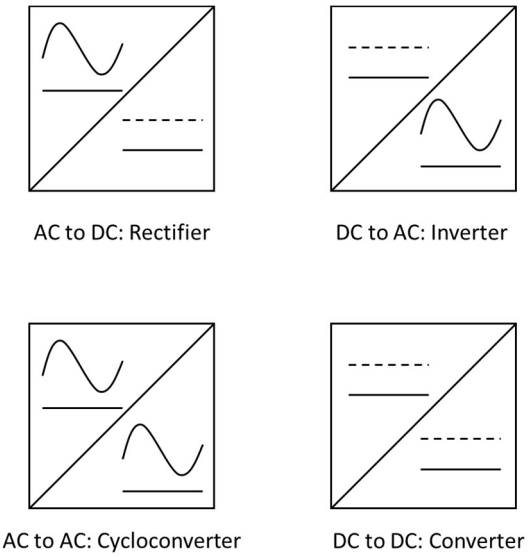

Figure 14. Main power electronic devices to perform a power conversion between AC and DC systems.

4.2.1. Operation fundamentals of the power inverter

For this section, the most relevant device is the DC to AC inverter since it forms the interface with from the DC systems with the gird. The operation and control are going to be analyzed considering the energy source as an ideal DC voltage source.

Power inverters can obtain an AC current from a DC source by using semiconductor commutation components. The easiest way to understand the fundamentals of a power inverter is by considering a single-phase system 2-level inverter with ideal switches instead of semiconductor components as depicted in Figure 15.

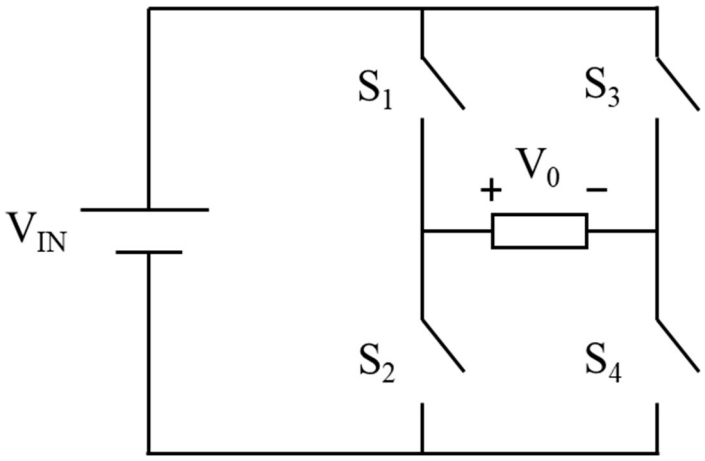

Figure 15. Single-phase 2-level inverter with ideal switches.

The system presented in Figure 15 is formed by an input voltage DC source (VIN) feeding an output AC source through four ideal switches (S1, S2, S3 and S4). Switches S1 and S4 and S2 and S3 must be paired, being always in the same state (ON or OFF). Thus, the current follows the paths showed in Figure 16, where the red path shows the direction of the flowing current when both S1 & S4 are in OFF state and S_2 & S_3 in ON state, and the blue path the direction of the flowing current in the reverse combination. Both pair of switches must be ON and OFF the same period to obtain an output signal as similar to a sinusoidal wave as possible.

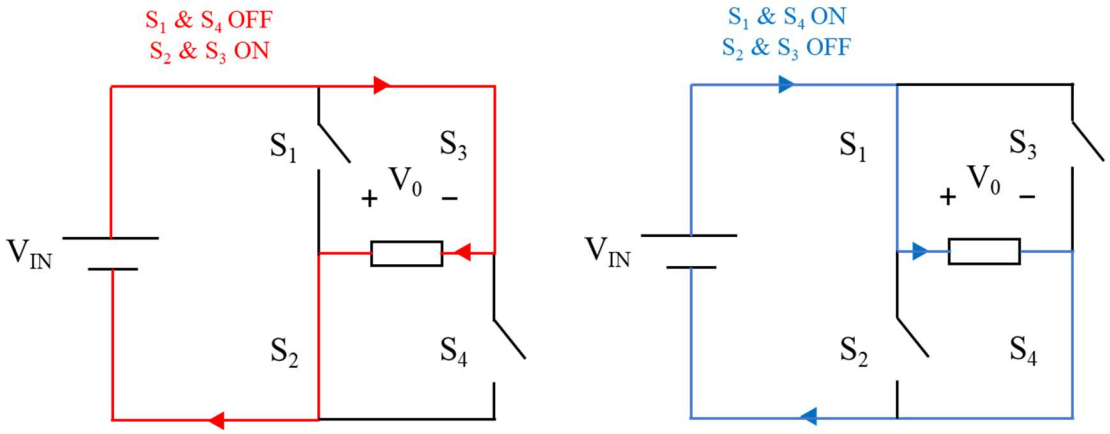

Figure 16. Current paths for each of the two inverter states.

In Figure 17, the result of the described operation is shown. The obtained output voltage consists in a square wave with a maximum and minimum value of $\pm V_{DC}$. To obtain a sinusoidal wave that is useful for the AC grid, T must be equal to 1/50 s, to set the frequency to the nominal value. Additionally, the stripped red line is showing the fundamental harmonic of the square wave, that is the desired signal to obtain at the output. Thus, an LC low-pass filter is usually set at the inverter output, to obtain a sinusoidal wave with low harmonic content.

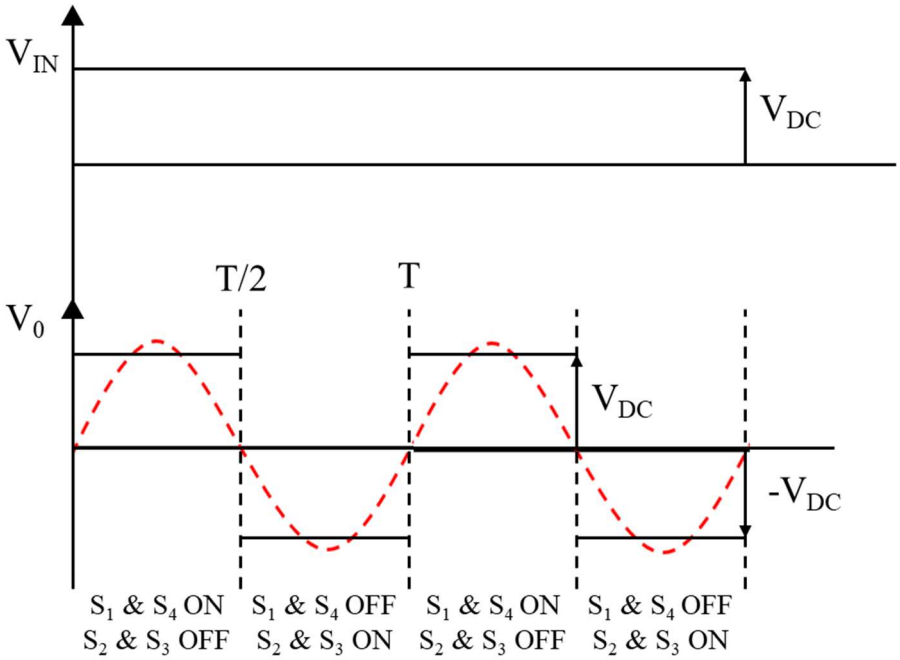

Figure 17. Relation between the input and output voltage at the inverter, including the first harmonic of the output voltage (red).

Once the basic operation of an inverter has been understood, it is important to analyze a more real approach. First, switches shown in Figure 15 are really formed by two main components, a commutation element that works as the switch; usually a thyristor, a MOSFET or an IGBT, and a diode to let inverse current flow. The resulting inverter schema is presented in Figure 18, considering real switches and the LC filter.

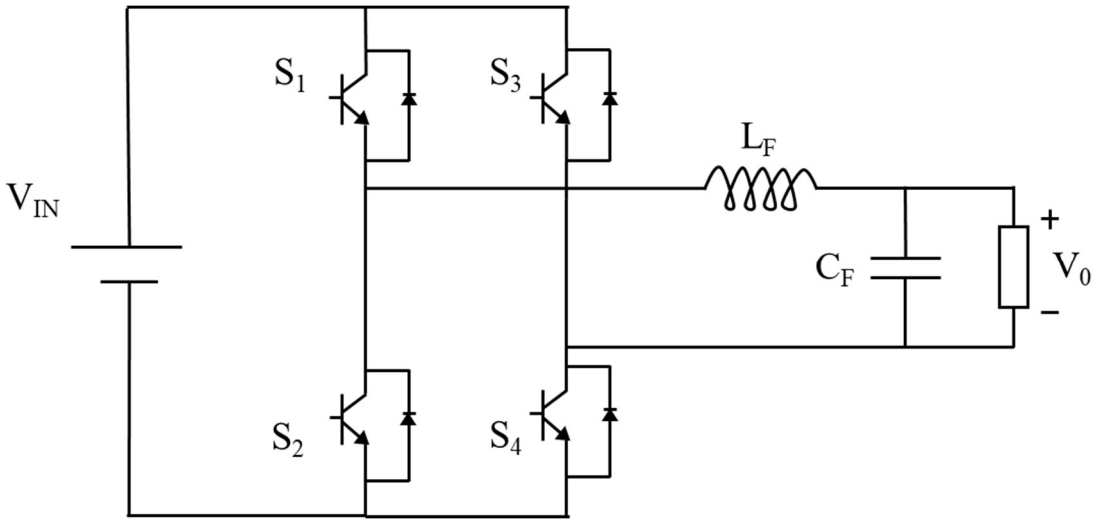

Figure 18. Single-phase inverter with real commutation elements and LC filter at the output.

Secondly, since the commutation element is not ideal, conduction and switching losses must be considered. Conduction losses usually represent a low part of the total losses. Switching losses only take place at the point of opening and closing the switch, since the variation of voltage and current is not immediate, as shown in Figure 19. To generate a voltage & frequency variable signal with sufficient power values, the commutation elements are required to work at saturation (V~0) and short point (I~0).

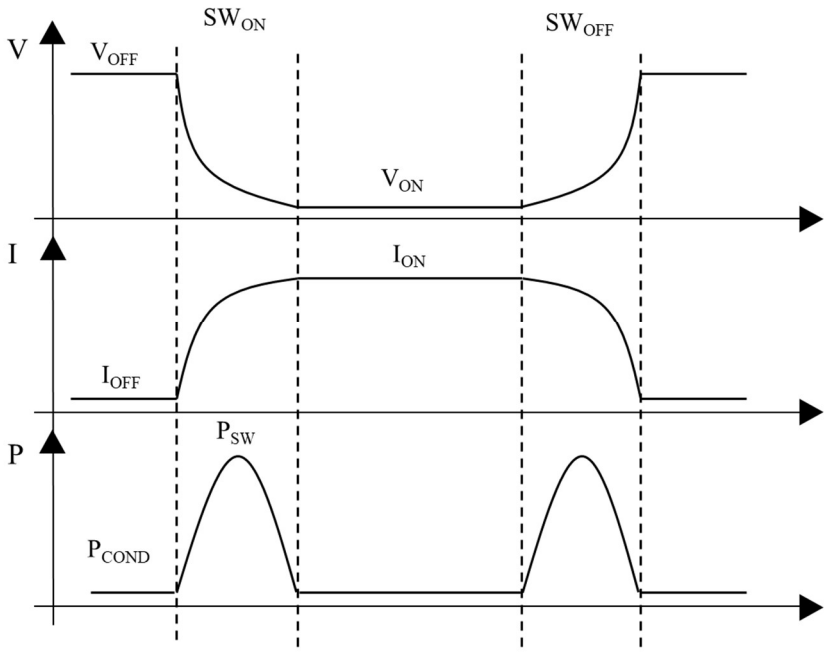

Figure 19. Conduction and switching loses, including the steady-state and transitory period for the activation and deactivation of each switch.

As previously analyzed, the output voltage can be controlled by controlling the commutation elements (the time that each pair of switches in ON and OFF state). The main objective of the inverter is to obtain a sinusoidal wave; therefore, the switch control must be focused in obtaining a signal to optimize the use of the filter to obtain the desired signal. To do so, a PWM (Pulse Width Modulation) control is used.

For instance, the sinusoidal PWM method modulates the pulses width proportional to the value of a sinusoidal wave in each instant as shown in Figure 20. It also shows the state of the four commutation elements depending on the value of the PWM signal. The PWM method has two main advantages: it allows a high-level control of the output signal, both in the amplitude and frequency, and that the obtention of the fundamental harmonic is easier.

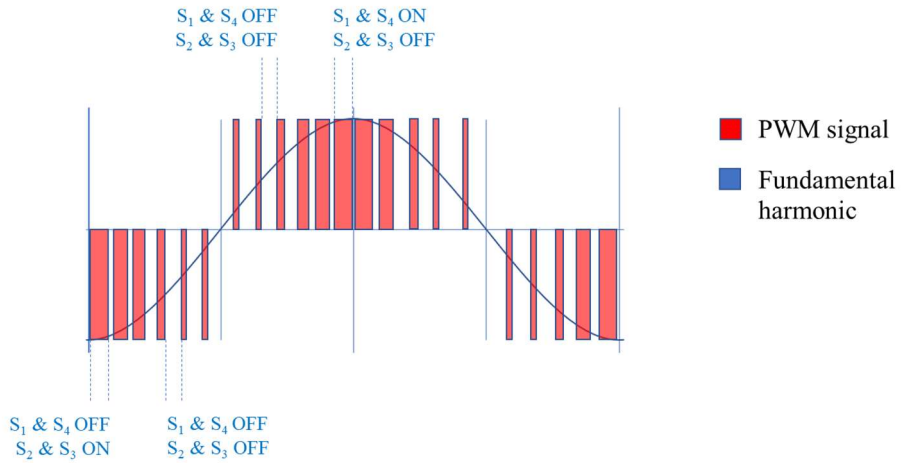

Figure 20. Sinusoidal PWM modulation method.

The obtention of the sinusoidal PWM signal is done by two signals, a carrier, and a modulation signal as shown in Figure 21. The carrier signal is usually a high-frequency triangular signal, whereas the modulation signal coincides with the desired sinusoidal signal. Modifying both the amplitude and the frequency of the modulation signal will in fact change the output signal obtained at the inverter. The relation between the peak values of the carrier and modulation signals is known as the modulation factor (m), and it establish the amplitude of the output signal. If m>1 overmodulation will take place, and the output signal will not be as precise as possible. If m>>1, the output signal is a square wave.

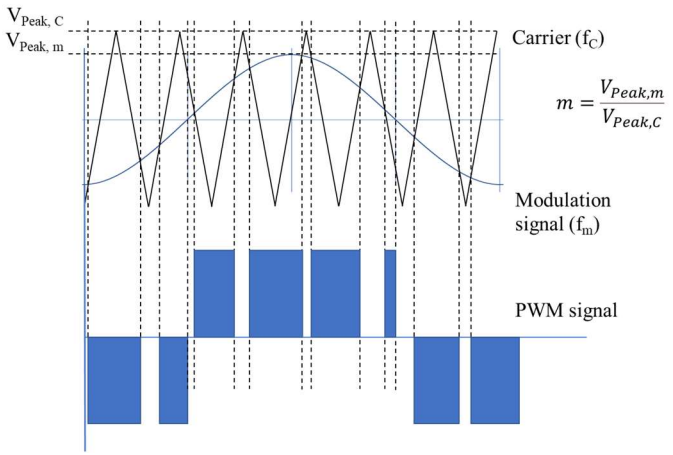

Figure 21. Obtention of the PWM signal by the combination of the carrier and modulation signals.

In Figure 22 [10], an output voltage signal obtained by a PWM signal is shown in addition to its frequency spectrum. The first harmonic is controlled by the modulation index, m. The higher harmonics content are multiples of the carrier frequency (f_C). The higher the value of f_C, the easiest it will be to remove the higher harmonic content. However, there is a trade-off when choosing f_C, since for higher frequency values, there will be more switching ON & OFF, and therefore more switching loses.

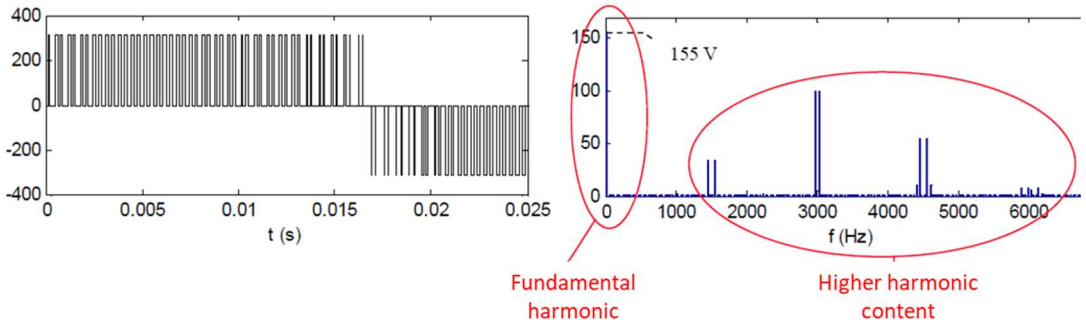

Figure 22. Output voltage PWM signal in time (left) and in frequency spectrum (right).0

For a three-phase inverter, the fundamentals and the operation are analogous to the single-phase inverter but applied to each of the three phases. The basic three-phase inverter circuit is depicted in Figure 23.

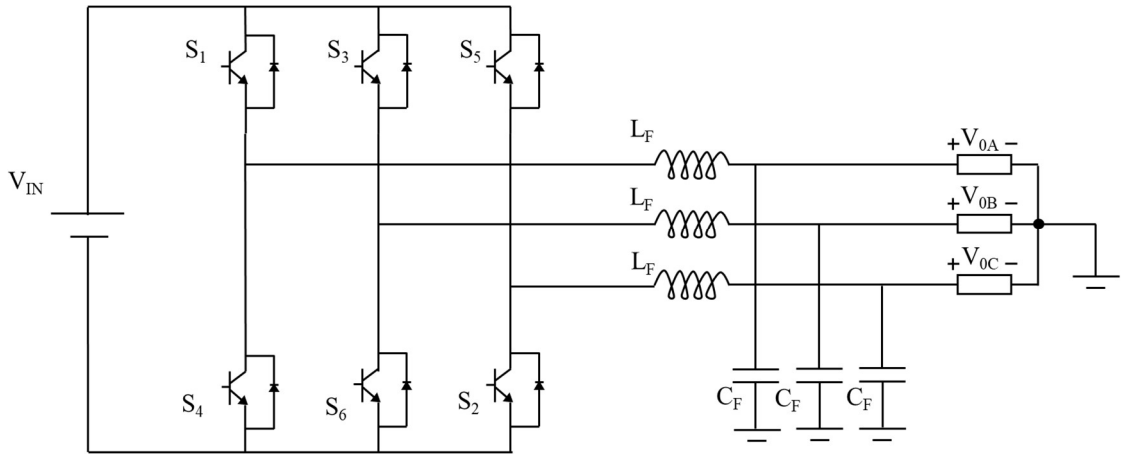

Figure 23. Three-phase inverter.

The outcome of the previous analysis is that the objective of the control of an inverter is to obtain the required modulation signal that is going to shape the output voltage signal.

The control of the power inverter is usually done in the dq axes, using the Park transformation.

A three-phase system formed by three sinusoidal waves displaced by 120º each both electrically and spatially can be expressed with the spatial vector shown in (29), (30), (31) and (32), where f (t) can be used both for the voltage and current.

$$f(t) = \frac{2}{3} \cdot \{f_a(t) \cdot e^{j0} + f_b(t) \cdot e^{j2\pi/3} + f_c(t) \cdot e^{j4\pi/3}\} = f_{peak} \cdot e^{j\omega t} \quad (29)$$

$$f_a(t) = f_{peak} \cdot \sin(\omega t) \quad (30)$$

$$f_b(t) = f_{peak} \cdot \sin\left(\omega t + \frac{2\pi}{3}\right) \quad (31)$$

$$f_c(t) = f_{peak} \cdot \sin\left(\omega t + \frac{4\pi}{3}\right) \quad (32)$$

By applying the 2/3 factor, when the current/voltage presents the nominal value (1 pu), the spatial vector will also be the nominal one (1 pu). Other factors used include the invariant power factor $\sqrt{(2/3)}$ or the effective value factor $\sqrt{2}/3$.

Additionally, to accurately represent the three-phase system through the spatial vector, an additional equation is required, that coincides with the homopolar component as seen in (33). However, the homopolar component is equal to zero if an equilibrated three-phase system is considered.

$$f_0 = \frac{1}{3}\left(f_a(t) + f_b(t) + f_c(t)\right) \quad (33)$$

Thus, f(t) can be represented as vector with amplitude equal to f_{Peak}, which represents the maximum voltage/current value, rotating at a ω speed, which determine spatial vector in DQ fix axis, represented in Figure 24.

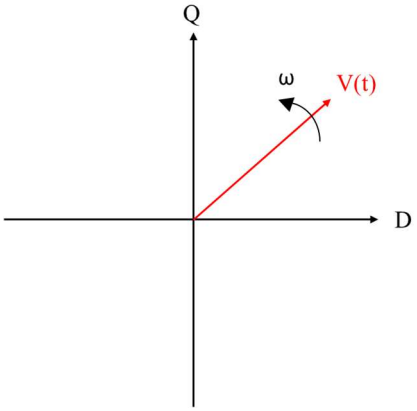

Figure 24. Spatial vector in DQ-fixed axis. Represented as a rotating vector.

The last step for the Park transformation consists in changing the DQ fix axis to a dq rotating reference axis. The key point of this last transformation is to adjust the rotating speed of the dq axis to the rotating speed of the spatial vector, so that the spatial vector is seen as a stationary vector in the new dq reference axis with constant module. This transformation is shown in Figure 25.

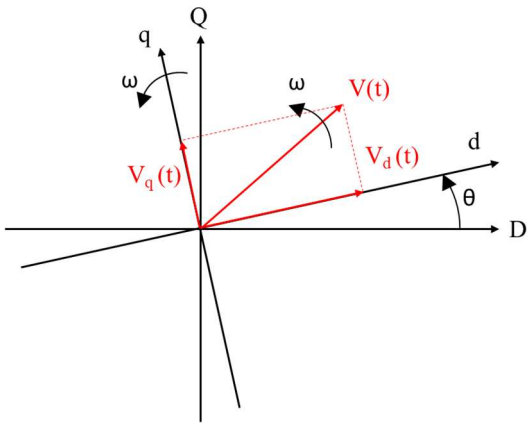

Figure 25. Transformation from DQ-fixed axis to dq-rotating axis.

The Park transformation can be represented in a matrixial way by (34).

$$\begin{pmatrix} f_d \\ f_q \\ f_0 \end{pmatrix} = \begin{pmatrix} cos\theta & sin\theta & 0 \\ -sin\theta & cos\theta & 0 \\ 0 & 0 & 1 \end{pmatrix} \begin{pmatrix} \frac{2}{3} & \frac{-1}{3} & \frac{-1}{3} \\ 0 & \frac{1}{\sqrt{3}} & \frac{-1}{\sqrt{3}} \\ \frac{1}{3} & \frac{1}{3} & \frac{1}{3} \end{pmatrix} \begin{pmatrix} f_a \\ f_b \\ f_c \end{pmatrix} \tag{34}$$

In dq axis, and for a usual power inverter under balanced operation, the active and reactive power can be computed as (35) and (36).

$$P = \frac{3}{2}(v_d i_d + v_q i_q) \tag{35}$$

$$Q = \frac{3}{2}(-v_d i_q + v_q i_d) \tag{36}$$

If the d-axis is fixed to the voltage source vector with the rotating speed being equal to ω, the q-axis component of the voltage is going to be removed as seen in Figure 26, therefore obtaining (37) and (38).

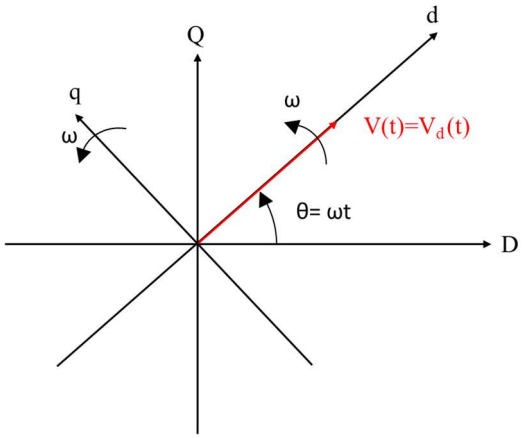

Figure 26. Spatial vector in dq-axis rotating at ω (angular speed of the spatial vector). Spatial vector aligned with d axis.

$$P = \frac{3}{2}(v_d i_d) \tag{37}$$

$$Q = \frac{3}{2}(-v_d i_q) \tag{38}$$

That is the purpose of using the dq-axis, since the active and reactive power can be independently controlled by i_d and i_q respectively.

4.2.2. Control strategy for the voltage source-controlled power inverter

As seen from (34), the angle θ needs to be obtained to accomplish the park transformation. The most common used technique to obtain θ is the Synchronous Reference Frame Phase-Locked Loop (SRF-PLL) [1]. The structure of the SRF-PLL is shown in Figure 27. The fundamental principle of the SRF-PLL is to take the value of v_q to zero through a feedback control loop. v_q is obtained by the Park transformation, then, using a PI controller, the error in the frequency value (ε_ω) is obtained and summed up to the reference frequency value (ω_{REF}). Finally, the value of the angular position is obtained by integrating the obtained angular speed. The following example illustrates how this feedback loop works. Considering a reference frequency value of 50 Hz (therefore obtaining an angular speed of ($\omega = 2\pi 50$ rad/s), supposing that the dq-axis is rotating at a frequency of 49 Hz, therefore lagging the spatial vector. In this case, a positive voltage q component is going to appear, therefore generating an error signal of 1Hz. Added to the reference value of 50 Hz, the dq-axis will begin to rotate at 51 Hz until it catches up the spatial vector. With this simple mechanism, we ensure the phase angle obtention.

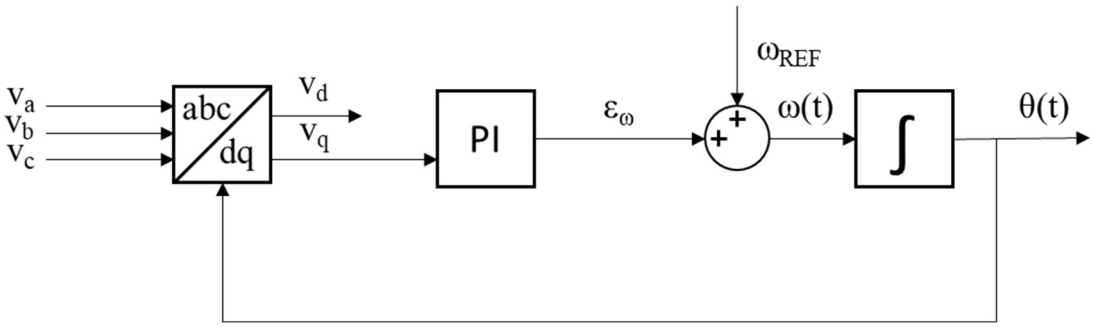

Figure 27. SRF-PLL structure.

The main drawback of the SRF-PLL is the deteriorated behavior under unbalanced conditions. To overcome this disadvantage, some methods had been proposed, as the decoupled double-synchronous reference frame PLL, which is based on the same principles of the SRF-PLL but adds some improvements on the phase and magnitude estimation in unbalanced conditions [1].

Besides, other proposals include Stationary Reference Frame Frequency-Locked Loop (SRF-FLL). As the name indicates, this method is applied in the DQ stationary axis instead of in the dq-axis, as well as being directly based on the frequency (angular speed) instead of the phase angle. The main advantage of SRF-FLL against SFR-PLL is the better response against angle jumps that might occur during transient grid faults, therefore improving the operation under unbalanced conditions [1].

Depending on the inverter operation mode, the main objective of the inverter's control can be to obtain a certain output voltage signal ($V_{O,\,REF}$) at the Point of Common Coupling (PCC), by modifying the voltage value at the output of the power inverter ($V_{F,\,abc}$). To accomplish the right voltage value at the inverter's output, two control loops are required.

First, an inner current loop is required to consider the series part of the filter, which is mainly based on an inductor (L_F) but can also include a series resistance (R_F). To understand the operation of the inner current loop, the relation between the voltage at the PCC and the voltage at the output of the inverter must be obtained. So, based on Figure 28, (39) is obtained.

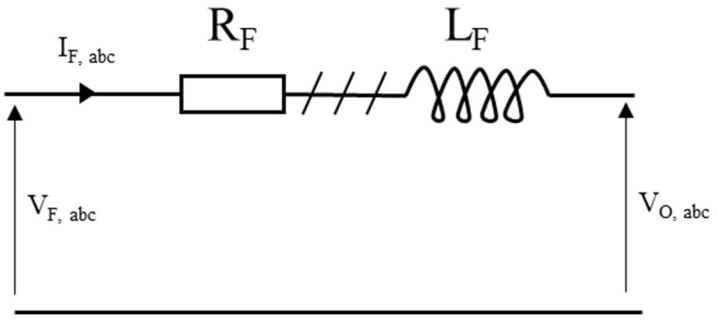

Figure 28. Filter's series components including a series resistor and inductance.

$$V_{F,abc} = V_{O,abc} + R_F I_{F,abc} + L_F \frac{dI_{F,abc}}{dt} \tag{39}$$

As previously discussed, the control is going to be done in the dq-rotating-axis, so the next step is to apply the Park transformation, P(θ) to (39), obtaining (40).

$$P(\theta) \cdot V_{F,abc} = P(\theta) \cdot V_{O,abc} + R_F \cdot P(\theta) \cdot I_{F,abc} + L_F \cdot P(\theta) \cdot \frac{dI_{F,abc}}{dt} \tag{40}$$

It is important to note that as long as both R_F and L_F correspond to diagonal matrixes with the corresponding values, they suppose no problem for the matrix computation. Additionally, to develop the third term of the right side of (40), the following steps shown in (41) and (42) must be followed.

$$\frac{d\left(P(\theta) \cdot I_{F,abc}\right)}{dt} = \frac{dP(\theta)}{dt} I_{F,abc} + P(\theta) \frac{dI_{F,abc}}{dt} \tag{41}$$

$$P(\theta) \frac{dI_{F,abc}}{dt} = \frac{d\left(P(\theta) \cdot I_{F,abc}\right)}{dt} - \frac{dP(\theta)}{dt} I_{F,abc} \tag{42}$$

Where,

$$\frac{d\left(P(\theta) \cdot I_{F,abc}\right)}{dt} = \frac{d\left(I_{F,dq}\right)}{dt} \tag{43}$$

$$\frac{dP(\theta)}{dt} I_{F,abc} = \begin{pmatrix} -\omega \cdot sin\theta & \omega \cdot cos\theta \\ -\omega \cdot cos\theta & -\omega \cdot sin\theta \end{pmatrix} \cdot \begin{pmatrix} I_{F,D} \\ I_{F,Q} \end{pmatrix} = -\omega \begin{pmatrix} sin\theta & -cos\theta \\ cos\theta & sin\theta \end{pmatrix} \begin{pmatrix} I_{F,D} \\ I_{F,Q} \end{pmatrix} \tag{44}$$

In (44), $I_{F,D}$ and $I_{F,Q}$ correspond to the current values in the DQ-stationary-axis, and the rotating matrix, that comes from deriving the initial rotation matrix to dq-axis, corresponds to a 90º rotation from the dq-rotational-axis. This can be represented by (45).

$$\frac{dP(\theta)}{dt} I_{F,abc} = -j\omega I_{F,iq} \tag{45}$$

With all the previous considerations, (45) remains as (46).

$$V_{F,dq} = V_{O,dq} + R_F I_{F,dq} + L_F \cdot \frac{dI_{F,dq}}{dt} + j\omega I_{F,iq} \tag{46}$$

(46) can be broken down in the two of the dq-axis as (47) and (48).

$$V_{F,d} = V_{O,d} + R_F I_{F,d} + L_F \cdot \frac{dI_{F,d}}{dt} - L_F \omega I_{F,q} \tag{47}$$

$$V_{F,q} = V_{O,q} + R_F I_{F,q} + L_F \cdot \frac{dI_{F,q}}{dt} + L_F \omega I_{F,d} \tag{48}$$

To develop the control, a mathematic arrangement ($\hat{V}_{F,d}$ and $\hat{V}_{F,q}$) is obtained, shown in (49) and (50), decoupling the d and q components.

$$\hat{V}_{F,d} = V_{F,d} + L_F \omega I_{F,q} - V_{O,d} = R_F I_{F,d} + L_F \cdot \frac{dI_{F,d}}{dt} \tag{49}$$

$$\hat{V}_{F,q} = V_{F,q} - L_F \omega I_{F,d} - V_{O,q} = R_F I_{F,q} + L_F \cdot \frac{dI_{F,q}}{dt} \tag{50}$$

The block schema obtained from the previous analysis to the inner current loop remains as shown in Figure 29, that includes both the control and the physical filter representation.

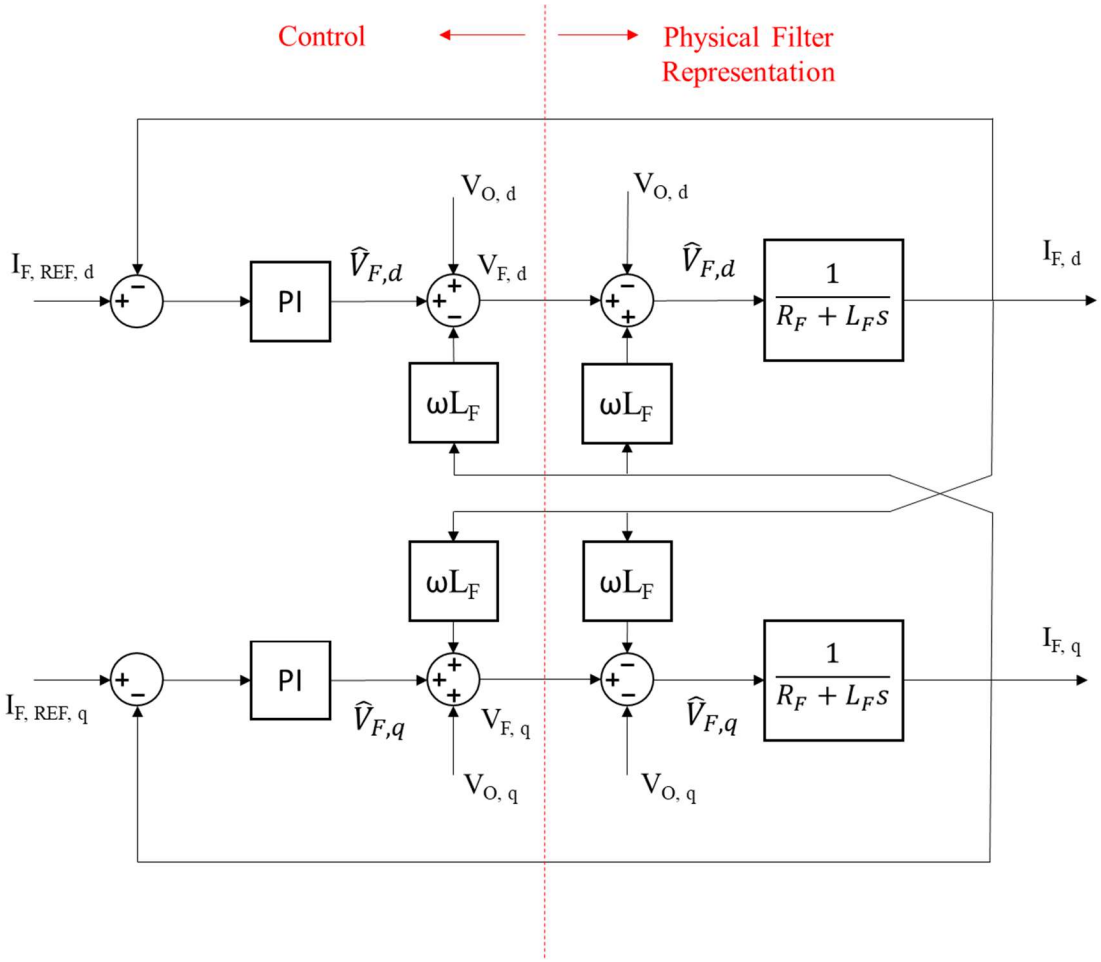

Figure 29. Block diagram of the inner current loop, including the control loop and the physical filter representation.

Secondly, an outer voltage loop is required to consider the shunt part of the filter, which is based on a capacitor (C_F). To understand the operation of the outer voltage loop, the relation between the current at the PCC and at the output of the inverter must be obtained. So, based on Figure 30, (51) is obtained.

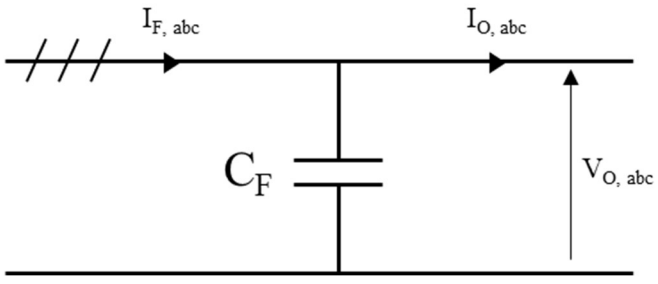

Figure 30. Filter's parallel component, including a shunt capacitor.

$$I_{F,abc} - I_{O,abc} = C_F \frac{dV_{O,abc}}{dt} \tag{51}$$

As previously discussed, the control is going to be done in the dq-rotating-axis, so the next step is to apply the Park transformation P(θ) to (51). This process is analogous to the one described for the inner current loop. Therefore, (52) and (53), show the resulting expressions broken down by the d and q axis.

$$I_{F,d} - I_{O,d} = C_F \frac{dV_{O,d}}{dt} - C_F \omega V_{O,q} \tag{52}$$

$$I_{F,q} - I_{O,q} = C_F \frac{dV_{O,q}}{dt} + C_F \omega V_{O,d} \tag{53}$$

To develop the control, a mathematic arrangement ($\hat{I}_{F,d}$ and $\hat{I}_{F,q}$) is obtained, shown in (54) and (55).

$$\hat{I}_{F,d} = I_{F,d} - I_{O,d} + C_F \omega V_{O,q} = C_F \cdot \frac{dV_{O,d}}{dt} \tag{54}$$

$$\hat{I}_{F,q} = I_{F,q} - I_{O,q} - C_F \omega V_{O,d} = C_F \cdot \frac{dV_{O,q}}{dt} \tag{55}$$

The block schema obtained from the previous analysis to the inner current loop remains as shown in Figure 31, that includes both the control and the physical filter representation.

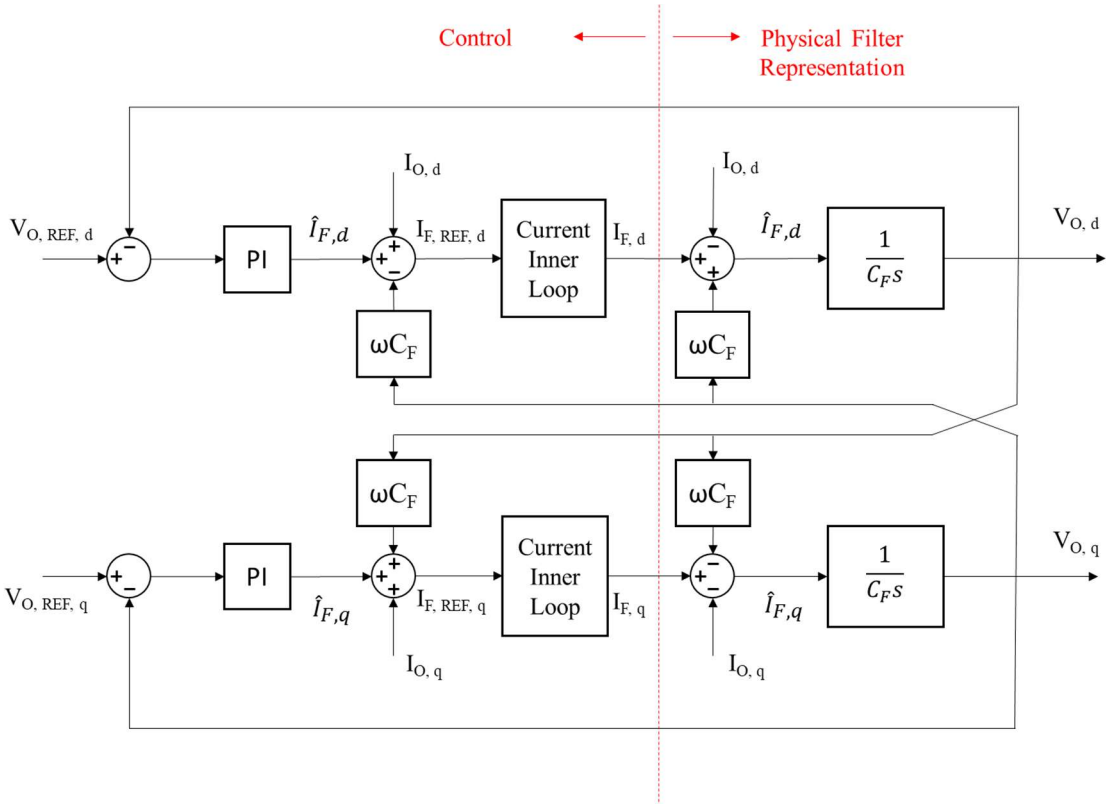

Figure 31. Block diagram of the outer voltage loop, including the control loop and the physical filter representation for a voltage source-controlled inverter.

As seen in the two previous schemas for both the current and voltage loops, three measurements from the inverter are required to control the voltage at the PCC:

- $I_{F,\,abc}$: The current that directly flows from the inverter to the series branch of the LC filter.
- $V_{O,\,abc}$: The voltage value at the PCC, which coincides with the voltage at the capacitor of the LC filter.
- $I_{O,\,abc}$: The current flowing through the PCC after the LC filter.

Finally, the control structure, including both the voltage and current loops is included in Figure 32, where the elements highlighted in red are the voltage and current measurements taken from the inverter and the filter, after being transformed to the dq-axis with the Park transformation, and $\varepsilon_{VO,\,dq}$ and $\varepsilon_{IF,\,dq}$, represent the errors in the voltage at the PCC and the current at the inverter's output in dq-axis that need to be removed, respectively. PI_{CC} and PI_{VC} represent the PI controllers for both the current and voltage control loops.

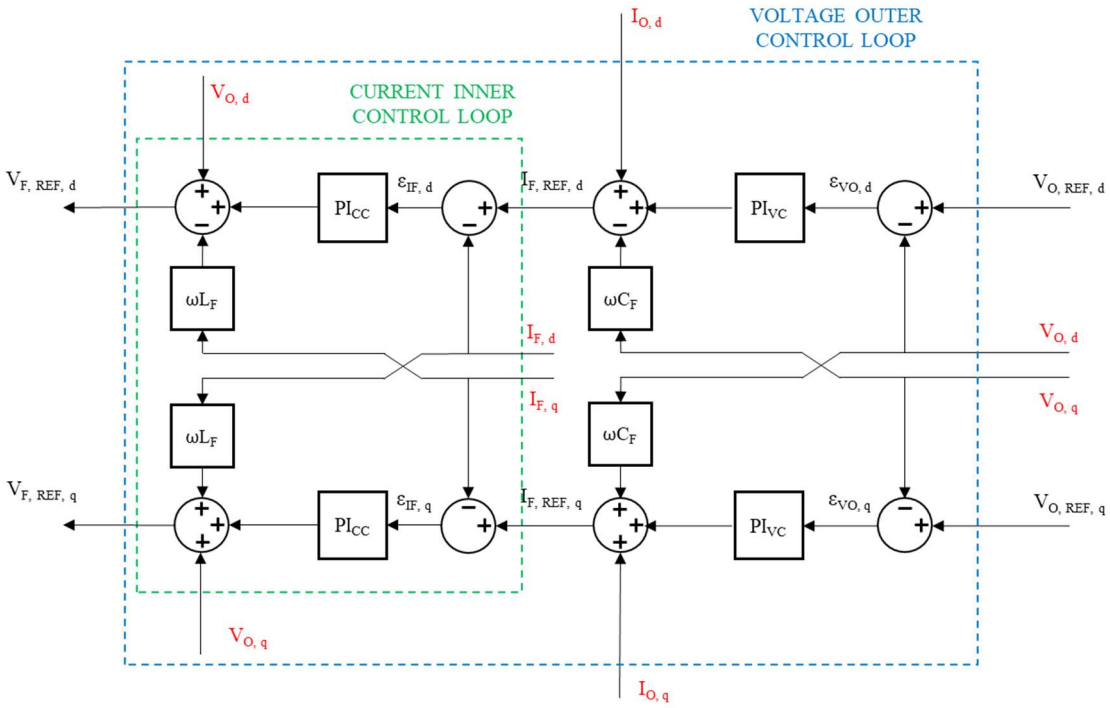

Figure 32. Voltage source-controlled inverter control inner and outer loops.

Therefore, the general inverter structure remains as showed in Figure 33. It is important to highlight that, for grid forming and grid supporting voltage source inverters, no SFR-PLL block is needed, since the voltage reference and angle are obtained from the control.

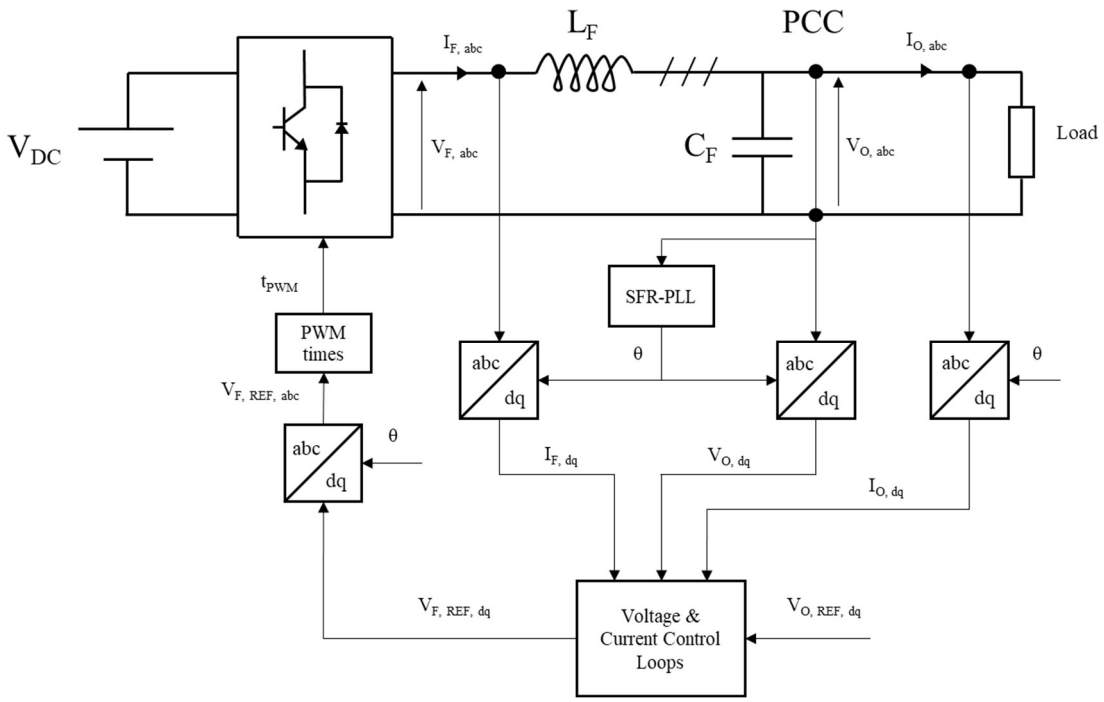

Figure 33. Voltage source-controlled inverter structure.

The obtained reference value for the voltage at the power inverter's output ($V_{F, REF}$) is used to compute the PWM signal (t_{PWM}) required for the power inverter to obtain the desired voltage, after applying the inverse Park transformation.

The presented schemas represent the operation of a power inverter controlled as a voltage source, since the objective is to obtain a specific voltage value at the PCC ($V_{O, REF, dq}$). For this thesis the focus is set on the voltage source-controlled inverter, since it is the control supported by the BESS. However, inverters may also be controlled as current sources, where the objective is to obtain a determinate current value at the PCC ($I_{O, REF, dq}$).

4.2.3. Types of Power Inverters

Now that the fundamentals of the power inverters have been analyzed, three power converters can be differentiated by their operation at an AC microgrid, which are determined by the controlled parameters, including:

- Grid-Feeding: The main objective of the grid-feeding inverters, also known as grid-following inverters, is to deliver a determinate active and reactive power to the power grid (P_{REF} and Q_{REF}), usually obtained through a high-level algorithm, such as an MPPT (Maximum Power Point Tracker), where the objective is to extract as much power as possible from the energy source. That is why grid feeding power inverters are, nowadays, the most used type for distributed generators (DG) such as solar or wind energy sources. The grid-feeding inverter need to get perfectly synchronized with the voltage and frequency of the power grid to regulate the exchanged active and reactive power. Thus, this type of converter is not suitable to work independently in island mode, since it needs a power source that stablishes the voltage and the frequency.
  The grid-feeding power inverter can be represented as a current ideal source in parallel with a high impedance, therefore, the current source-controlled inverter's structure is used in this case. Since the objective of grid-feeding inverters is to establish a reference

active and reactive power value, and the current source-controlled inverters need a reference current as an input, the relation depicted in (*37*) and (38) is used to relate these parameters as shown in Figure 34 where the obtention of the reference currents that serve as the input for the current source-controlled control structure is presented.

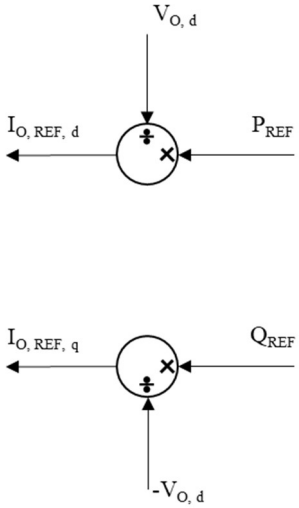

Figure 34. Obtention of the dq reference currents from the reference active and reactive power values.

- Grid-Forming: The main objective of the grid-forming inverter is to establish a voltage amplitude and a determinate frequency of the local power grid (E* and ω*). Therefore, the application of this type of inverter is limited to islanded mode operation, since for the normal operation (connected to the power grid), the synchronous generators are usually in charge of setting the voltage and frequency reference values. A way to understand the grid-forming inverter is by looking at the operation of an Uninterruptible Power Supply (UPS), since UPS are disconnected from the grid until a failure on the grid takes place, when the UPS starts working to work as an independent source for a small local system.
  The grid forming-power inverter can be represented as a voltage ideal source in series with a low output impedance, where the main objective is to establish a voltage and frequency references (U_{REF} and ω_{REF}). These inverters require a highly accurate synchronization with parallel inverters since the power sharing among them depends on the output impedance [1].
  Since the grid-forming inverter can set the frequency to its reference value, its control structure presents some changes with respect to the voltage source-controlled structure. The main difference is that instead of obtaining the phase-angle (θ) from the grid voltage, this inverter forces it to be synchronized to the reference angular speed (ω_{REF}), therefore removing the need for the SFR-PLL. The voltage input is directly the voltage reference at the output of the inverter.
  The control structure modifications for the grid-forming inverter are presented in Figure 35, where the obtention of the input for the voltage source-controlled control structure is shown ($V_{O,\,REF,\,dq}$ and θ).

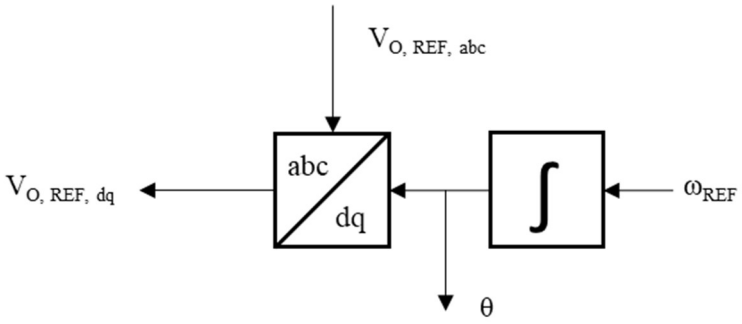

Figure 35. Obtention of the input values for the grid-forming inverters (ω_{REF} and $V_{O,\,REF,\,dq}$).

- Grid-Supporting: This type of power inverter offers benefits in between the grid-forming and grid-feeding inverters. The main objective of grid-supporting inverters is, as indicated by its name, to support the voltage and frequency grid values. It can be controlled both as an ideal current source in parallel with a high impedance, or as an ideal voltage source in series with a low output impedance, with the implying control structure for each case.
  If operated as a current source, the grid-supporting inverter needs at least an additional grid-forming inverter to operate in island mode. In this mode of operation, the main objective is not only to supply the connected load, but it is also adjusted to contribute to the voltage and frequency regulation in both the grid connected and island mode. However, if operated as a voltage source, the inverter emulates the operation of a synchronous machine, and therefore, can operate both in grid connected and independently in island mode [1].
  The two control types of the grid-supporting inverters, voltage source and current source-controlled grid-supporting inverters, are equivalent to the grid-forming and grid-following inverters but including a droop control that enables the voltage and frequency regulation and helps the current-sharing among inverters.

4.2.4. Current limiting strategies

Semiconductor components are very sensitive to the current flowing through them and are designed to support an over current of 1.2 or 1.4 times the nominal current values, which is a very small limit compared to synchronous generators, which can cope with up to seven times its nominal value [11]. To try to support the same amount of over current as a synchronous generator would lead to an oversizing of the power inverter, which would come with the related over price. Thus, power inverters must be protected from over currents. Two main solutions are described in [11].

- Virtual Impedance (VI): Basically, this method consists in emulating the effect of an additional impedance to limit the output current within the inverter's limits. First, the over current must be detected (current value exceeding its nominal value). Then, the VI is activated and its value is computed. Finally, the AC voltage drop is computed to include it in the voltage reference that is used by the inverter's control. The VI is formed by a virtual resistor (R_{VI}) and a virtual inductor (X_{VI}), computed by (56) and (57).

$$R_{VI} = k \cdot \Delta I \tag{56}$$

$$X_{VI} = \sigma \cdot \Delta I \tag{57}$$

Where ΔI correspond to the over current (I_F-I_n) and parameters k and σ are set to limit the over current to a suitable level during steady-state conditions and to ensure good system dynamics, respectively. It is important to highlight that if ΔI<0, the virtual impedance is equal to zero, and therefore, there is no effect on the control of the inverter.
The AC voltage drop is then computed by (58) and (59).

$$\Delta V_{ref,d} = R_{VI} I_{F,d} - X_{VI} I_{F,q} \tag{58}$$

$$\Delta V_{ref,q} = R_{VI} I_{F,q} + X_{VI} I_{F,d} \tag{59}$$

The new voltage reference is computed by (60).

$$V'_{ref,dq} = V_{ref,dq} - \Delta V_{ref,dq} \tag{60}$$

- Current Saturation Algorithm (CSA): This method consists basically in limiting the reference current values. Usually, priority is given to the current in the d-axis, since, as seen from (37), is the responsible of delivering the required active power. Therefore, the new reference values are computed by (61) and (62), where I_{SAT} correspond to the maximum current value supported by the inverter.

$$\left|I'_{F,REF,d}\right| = min\left(I_{SAT}, \left|I_{F,REF,d}\right|\right) \tag{61}$$

$$\left|I'_{F,REF,q}\right| = min\left(\sqrt{I_{SAT}^2 - I'_{F,REF,d}{}^2}, \left|I_{F,REF,q}\right|\right) \tag{62}$$

  As seen in (61) and (62), if no over current takes place, the reference current values are not modified, and no changes are then made to the control of the power inverter.

The control structure for the power inverter is modified as shown in Figure 36, where the effect of the VI is shown.

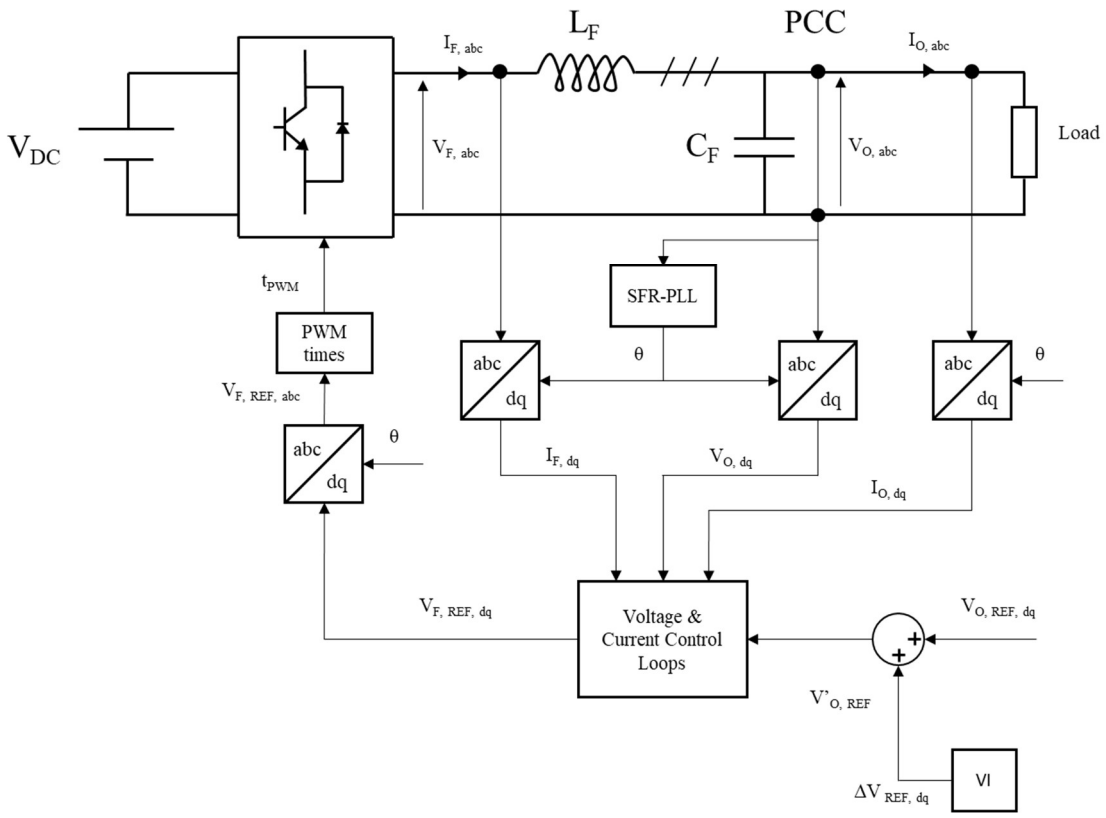

Figure 36. Voltage source-controlled inverter structure including the effect of the Virtual Impedance (VI).

The effect of the CSA is presented inside the Voltage & Current Control Loop block, and mainly affects the current inner loop as depicted in Figure 37.

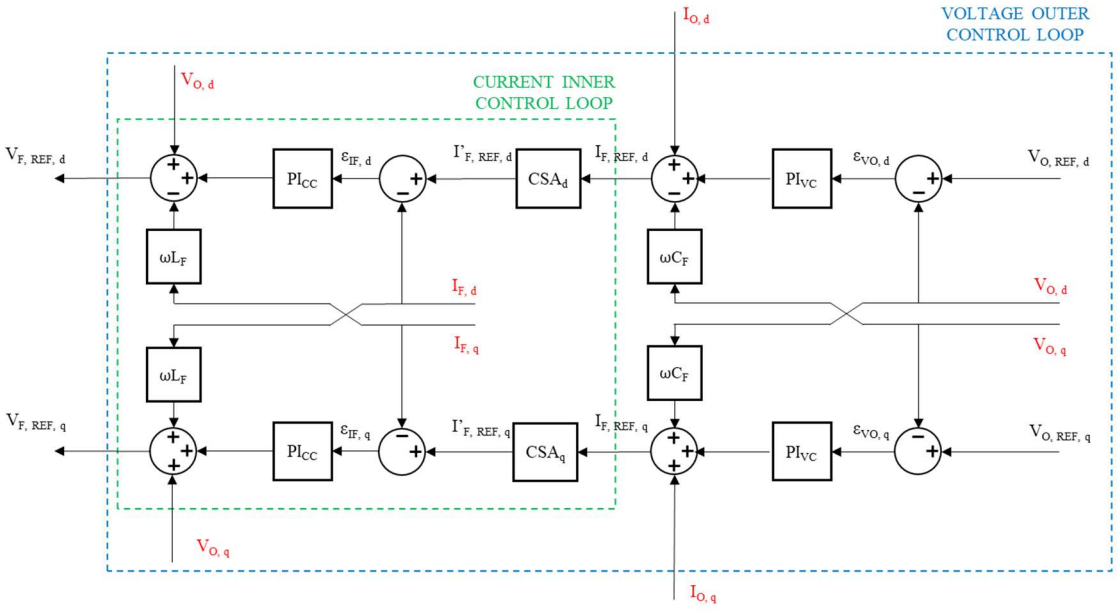

Figure 37. Effect of the Current Saturation Algorithm to the inner current control loop.

Results presented in [11] show that CSA perform better when looking at effectively limiting the output current, since the VI present some oscillations at the beginning of the fault process that

could be damaging for the inverter due to the operation on the voltage outer loop, while the CSA has direct action on the current. However, considering the post-fault synchronization, the VI method ensures a better transient stability than CSA, presenting higher critical clearing times. Finally, in [11] a hybrid solution between the VI and CSA is analyzed, which presents promising results.

4.2.5. Droop Control

Several techniques had been proposed to control the current sharing among parallel inverters, including centralized control, master-slave, or average-load sharing [1]. However, these methods require a communication network to get synchronized. Thus, these solutions may not be the most suitable one for distributed generators, hence, droop control is posed as a current sharing technique without the need for communications between devices, therefore presenting a huge improvement for the microgrid operation. The droop control is mainly used in grid-supporting inverters to maintain reasonable voltage and frequency values by regulating its active and reactive power. The development of the droop control is based on trying to emulate the operation of a synchronous generator in grid-connected mode.

Considering the power inverter as a voltage ideal source connected to the grid by a line impedance as shown in Figure 38, the active and reactive power can be obtained by (63) and (64), where PA and Q_A are the active and reactive power, respectively, injected from the power converter (A) to the grid (B) through the line impedance (Z=R+jX).

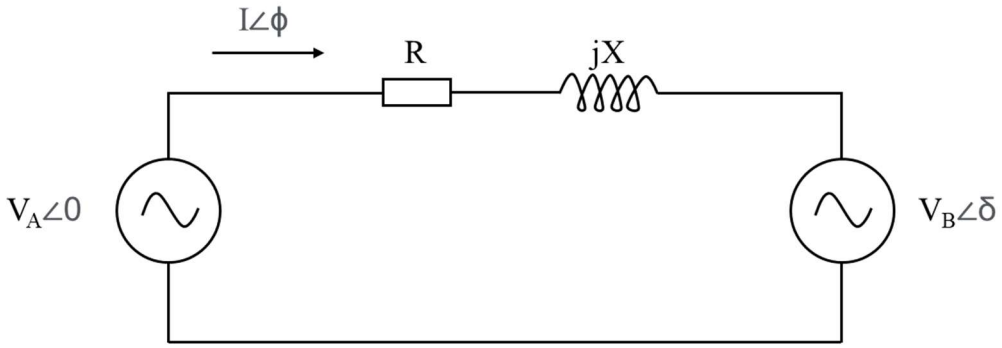

Figure 38. Power inverter as an ideal voltage source (V_A) connected to the grid (V_B) through a line impedance (R+jX).

$$P_A = \frac{V_A}{R^2 + X^2}[R(V_A - V_B cos\delta) + XV_B sin\delta] \quad (63)$$

$$Q_A = \frac{V_A}{R^2 + X^2}[-RV_B sin\delta + X(V_A - V_B cos\delta)] \quad (64)$$

Two cases can be considered when applying the droop control.

First, for high and medium voltage grids, the line inductance can be considered much higher than the line resistance, therefore neglecting the effect of the line resistance. Since the δ, the angle difference between both voltage sources is typically small, (65) and (66) can be assumed, therefore leaving the active and reactive power by (67) and (68).

$$\sin(\delta) \approx \delta \quad (65)$$

$$\cos(\delta) \approx 1 \quad (66)$$

$$P_A = \frac{V_A V_B}{X}\delta \tag{67}$$

$$Q_A = \frac{V_A}{X}(V_A - V_B) \tag{68}$$

In (67) and (68), a direct relation is depicted between the active power and the voltage angle difference ($P_A \rightarrow \delta$) and reactive power and the voltage magnitude difference ($Q_A \rightarrow V_A - V_B$). Thus, if more active and reactive power is injected, the frequency and the voltage values are going to increase, respectively. Therefore, the droop control expressions must follow (69) and (70), which is represented by Figure 39.

$$f - f_0 = -k_P(P - P_0) \tag{69}$$

$$V - V_0 = -k_Q(Q - Q_0) \tag{70}$$

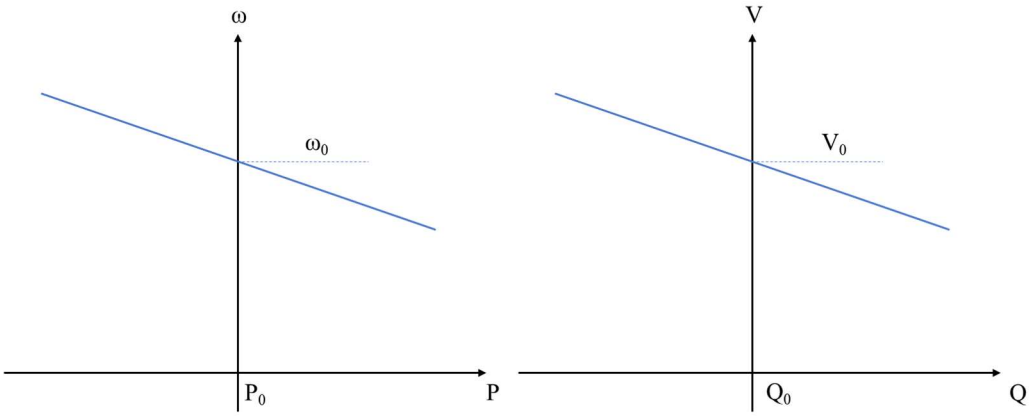

Figure 39. Representation of the droop control expressions for an inductive line impedance.

The slope of each of the frequency and voltage droop controls can be controlled by gains k_P and k_Q, respectively. Thus, each power inverter will participate in the microgrid voltage and frequency regulation following its droop characteristic.

Secondly, low voltage grids present a highly resistive characteristic, therefore, for the droop control, the inductive part can be neglected, and the same simplifications (65) and (66) are applied, leaving the injected active and reactive power by (71) and (72).

$$P_A = \frac{V_A}{R}(V_A - V_B) \tag{71}$$

$$Q_A = -\frac{V_A V_B}{R}\delta \tag{72}$$

(71) and (72) show a direct and inverse relation between the active and reactive power with the voltage magnitude and angle difference, respectively ($P_A \rightarrow V_A - V_B$, $Q_A \rightarrow \delta$). In this case, if more active power is injected, the voltage value is going to increase, however, if more reactive power is injected, the frequency is going to decrease. Therefore, the droop control expressions must follow (73) and (74), which is represented by Figure 40.

$$V - V_0 = -k_P(P - P_0) \tag{73}$$

$$f - f_0 = -k_Q(Q - Q_0) \tag{74}$$

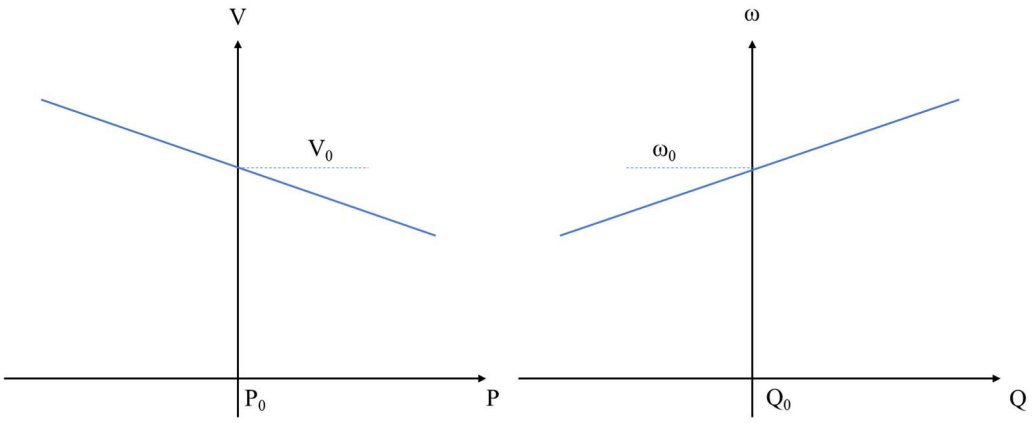

Figure 40.Representation of the droop control expressions for a resistive line impedance.

As for the first case, the slope of each of the frequency and voltage droop controls can be controlled by gains k_P and k_Q, respectively. Thus, each power inverter will participate in the microgrid voltage and frequency regulation following its droop characteristic.

The droop control has proven to be very efficient in the regulation of the voltage and frequency values. However, this method is highly dependent of the R/X relation being usually estimated. The main disadvantage is that a small estimation mismatch, especially in LV networks, can lead to an in-efficient power sharing among the parallel inverters [1]. Therefore, a possible solution could be the installation of inductors to the inverter's output, so that the line impedance could be considered as inductive. Since this solution would increase both loses and the inverter's price, the abovementioned method based on a Virtual Impedance could be used to mimic the required inductor.

The droop control structure schematic for a grid-supporting inverter controlled as a current source is presented in Figure 41, where the value of ω(t) comes from the SFR-PLL and the VO,d corresponds to the voltage at the PCC in the d-axis after the Park Transformation. In this schematic, it is shown that the reference active and reactive power include both the demand P and Q values (P'_{REF} and Q'_{REF}), and the variation (ΔP and ΔQ) due to the mismatch in both voltage and frequency to the reference values (U_{REF} and ω_{REF}).

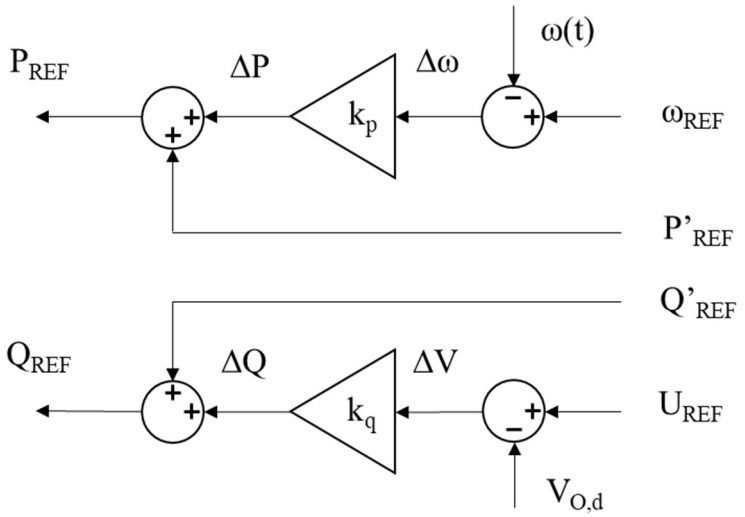

Figure 41. Droop control schematic for a current source-controlled grid-supporting inverter.

The droop control structure schematic for a grid-supporting inverter controlled as a voltage source is presented in Figure 42, where the measured active and reactive power (PMES and QMES) are computed from the voltage and current values at the output of the power inverter ($V_{O,\,dq}$ and $I_{O\,dq}$), after the Park Transformation. The voltage and frequency reference values (U_{REF} and ω_{REF}) include both the reference values (U'_{REF} and ω'_{REF}) and an additional term (ΔU and $\Delta\omega$) that include the mismatch of the active and reactive power (ΔP and ΔQ) from the respective reference values. As seen in the schematic, the phase angle (θ) is obtained from the reference angle speed value.

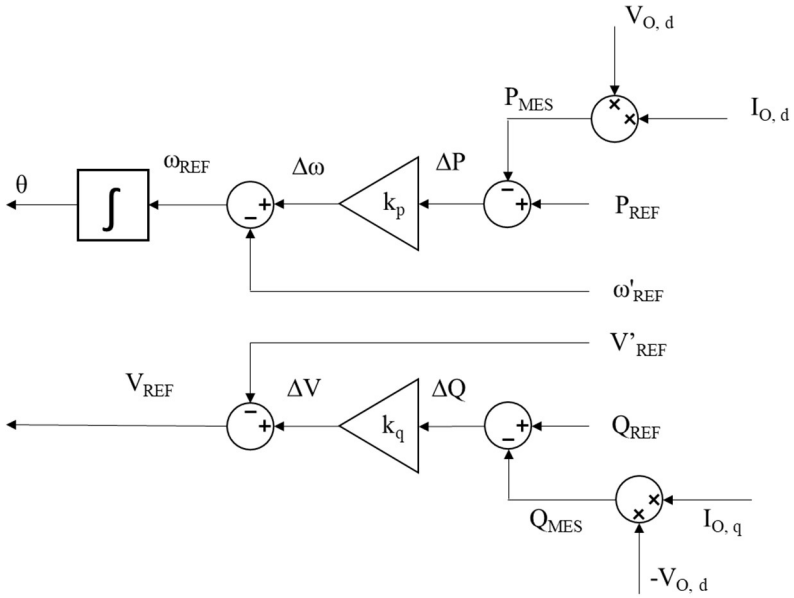

Figure 42.Droop control schematic for a voltage source-controlled grid-supporting inverter.

However, as abovementioned, the two grid-supporting inverter types are almost identical to the grid-forming and grid-following inverters, being a more theoretical difference applicable for literature.

5. SIMULATIONS ANALYSIS

In this section, a first and simpler simulation is carried out to analyze the behavior of the inrush currents when energizing a single three-phase transformer, to be followed by the analysis of the simulation of a whole feeder. In ANNEX I, all the required simulation elements are presented, and their operation is described.

5.1. SIMPLE TEST SIMULATION

5.1.1. Analysis of Transformer Simulation

In this section, an analysis is carried out for the operation of a three-phase transformer, with the objective of checking the right operation of a single three-phase transformer simulation, by comparing it to the theory presented in section 4.1.

The 50 kV transformer has been chosen to examine the energizing dynamic response, which parameters are presented in Table 12 in ANNEX I. As discussed in ANNEX I, the saturation region of the hysteresis & saturation curve has been modified to match the worse-case scenario with the highest inrush current peak indicated in [14], resulting in Figure 43, that shows an extract of the Powergui hysteresis tool, showing the saturation region of the 50 kVA transformer.

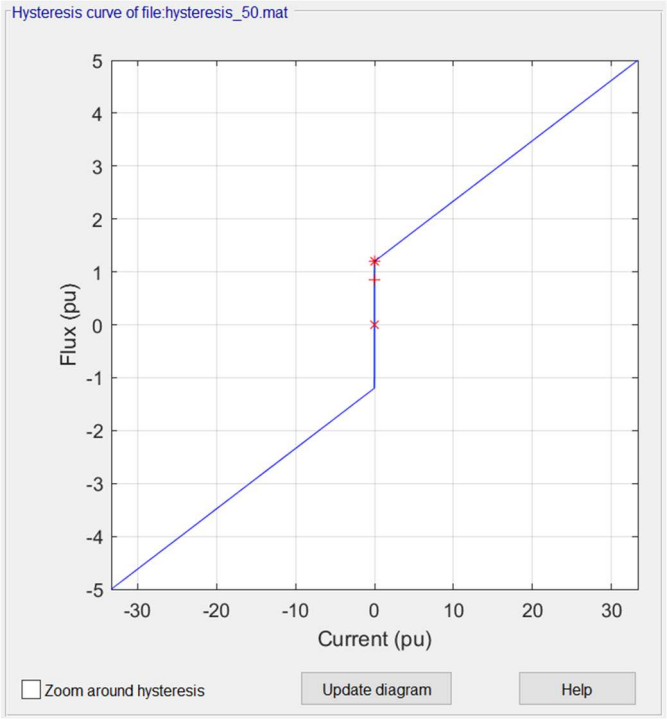

Figure 43. Flux vs. current saturation curve for the 50 kVA transformer.

Figure 44 shows the Simulink final schematic for the 50 kVA three-phase transformer. This schematic includes the battery, which is emulated as an ideal 400 V voltage source connected to the 20 kV distribution line through a 400V/20kV transformer. Indeed, under normal operation the battery operates as a voltage source when islanded and therefore the approximation as a voltage source seems reasonable. Nonetheless, during transients this approximation is not valid since the inverter control involves current limitations (see section 4.2.4) and the inverter stops being a voltage source. The distribution line and the three-phase circuit breaker are also included. Additionally, four measurements are made, including the phase current flowing to the

transformer, both in SI and pu, the voltage at the primary side of the transformer and the magnetic flux at its core. Additionally, these measures are also saved in the Matlab workspace with the use of a "To Workspace" block, to build the plots that are shown in this document.

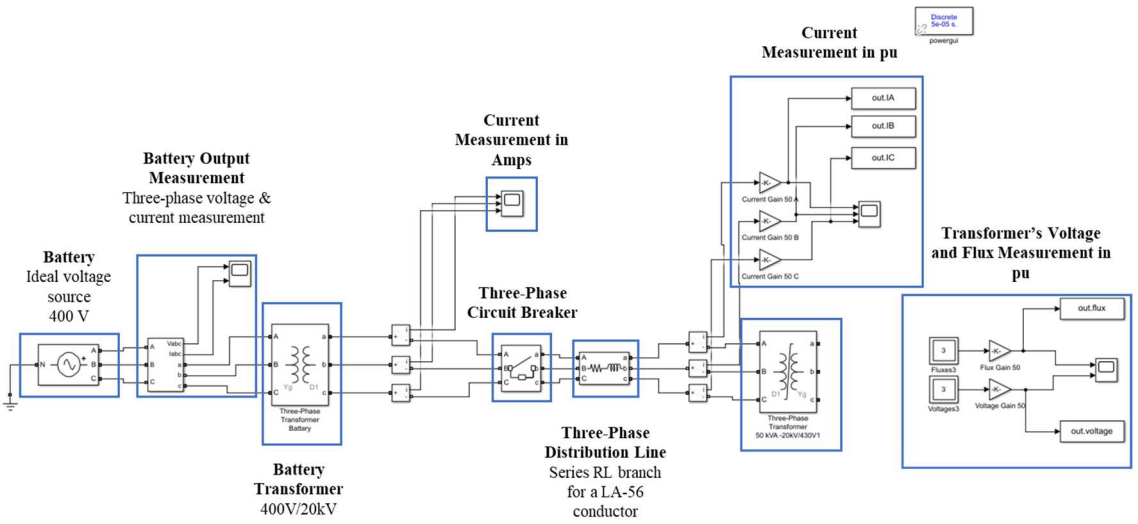

Figure 44. Simulink final schematic for the single three-phase transformer simulation.

The first analysis is carried out for an ideal case, where neither power lines nor the transformer connected to the battery are included, therefore obtaining the highest possible value for the inrush current.

Since the worst-case scenario takes place when the transformer presents an initial flux value that matches to its residual value at the energization instant, and the residual flux take place when de-energizing the transformers after a normal condition operation, the system must be initialized to correctly simulate the effect of the inrush currents.

The objective of the initialization is for the system to work in steady state operation, which basically involves the voltage and flux to be at their nominal values before opening the circuit breaker. For this purpose, a first simulation is going to be carried out and the final state of the simulation is going to be saved to be used as the initial conditions for the actual inrush simulations. For the initialization case, the breaker starts in open status. After one second, the circuit breaker closed. A first inrush current phenomenon takes place, but without considering the effect of the residual fluxes, so it is not representative for the overall simulations. The peak flux needs to be extinguished before the transformer is de-energized, therefore, the circuit breaker is opened after 100 seconds, which has been considered as a sufficient time for the flux transitory values at each phase to get extinguished, and for the residual values to get stablished at their nominal value.

Figure 45 shows the variation of the flux (up) and voltage (down) through time, both in pu. A first inrush current phenomenon when the circuit breaker is first closed at t=1s can be observed as well as the system, both flux and voltage, running in a steady state operation before the breaker opens at t=100 s. In Figure 46, where a detail of the last few seconds is shown, the flux getting stablished at the residual flux value can be seen. It can also be observed that two phases present residual fluxes with equal magnitude but with the opposite sign while the third phase does not present any residual flux, which can be explained since a three-phase system is energizing the transformer. Therefore, while the fluxes at two of the three phases are nearer to the saturation point and will thus remain at the residual flux point when de-energize, the other phase is nearer to the coercive current point, and thus, when de-energized, the flux at this third phase will present a zero value.

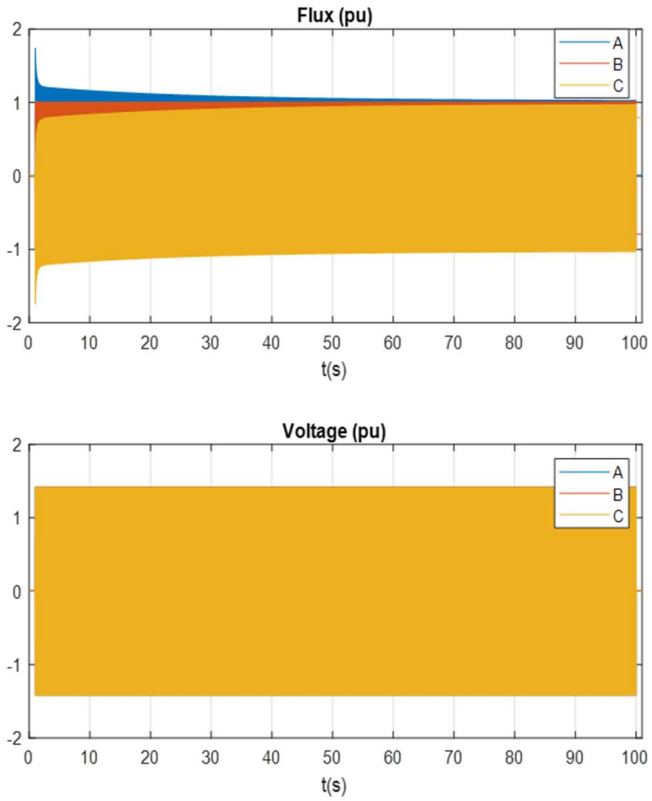

Figure 45. Previous energization of the transformer to reach the initial status for the residual flux of the transformer.

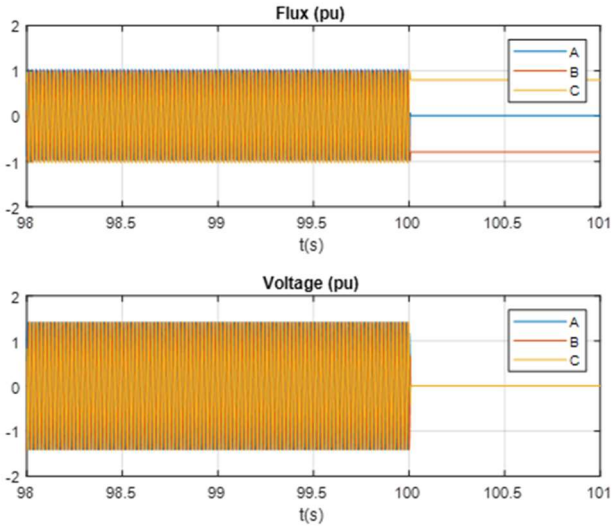

Figure 46. Detail of the last three seconds of the initialization of the transformer. Special focus on the residual flux of each phase.

Figure 47 shows a zoom from two complete cycles from the previously obtained results to get a further detail of the relation between the flux and the voltages at the transformer. Both the flux and the voltage present their nominal values. Besides, the 90º delay of the flux with respect to the voltage at each phase can be checked.

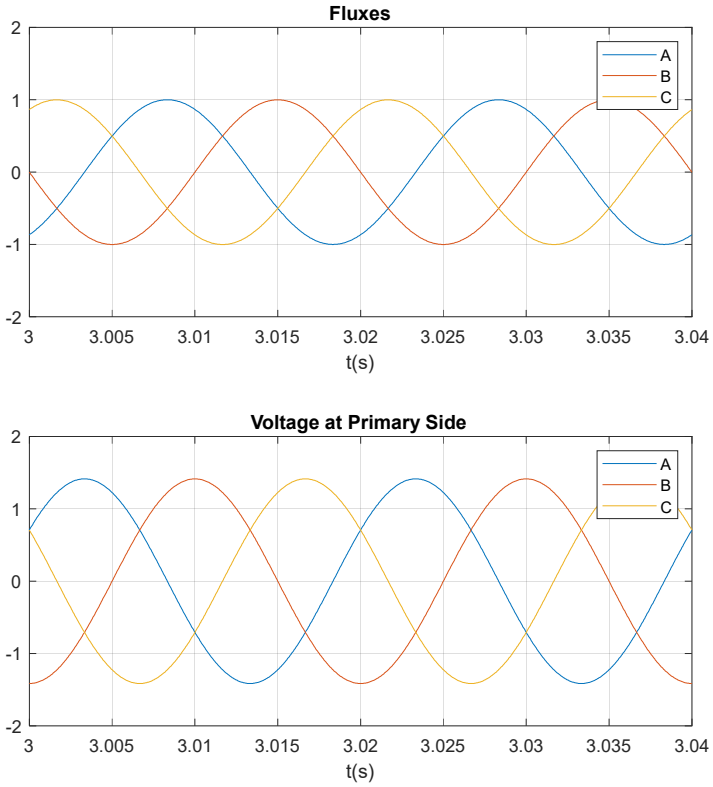

Figure 47. Detailed relation between the flux and the voltage at the primary side of the transformer.

Once the system has been initialized, the inrush current simulation is carried out. First, the worst-case scenario must be found. As explained in section 4.1, the inrush current is highly dependent of the triggering moment of the circuit breaker. Therefore, to get an understanding of the relation of the variation of the closing instant with the inrush current value, several simulations had been made by delaying the activation of the circuit breaker in 30º steps. In Table 1, the maximum phase-current values for each case are shown. The reference (0º) is set for when the voltage of phase A, which presents a zero-residual flux value, positively crosses the zero-voltage value.

Step	0º	30º	60º	90º	120º	150º	180º	210º	240º	270º	300º	330º
I_{max} (pu)	9.25	5.72	1.78	0.02	1.88	5.84	9.43	10.78	13.60	14.98	13.79	10.40

Table 1. Maximum phase current value in pu for each 30º step circuit breaker activation.

As seen from Table 1, the highest inrush current value, which coincides with the maximum inrush current value presented in [14], is obtained for a triggering delay of 270º, which corresponds to the point in which V_A is at its negative peak and V_B and V_C present an equal value. This delay is then going to be set in the circuit breaker as the predeterminate case for the inrush effect analysis.

Once the system is initialized and set to represent the worst-case scenario, the simulation is carried out. Figure 48 shows the voltage and flux values at the first few cycles after the closing of the circuit breaker. The obtained flux from the voltage of phase A (blue line) remains within its nominal value, since the circuit breaker is closed when the phase A voltage is at its absolute maximum value. Both the flux from voltages of phases B and C present a similar absolute maximum value about 2.35 pu.

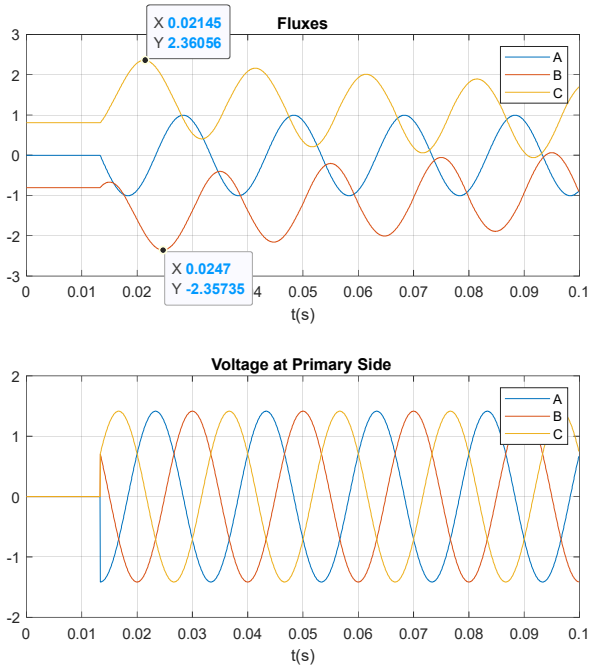

Figure 48. Flux and voltage of each phase at the primary side of the transformer for the first few energization cycles.

In Figure 49, the phase currents flowing to the transformer are shown in pu. As can be checked, the maximum inrush current is obtained from the current flowing through phase C, reaching a maximum value of almost 15 pu. The other two phases, B and C, also present very high values, reaching peaks of around 8 pu.

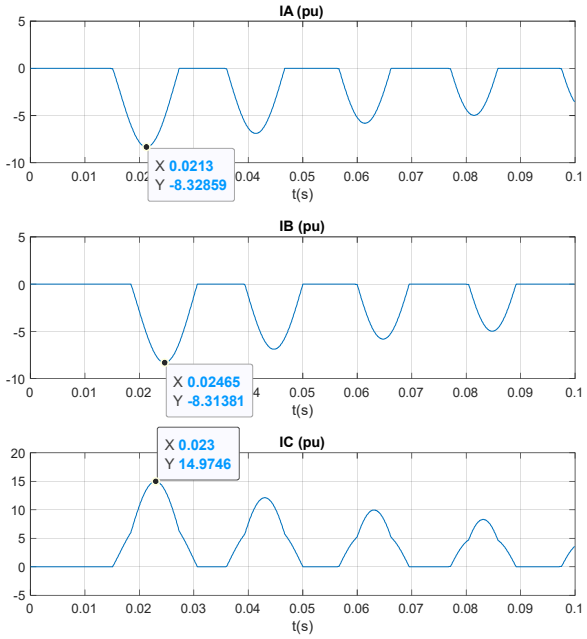

Figure 49. Phase current of each phase in pu at the primary side of the transformer for the first few energization cycles.

Additionally, Figure 50 show the inrush current transient for each of the three phases. The transient is extinguished in approximately one second, reaching its nominal value (1 pu) in around 0.42 seconds. For the R1 and L1 values that are presented in Table 12 of the three-phase

transformer section of ANNEX I, the estimate theoretical time constant, that can be obtained through (27) presented in section 4.1, presents an approximate value of 0.005 seconds. Therefore, considering five time constants for the transient to get extinguished, the total theoretical extinguishing time should present a value of 0.025 seconds. As discussed in section 4.1, this value is obtained under certain simplifications (linear magnetic characteristics and no core losses) and applied to a single-phase transformer. As has been proven, the time estimation under these conditions cannot be applied to a three-phase transformer. However, the exponential extinguishing curve shape is maintained.

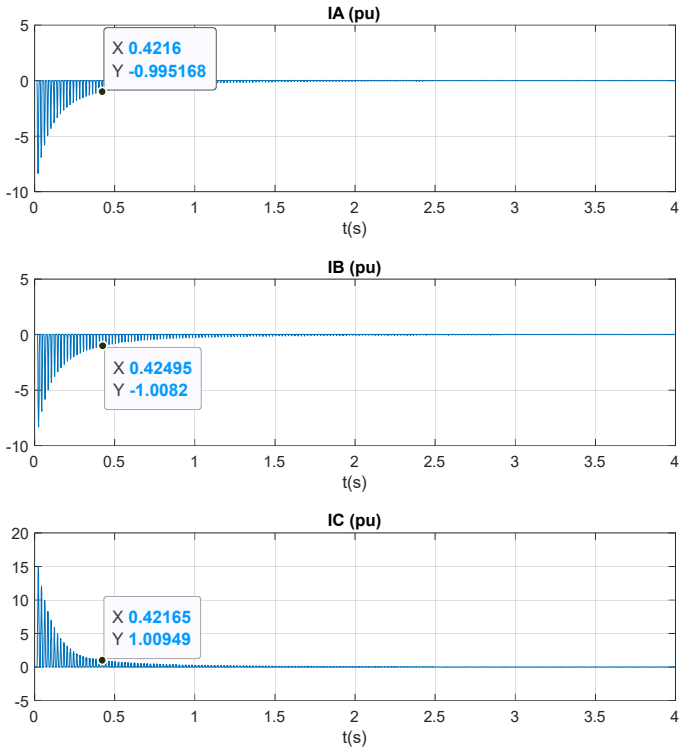

Figure 50. Inrush current transient for each phase.

It is important to clarify that the phase currents measured outside of the transformer, the ones that are going to be used in the protection relay triggering are not the same that the currents flowing through each of the transformer windings, since the primary side is delta connected. Thus, the presented results provide the highest possible current value through one of the three phases outside the transformer. However, the maximum current through one of the transformer windings do not correspond to this case. Instead, as seen in section 4.1, the highest current value flowing through one of the transformer's windings, corresponds to the instant at which the voltage of the phase which presents the highest residual value, is at its minimum absolute value (voltage value equal to zero).

Figure 51 and Figure 52 show a comparison between these two above-mentioned cases. Figure 51 presents the case in which the highest current value outside the transformer is obtained, while Figure 52 presents the case in which the highest current value at one of the transformer's windings is reached. Comparing both figures, it can be verified, that although the highest winding current value is reached for the maximum flux case, presenting a current value of 9 pu, the outside maximum phase current value is obtained for a different closing moment, presenting a winding

current value of 8.33 pu. In the end, what matters is the current flowing through the electric protection, that is going to coincide with the phase current outside the transformer, therefore matching with the worst-case scenario.

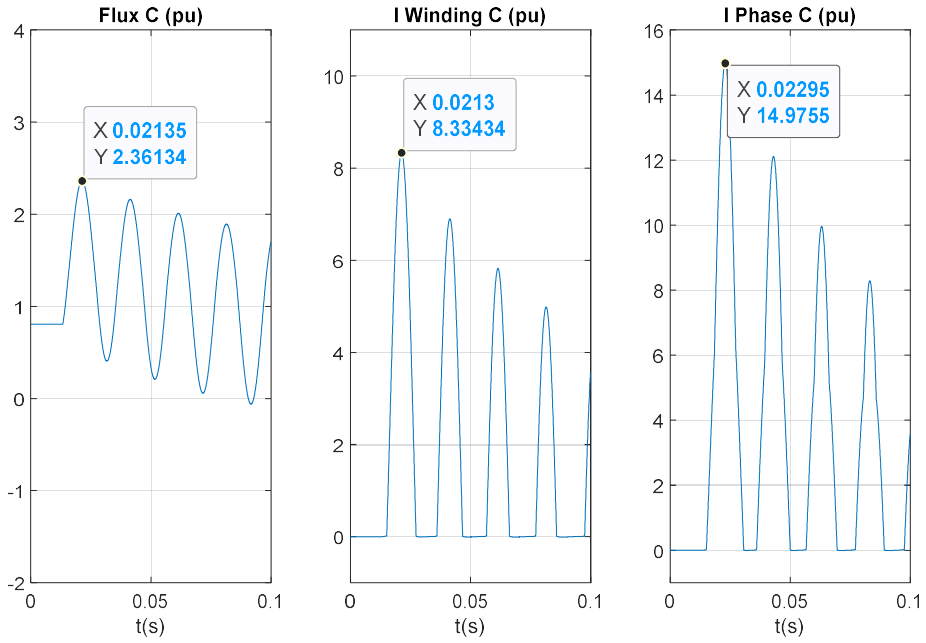

Figure 51. Flux (left), line current through the transformer winding (middle) and phase current (right) at the phase presenting the highest inrush current for the highest phase current case.

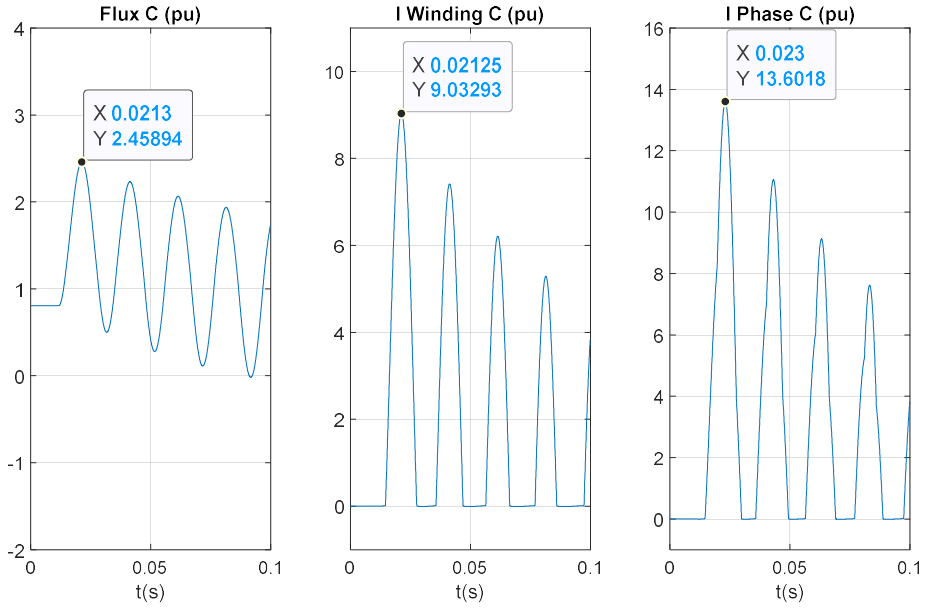

Figure 52. Flux (left), line current through the transformer winding (middle) and phase current (right) at the phase presenting the highest inrush current for the highest line winding current case.

Finally, it is important to mention that the operation of the other four transformers is equivalent to operation of the 50 KVA that has just been analyzed, but with the respective variation of the inrush maximum current value.

5.1.2. Transformer Operation in Parallel

In this section the effect of setting two transformers in parallel is shown since it supposes an in-between step to the Caravaca feeder simulation. The result of ideally connecting two transformers in parallel without any line in between, would be the summation of the inrush currents obtained in each of the transformers individually.

To check the effect of this solution, the simulation scheme, shown in Figure 53, has been built. This scheme includes the voltage ideal source, the three-phase circuit breaker and two transformers of 50 kVA and a 100 kVA, respectively. Additionally, the currents at each of the three phases have been measured in Amperes to check the inrush current values.

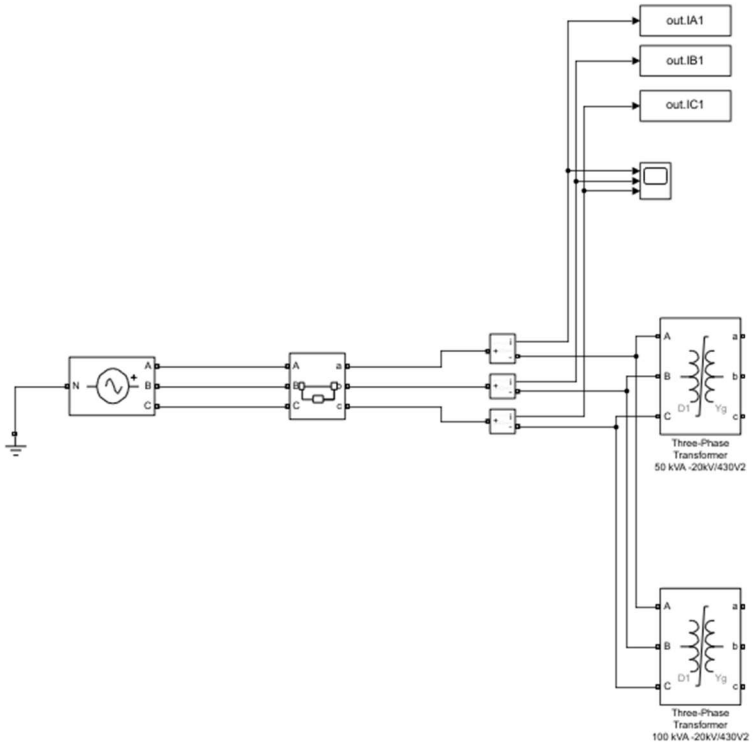

Figure 53. Simulink scheme for the simulation of two transformers in parallel.

Before the simulation results are presented, it is crucial to show the inrush current simulation for both transformers individually, to check the performed hypothesis. In Figure 54, the inrush current in Amperes for the 50 kVA (left) and 100 kVA (right) transformers is shown, where the maximum values reached by each transformer, corresponding to phase C, round almost 22 A and 40 A, respectively.

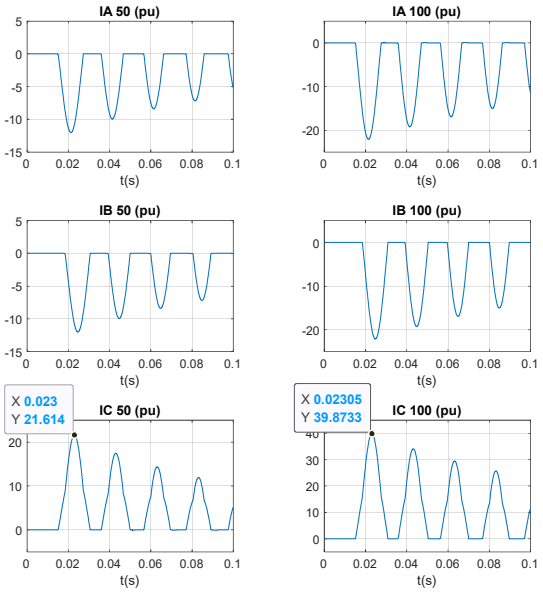

Figure 54. Inrush current values for the worst-case scenario for each of the 50 kVA (left) and 100 kVA (right) transformers individually.

The simulation results for the parallel connection of the 50 kVA and 100 kVA transformers are shown in Figure 55. The maximum inrush current value reaches a value of almost 62 A, which effectively coincides with the summation of the two inrush currents independently.

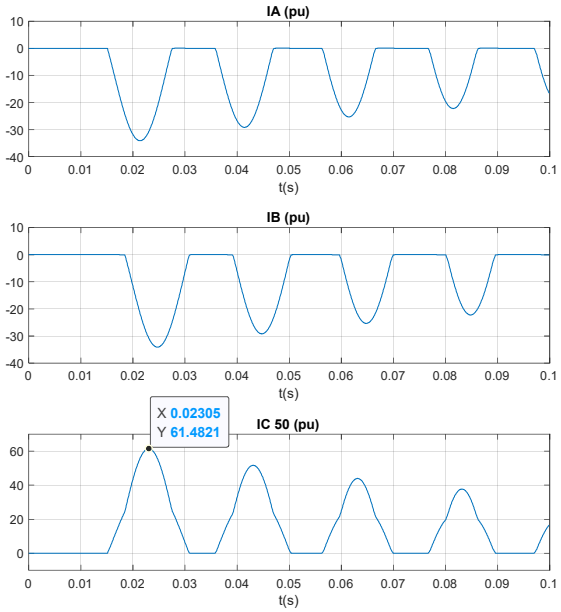

Figure 55. Inrush current values at each phase for the case of a 50 kVA and 100 kVA transformers in parallel.

The conclusion to this brief section is that, as an approximation, several transformers can be connected in parallel to emulate transformers of different nominal powers, than the ones introduced in the simulation with the data obtained from [14] and [15].

5.1.3. Analysis of the Line Inclusion Effects

In this section, a further step into a more realistic system is taken by including a series RL branch that represents the distribution lines that connect the battery with the transformers, which parameters are included in ANNEX I. Three simulations are carried out, each with a different distribution line length, including a 1 km, 10 km, and 50 km distribution line.

The results are presented in two different sections. First, the first few cycles are presented to check the effect of increasing the line length in the peak voltage, flux, and current values. As reviewed in section 4.1, the inrush current depends on the flux value on the magnetic core, while the flux is stablished by the voltage at the primary side of the transformer. Therefore, as shown in Table 2, which shows the overall results for this first section, the peak voltage, flux, and current values are directly related. Increasing the distribution line length leads to a reduction of the applied voltage to the transformer due to a greater voltage drop because of the increasing line losses, which implies a proportional reduction in the flux peak value and, finally, a reduction of the phase peak current, that is reduced in approximately 0.8 pu from a 1 km to a 50 km line.

Length (km)	1	10	50
Line peak voltage (pu)	1.413	1.408	1.370
Peak Flux (pu)	2.352	2.344	2.305
Phase Peak Current (pu)	14.856	14.700	14.038

Table 2. Results of the line inclusion simulation, including the line peak voltage, the peak flux and phase current for the line length variation.

Figure 56, Figure 57 and Figure 58 show the commented results for the first 0.1 seconds for the line length variation shown in Table 2, including 1 km, 10 km, and 50 km.

- 1 km:

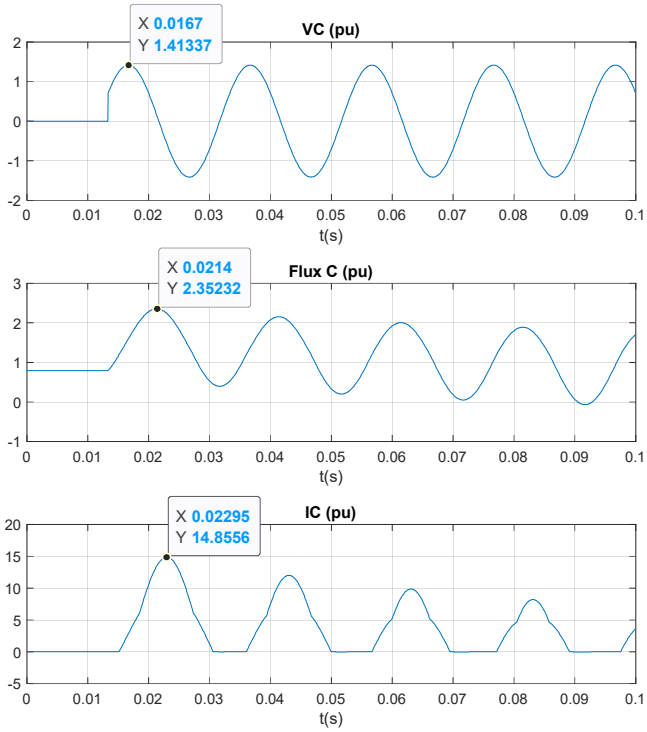

Figure 56. First 0.1 seconds of the energization of a single three-phase transformer including a 1 km length line.

- 10 km:

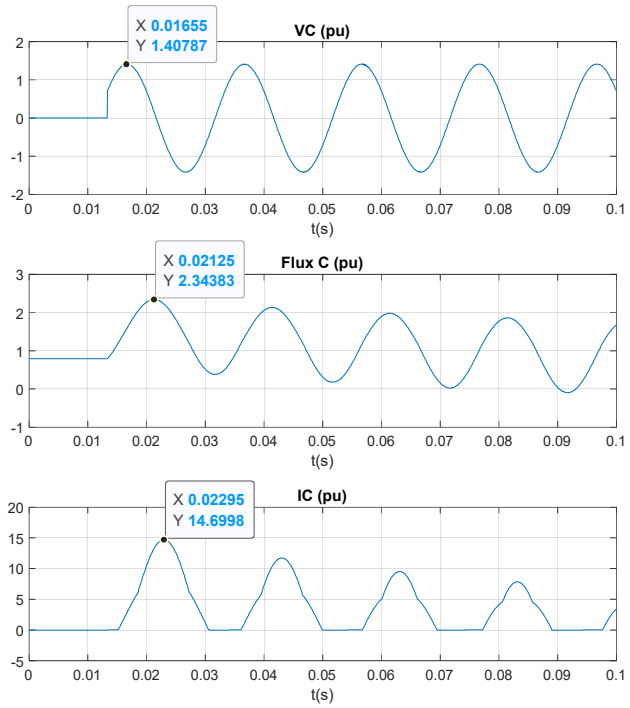

Figure 57. First 0.1 seconds of the energization of a single three-phase transformer including a 10 km length line.

- 50 km:

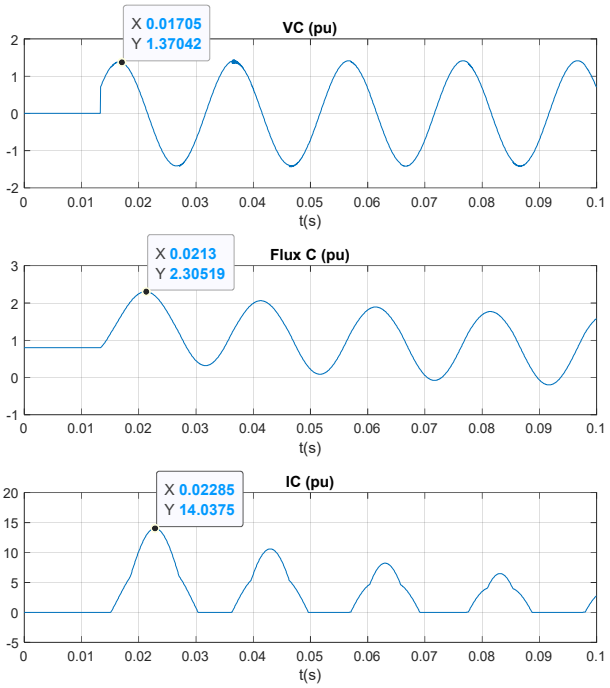

Figure 58. First 0.1 seconds of the energization of a single three-phase transformer including a 50 km length line.

The second section analyze the effect of increasing the line length to the inrush current transient. As seen from section 4.1, the exponential decrease of the inrush current is highly dependent of the series resistance and inductance components, therefore, increasing the line length, which basically correspond to an increase of the RL series parameters, will lead to a decrease of the transient extinguish time. Results of the simulations are summarized in Table 3, which show the results obtained from the three simulations that can be observed in Figure 59, Figure 60 and Figure 61, which correspond to the 1 km, 10 km, and 50 km simulations, respectively. The results shown in Table 3 include the time it takes for the inrush current to reach a peak current value equal to the nominal current (1 pu).

Length (km)	1	10	50
Decreasing time (s)	0.422	0.402	0.325

Table 3. Transient response variation for the line length variation.

As discussed in section 5.1.1, the time constant (L/R) obtained theoretically for a single-phase transformer fails to quantitative estimate the time it takes for the inrush currents to get extinguished. However, and based in the results of this section, it can be inferred that the time constant estimation presented in section 5.1.1 achieves a qualitative estimation of the extinguishing time. The parameters of the distribution line, which are included in the three-phase RLC branch section of ANNEX I, presents a R value of 0.688 Ω/km and a L value of 0.001378 H/km. The resistance value is approximately 500 times the inductance value per km, and therefore, for longer distribution lines, the difference between these parameters characterizes the reduction of the extinguishing time, that for these simulations goes from 0.422 s to 0.325 s.

- 1km:

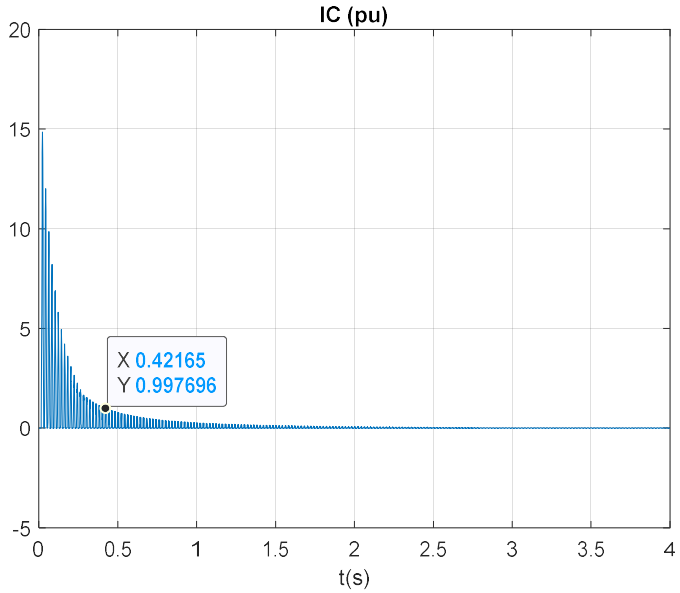

Figure 59. Inrush current transient for the energization of a single three-phase transformer including a 1 km length line.

- 10 km:

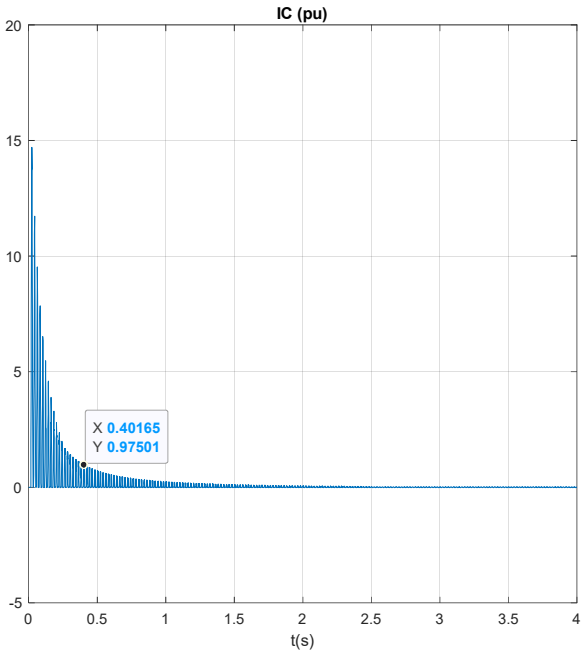

Figure 60. Inrush current transient for the energization of a single three-phase transformer including a 10 km length line.

- 50 km:

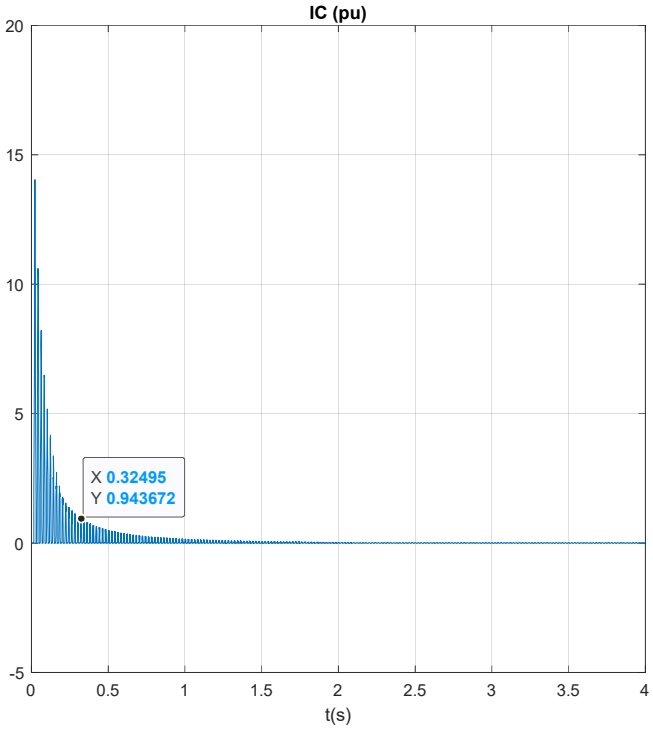

Figure 61. Inrush current transient for the energization of a single three-phase transformer including a 50 km length line.

5.2. SIMULATION OF CARAVACA FEEDER

In this section, the simulation of a real feeder from the Iberdrola network connected to the BESS facility of Caravaca de la Cruz is built, with the objective of analyzing the operation of a whole feeder instead of a single transformer.

Three main analyses are carried out. First, the effect of the voltage drop across the whole feeder on the energization of the transformers is studied. Secondly, the voltage conditions that lead to each of the initial flux cases are obtained. Finally, the effect of the closing instant of the circuit breaker for different initial flux conditions is analyzed.

Figure 62 shows the single-line diagram of the emulated feeder. This feeder is composed by a sum of eight transformers, all connected by the respective distribution lines, and powered by a 400 V ideal source connected to the feeder by a 400V/20kV transformer. The 400 V ideal voltage source represents the battery energy storage system. The distribution line lengths, as well as the nominal power for each of the feeder's transformers are depicted in the single-line diagram. The distribution line parameters are described in ANNEX I. "CB" represents the circuit breaker at the top of this feeder, which corresponds to a remote controlled three-phase circuit breaker. The nine red dots indicate the measurement points, where both the line voltages and phase currents are measured.

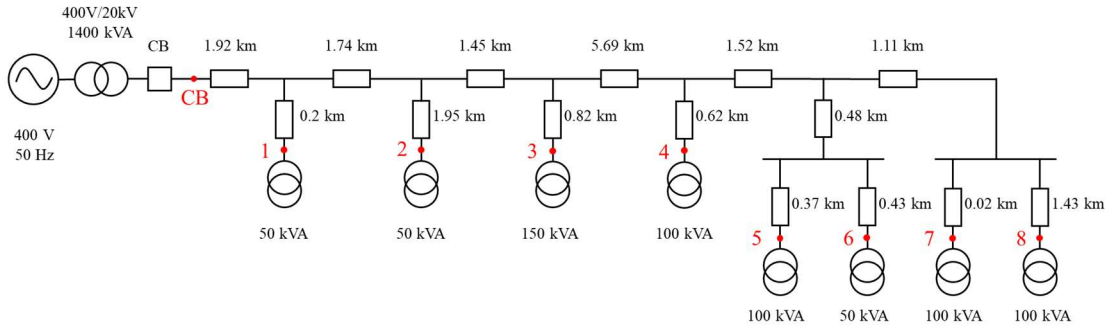

Figure 62. Single-line diagram for a real feeder from the Caravaca facility.

Figure 63 show the Simulink schema used for the simulations of this section. The highlighted blue squares "1" and "2" represent the phase current and line voltage measurements at the 20 kV side of the battery transformer, respectively. The blue square "3" presents the block that includes the phase IDMT relay, which input corresponds to the three-phase currents at the top of the feeder and which output triggers an additional circuit breaker that represents the protection switch. The blue square "4" represents one of the transformer sets, which include the three-phase saturable transformer, the respective distribution line section and the three-phase current measurement. Finally, for each transformer a set of voltage and flux measurements are included in square "5".

At this point of the analysis is important to mention the different protection relays that are included in the Caravaca facility while operating in islanding mode. There are 4 different relays that trigger the same circuit breaker at the top of the system, which include the 4 independent feeders. Additionally, there is an internal BESS protection limiting the instantaneous current inside the inverter.

Table 4 collects all the relays parameters of the main circuit breaker.

Protection Relay	Characteristic	Pick-Up Current (A)	TMS
Phase IDMT - 51	IEC Very Inverse	54	0.5
Phase Instantaneous Overcurrent - 50	Fixed Time	300	-
Neutral IDMT - 51N	IEC Very Inverse	9	0.5
Neutral Instantaneous Overcurrent - 50N	Fixed Time	42	-
BESS Instantaneous Overcurrent - 50	Fixed Time	40	-

Table 4. Relay configuration parameters of the main circuit breaker.

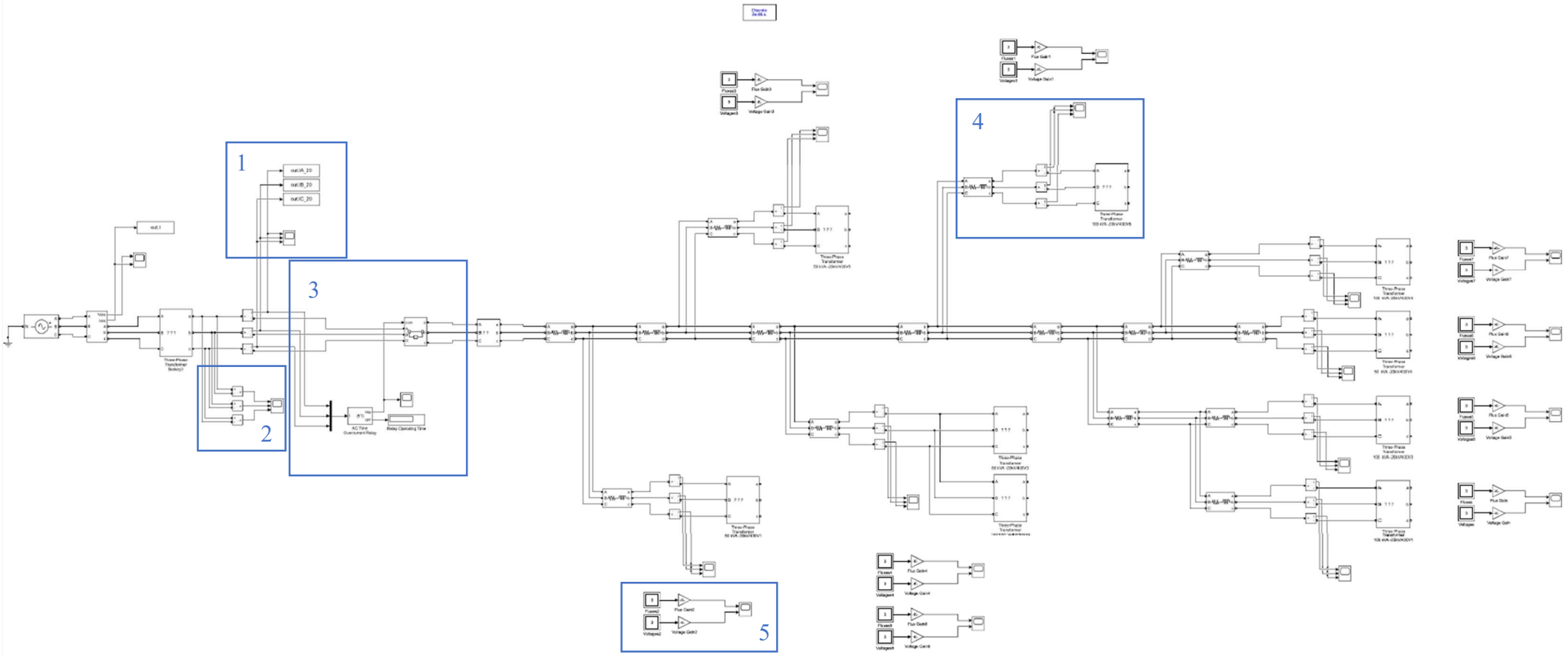

Figure 63. Simulink schema for the real Caravaca feeder simulation.

5.2.1. Voltage Drop Effects

The objective of this first simulation is to see how the voltage drop across the feeder affects the inrush current of each transformer and the overall effect at the whole feeder. For this purpose, measurements in the feeder include the voltage at the primary side as well as the maximum inrush current value flowing to each transformer. The simulation is carried out to emulate the worst-case scenario, scilicet, when the inrush current value for each of the transformers forming the feeder reaches the highest possible value. The measured inrush current is also compared to the maximum inrush current of each transformer, which is indicated in the transformer datasheets [14], [15] and [16], to check the reduction of the inrush current value. Table 5 shows the results of the simulation, where the measured voltage corresponds to the peak voltage value reached at the first cycle after closing the circuit breaker, and, presenting the source a voltage value of 1 pu. As has been proven in section 5.1.1, transformers are emulated to match the maximum current presented at the manufacturer datasheets.

Point	Description	Voltage (pu)	Datasheet Current (A)	Measured Current (A)	Reduction (%)
1	Measurement of 50 kVA transformer	0.889	22	17.719	19.46%
2	Measurement of 50 kVA figuretransformer	0.875	22	17.480	20.55%
3	Measurement of 150 kVA transformer	0.864	62	48.742	21.38%
4	Measurement of 100 kVA transformer	0.846	40	30.029	24.93%
5	Measurement of 100 kVA transformer	0.841	40	29.673	25.82%
6	Measurement of 50 kVA transformer	0.841	22	16.124	26.71%
7	Measurement of 100 kVA transformer	0.829	40	29.606	25.99%
8	Measurement of 100 kVA transformer	0.827	40	29.522	26.20%
CB	Measurement at the top of the feeder	0.902	288	219.070	23.93%

Table 5. Simulation results, including, for each of the measurement points, the voltage, the estimated and the measured current as well as the current reduction.

As has been proved in previous sections, the inrush current is highly dependent on the voltage value through the means of the flux. As seen in Table 5, the huge current values presented at the energization of the transformers leads to a huge decrease of the voltage at the primary side of the transformers because of the losses increase in the distribution lines. Therefore, the longer the distribution line connected to the transformer, the lower the voltage at the primary side when closing the circuit breaker. This consequence can be verified by comparing, for instance, point 1 to point 8, corresponding to the first and last transformers respectively. Point 1 and 8 present a voltage value of 0.889 pu and 0.827 pu respectively. However, these temporary increase of the distribution losses causes a beneficial result for the feeder connection since the overall inrush current is decreased by a 24%, as seen from the CB measurement point. Finally, it is important to highlight that, the more downstream a transformer is in the distribution feeder, the higher the reduction of the inrush current is going to be presented, due to the lower voltage value at the transformer.

As for the previous cases, it is also interesting to look at the transient response of the inrush current. Figure 64 show the transient response of phase A inrush current, which corresponds to the phase with the highest inrush current peak value. For this case, the nominal current value considered for the base current value, matches with the nominal current value of the battery transformer (400V/20kV). Therefore, for a nominal power value of 1400 kVA, the nominal current for this feeder can be computed by (75).

$$I_n = \frac{S_n}{\sqrt{3}U_n} = \frac{1400}{\sqrt{3}\cdot 20} = 40.41\ A \tag{75}$$

In this case, it takes nearly 0.13 seconds for the inrush current value to reach the nominal current value. Compared with the case presented in section 5.1.3, where just one transformer and line were considered, the extinguishing time is reduced from 0.32 to 0.13 seconds. Following the conclusions inferred in section aa, the longer the RLC branches that are connected to the transformers, the less time it takes for the transient to get extinguished. Overall, the total time for the inrush currents to get extinguished is about 1.3 seconds.

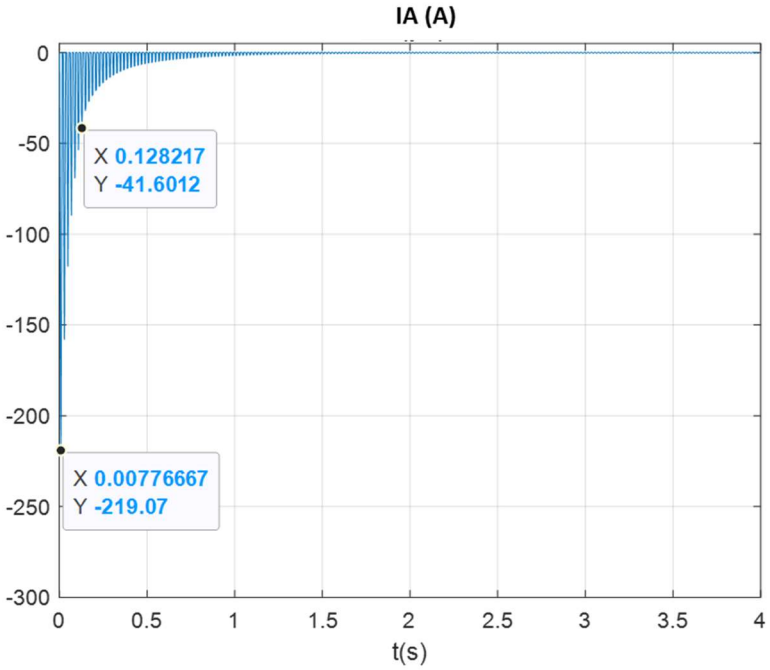

Figure 64. Transient inrush current response of phase A for the real feeder simulation.

5.2.2. Initial Flux Conditions

Once the effect of the voltage at the primary side of the transformers has been proved, it is time to analyze the effect of the circuit breaker closing instant on the inrush current value.

As seen in section 4.1, the inrush current is highly dependent on the initial residual flux value. Before opening the circuit breaker, a three-phase equilibrated system in steady state is considered. Thus, for any opening instant, and following the B-H curve of the material, two of the three phases are going to remain with the remanent flux value (one in opposition to the other), while the third

phase is going to present a zero remanent flux value. Six possible combinations are then possible for the initial flux condition, therefore defining six initial cases for this section.

In the simulations, it does not suppose a problem to look at the initial flux conditions, since it only requires setting a measurement in each transformer capable of registering the flux inside the transformer. However, measuring the initial flux conditions in a real feeder is much more complicated, since the flux measurement is not straightforward, and it will require to install a measurement device in each transformer. Therefore, it is interesting to find a relation between the voltage at the top of the feeder with the initial flux condition of the transformers of the feeder.

In this next simulation, this relation is obtained.

For this simulation, the disconnection of all the transformers at the same time is going to be considered, since the disconnection is going to be done with the circuit breaker at the top of the feeder. As seen later in the results, this leads to the same initial flux conditions for each of the transformers in the Caravaca feeder, since the voltage at the primary side of all transformers of the feeder are nearly the same. This voltage equality is strengthened because of the no-load condition at the initialization process. Twelve simulations have been carried out for the described purpose. Each of the simulations corresponds to a 30º step delay with respect to the instant at which the line voltage V_{ab} is positively crossing the zero value at the 20 kV side of the battery transformer. The twelve 30º step simulations permits to cover a wide spectrum of possible initial conditions for a whole cycle, thus having all the possible combinations covered.

Figure 65 shows the three-phase flux values for the opening instant of the circuit breaker for both the first and the last transformers of the feeder. From this result, it can be supposed that transformers for the whole feeder maintain the same residual fluxes if disconnected at the same point in time.

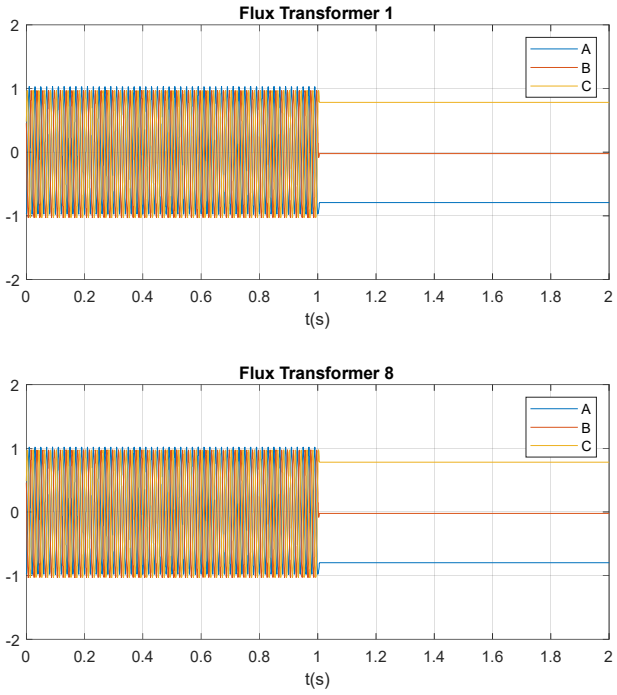

Figure 65. Flux initial condition for transformers 1 and 8, located at the beginning and end of the feeder, respectively.

Table 6 shows the residual flux at each of the three phases (A, B and C) for each of the circuit breaker opening cases (in 30º steps). The residual flux value coincides with the residual flux nominal value. In each case, a positive, negative and zero residual flux values are presented. As abovementioned, 6 cases are obtained, each case consisting in two different opening instants.

Steps		0º	30º	60º	90º	120º	150º	180º	210º	240º	270º	300º	330º
Initial Flux Condition	**Flux A**	-	0	0	+	+	+	+	0	0	-	-	-
	Flux B	0	-	-	-	-	0	0	+	+	+	+	0
	Flux C	+	+	+	0	0	-	-	-	-	0	0	+
Initial Case Nº		1	2	2	3	3	4	4	5	5	6	6	1

Table 6. Initial flux condition at each phase for each of the circuit breaker opening cases.

With these results, the initial flux conditions are matched to the voltage values at the 20 kV side of the battery transformer, being an easier measurement to be made in real conditions.

5.2.3. Circuit Breaker Closing Effects

Once the initial flux conditions had been analyzed, it is important to see the effects of closing the circuit breaker in different moments, therefore energizing the transformer for different voltage waveform conditions.

With this purpose, for each of the obtained 6 initial flux cases, 12 simulations had been carried out, by closing the circuit breaker in 30º delay steps with respect to the instant at which the line voltage V_{ab} is positively crossing the zero value at the 20 kV side of the battery transformer. Results from these simulations are shown in Table 7. Each row corresponds to a different initial flux case, corresponding to the ones shown in Table 6. Each of the columns corresponds to one of the 12 different circuit breaker closing instants. The dark-red colored cells represent the highest inrush current values matching with the worst-case scenarios for each case, while the dark-green colored cells represent the lowest inrush current values. The inrush current values range go from around 230 Amps, to a nearly zero value.

		Circuit Breaker Triggering Steps											
		0º	30º	60º	90º	120º	150º	180º	210º	240º	270º	300º	330º
Initial Flux Condition	Case 1	30.941	0.314	27.497	85.181	139.190	159.287	197.952	219.070	203.876	153.424	137.280	87.820
	Case 2	141.481	91.810	31.261	0.307	28.356	84.094	140.043	159.451	201.937	223.718	208.175	159.246
	Case 3	212.963	164.240	141.336	90.387	30.335	0.293	29.248	90.925	145.057	165.057	207.445	228.950
	Case 4	207.896	228.536	213.285	163.351	135.118	85.960	23.944	0.298	34.328	96.577	150.288	170.530
	Case 5	149.937	169.269	200.800	222.945	207.914	159.057	131.473	81.365	25.606	0.318	34.103	94.512
	Case 6	33.972	88.617	142.794	163.455	197.965	219.437	203.537	154.124	132.718	81.600	25.681	0.312

Table 7. Inrush current maximum value in A for each of the initial flux condition and circuit closing case.

From the results of these simulations, two main conclusions can be drowned. First, with the objective of minimizing the inrush current value, it is not possible to select a single instant to close the circuit breaker, since, depending on the initial flux condition, each of the closing instants is, at one or another initial case, close to the worst-case scenario, presenting very high inrush current values. Furthermore, the worst-case scenario closing instant for one initial case coincides with the best-case scenario for another initial case, where the inrush current phenomenon does not take place. Secondly, the results of Table 7, it can be stated that, if the initial flux case is known, it is possible to close the circuit breaker in an instant in which the inrush current effects are minimized and even removed.

In the light of the results obtained for the feeder simulation, an estimation of the maximum inrush current that could take place during the connection of a determinate feeder is achieved, including the approximate effects of the connection of the transformers to the distribution network. Therefore, the behavior of the feeder energization for feeders with different characteristics is achieved.

Finally, it is important to mention that the IDMT relay did not trigger the protection any of the simulated cases, since the inrush currents follow a rapidly extinguished exponential as seen in Figure 64. However, the instantaneous current limitation of 40 A that the BESS includes is reached for most of the cases, and would then, trigger the inverter's internal protection. In addition, it is also important to remember that the simulations are carried out for just one feeder independently, which highly reduces the effect of connecting the four feeders at the same time or connecting feeders while other feeders are operating under normal conditions.

6. ANALYSIS OF THE FIELD TEST RESULTS

In addition to the Matlab simulations presented in section 5, experimental test at the Iberdrola BESS facility at Caravaca de la Cruz, had been carried out for the purpose of this thesis. In this following section, the field test results are going to be discussed with the objective of validating some of the conclusions drawn from the previous analyzed simulations. First a brief description of the Caravaca facility is going to be carried out, followed by a description of the field test that where developed, to finally analyze the obtained results.

6.1. Facility Description

The facility in which these tests had been carried out is located around the village of Caravaca de la Cruz in the province of Murcia, Spain. Historically, this part of the distribution network had regularly suffered from the negative effects of power cuts caused by line interruptions. Hence Iberdrola decided to install a BESS to provide the clients around this facility with energy even when the power lines failed, and thus being inevitably disconnected from the power grid.

The islanding operation since the BESS was installed has resulted in a local decrease of the local SAIDI index of around a 90%. In addition, when the BESS system is connected to the power network while normal operation, the BESS provides voltage support through reactive power variation.

The BESS can provide 2 MWh of electric energy presenting a nominal power of 1.25 MW at a nominal voltage of 400 V and is connected to the power grid by a 400V/20kV transformer of 1.4 MW nominal power.

Figure 66 shows a schematic description of the Caravaca BESS facility. The triangle-shape plot includes a telecommunications antenna (5) and the telecommunications distribution center (6), which enables the connection of the facility to the telecommunication private network of Iberdrola, permitting the monitoring and control of the whole facility, including both the BESS system and the remoted controlled circuit breakers of each feeder. The secondary substation (7) includes the auxiliary services transformer with its corresponding cell, the measurement and power transformer cell, the overhead to underground cables cell and each of the feeder's cells in addition to the required electric protections triggering the circuit breaker connected to the power transformer. At the right of this facility the 400V/20kV power transformer (8) is located in addition to the BESS containers (12). Finally, at the right side of the facility's schema, two medium voltage (20 kV) power lines (13 & 14) are presented.

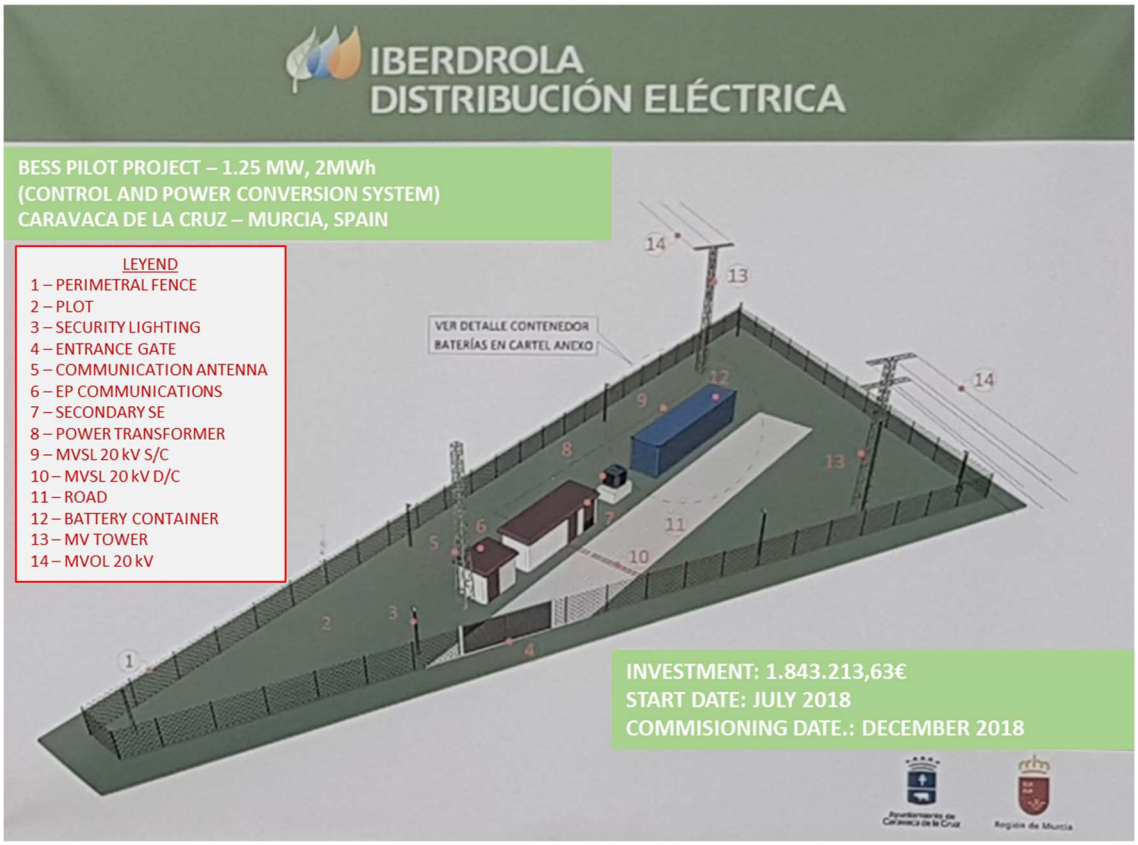

Figure 66. Pilot BESS Caravaca project facility scheme.

In Figure 67, a schematic showing the BESS system layout is presented. The container where the BESS system is located can be divided in two main parts. The first container incorporates the inverter, the control elements as well as the protection elements, which includes both electrical and physical protections (such as fire, temperature, or presence protections). The second container includes 28 battery modules which are connected in parallel, each one of these modules inside a different cabinet as shown in Figure 68. These modules are likewise composed by 17 submodules connected is series reaching the input inverter DC voltage of 400 V. Each one of these modules is controlled by a Battery Management System (BMS), which oversees both the temperature and voltage of each module, as seen at the top of Figure 68. The temperature of the battery modules is a critic parameter in the well-functioning of the battery submodules. The battery room temperature must be maintained at 23 ºC with a ±5º C range. As seen in Figure 68, the room's temperature is precisely maintained at 23 ºC, the optimum temperature for the battery operation.

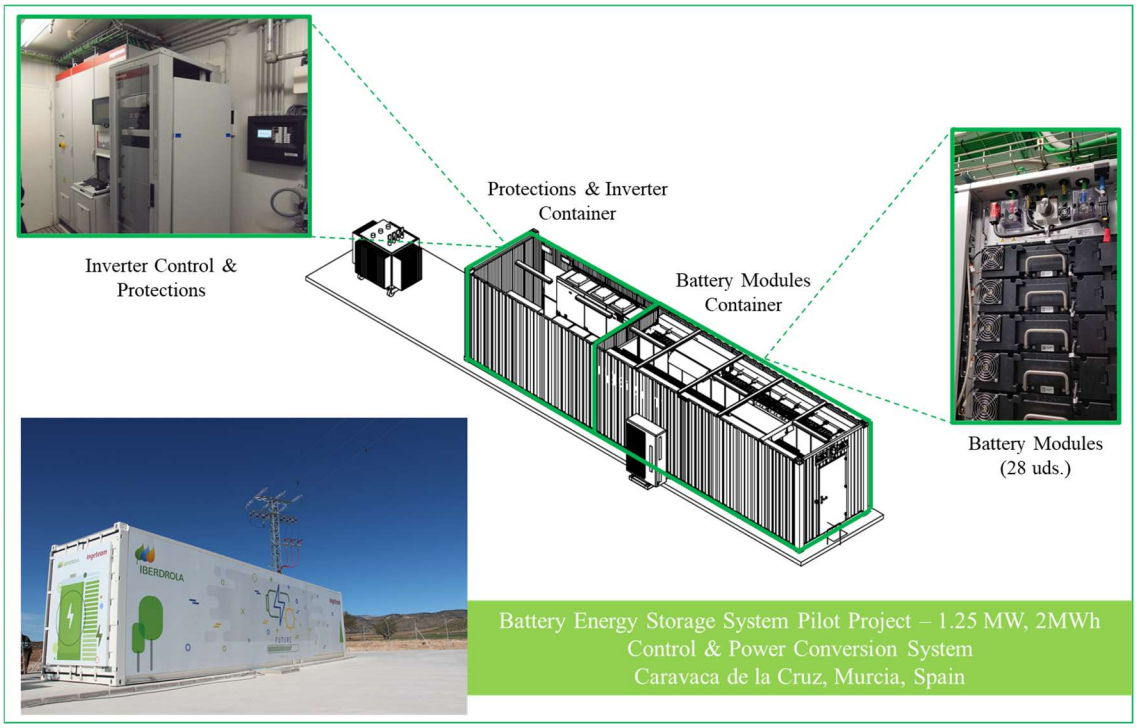

Figure 67.Pilot BESS Caravaca project battery container scheme.

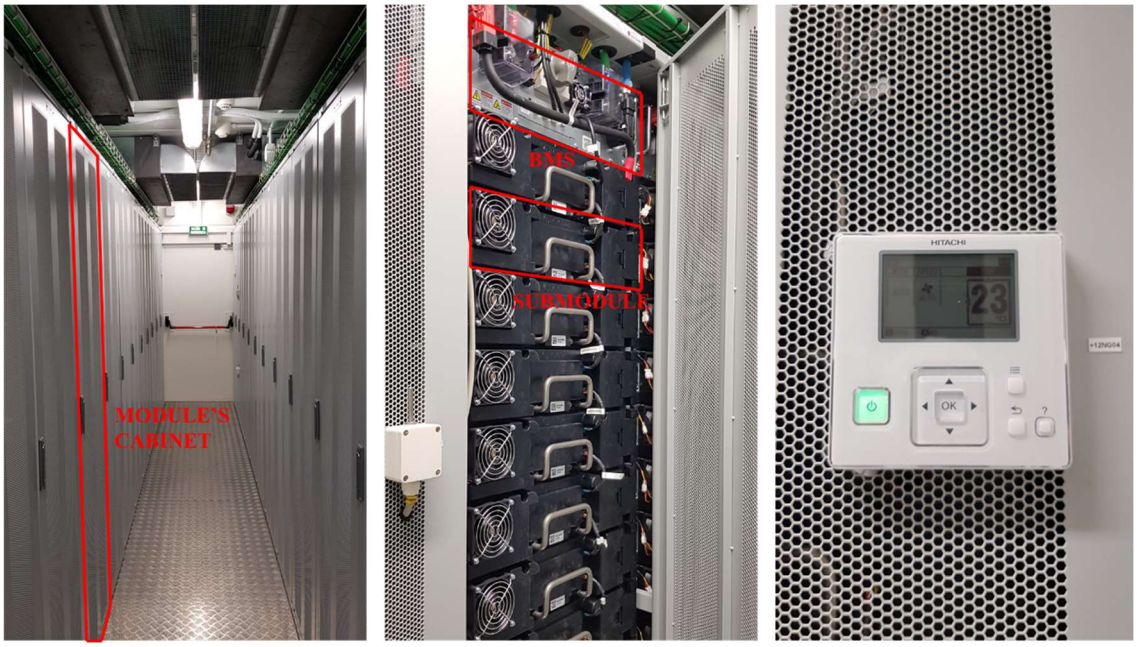

Figure 68. Inside of the BESS container. Module's cabinets (left), submodules & BMS (middle), and thermostat (right).

It is important to highlight that the inverters operation is mainly temperature-limited by the heat that can be extracted from the IGBT transistors, and therefore, a main component of the first container is the liquid refrigeration used for this purpose and shown in Figure 69, where also the air-refrigeration system for the batteries container is shown. Additionally, three CO2 containers are located inside the control & inverter container, which are used for fire extinguishing purposes when fire is detected in one of the two containers. Within the control system, some of the most

important components shown in Figure 69, include the inverter's control, the zero-crossing register, the air conditioner control system, the telecommunications switch, remote controlled circuit breakers, a main relay overseeing the operation of the battery, which is triggered if the voltage or temperature values get out of the imposed limits or if fire is detected. Additionally, an industrial PC is included in the control room to get data of the BESS status, including telecommunications, voltage and temperature real time and historical information. This information is displayed in several tabs in a monitor that can be controlled from the inside of the container, serving as the user interface. One of these tabs is shown in Figure 70, where, for instance, the temperature control tab is presented.

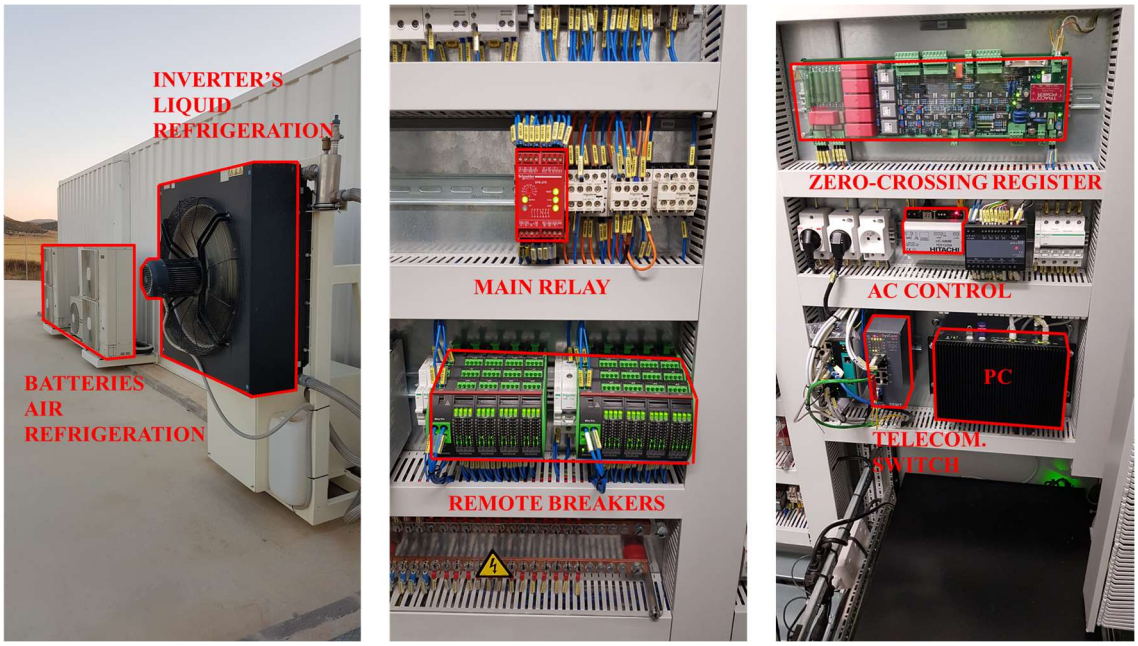

Figure 69. Refrigeration for the batteries & inverters (left), and inverter's control elements (middle and right).

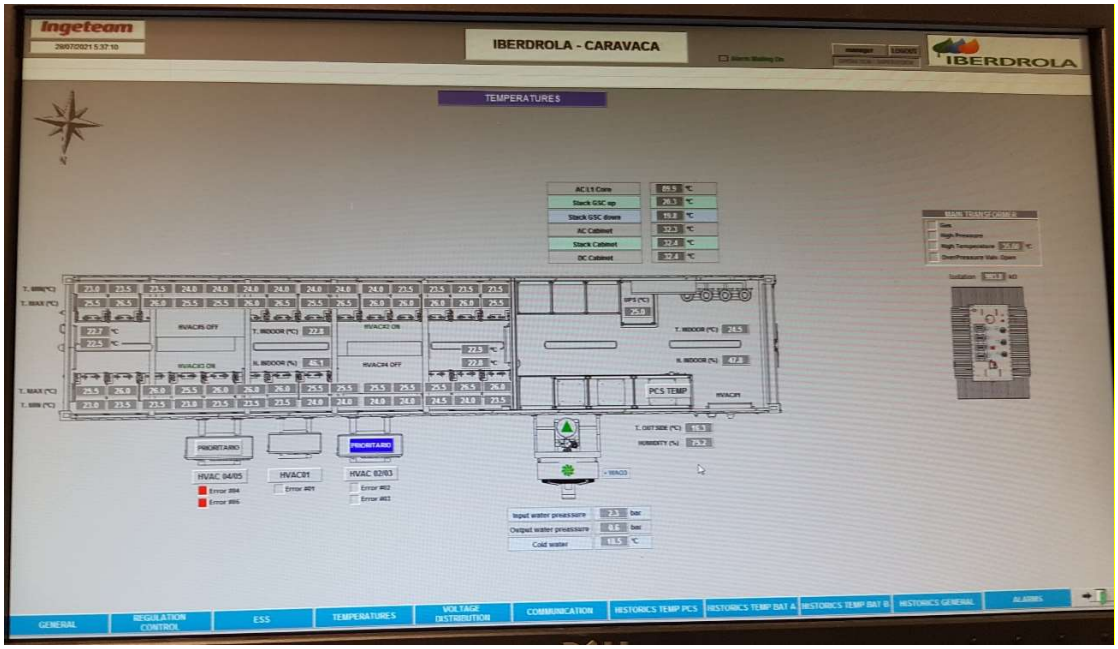

Figure 70. User BESS interface. Temperature control tab.

For the field test carried out for this section, the measurements were made inside the secondary substation with a digital recorder that registers both the voltage and current waves whenever a relevant event takes place. As seen in Figure 71, the digital recorder requires both current and voltage measurement connections that are linked to the "meter" cell of this facility, which basically consist in voltage output terminals that are used for the register connection. The current is measured through current clamps to each of the three phases. In addition, 3 feeder's cells, a measurement cell, the overhead to underground line cell and the power and auxiliary services cells are included in the secondary substation, which are shown in Figure 71, in addition to the protections relay.

Figure 71. Inside of the secondary substation. Digital recorder connections (left), and various cells (middle and right).

6.2. Tests Description

The obtention of experimental data to analyze the real effects of the inrush current is done by testing the operation of the Iberdrola BESS facility at Caravaca de la Cruz. The installed BESS represents an energy source for many consumers. The carried-out tests require, in most of the cases, to disconnect part of the consumption for some time, since the inrush current takes place when re-connecting a feeder that was previously de-energized. The power cuts originated to the consumers is the main reason for the limitations of these experiments. In addition, for Iberdrola, the BESS Caravaca facility is a pilot project to research the use of BESS for islanding operation in the grid, and, therefore, has its own interests in these experimental tests. The cases that had been tested correspond to Iberdrola's requirements and investigations. In addition, another limitation is found in the measurement device. For the obtention of the results, the Hioki 3196 Power Quality Analyzer has been used. This digital recorder is used to monitor and record any relevant event that takes place in the network. The main limitation involving this device is that it only records the voltage and current values in case of an event such as a voltage drop, sag, flicker, etc. Therefore, if the Hioki-3196 does not detect the objective event, no data will be available for a future analysis.

The recorded data can only be analyzed through the HiVIEW program, which is a software provided by the manufacturer, Hioki. This software allows a detailed analysis of both the voltage

and current in the case of an event taking place. All the figures presented in the following section are directly obtained from the HiVIEW interface.

Once the limitations of these tests and the measurement procedure has been reviewed, it is time to take a further look to the actual test that had been carried out at the BESS facility. Seven different tests had been carried out that can be useful for the development of this thesis. All follow the same structure. In the first place, the system is operating in islanding mode with a determinate load that is going to be characterized by the total nominal load connected to the BESS, which characterizes the previous nominal power supported cases. From this stable operating point, an additional feeder is connected to the BESS by closing a specific circuit breaker, which supposes the inclusion of an additional nominal power to the system, and which characterizes the nominal power addition cases. Besides, the manufacturer of the BESS has implemented an algorithm to improve the robustness of the islanding operation mode for the connection of feeders with a larger consumption. The programming details of this algorithm are not available since the manufacturer strategy to protect its product from unwanted intrusions is to share no information about it. However, in general terms, this algorithm is based on a voltage variation at the energization instant to allow a larger consumption to be connected without overreaching the current limitation that triggers the battery's protections.

Table 8 summarizes the description of the seven tests, including the nominal power in kVA previously supported by the BESS system as well as the nominal power in kVA to be added through the CB closing. In addition, the status, active or inactive, of the BESS voltage variation-based algorithm and the number of repetitions of each test is presented.

No.	Previous Nominal Power Supported (kVA)	Nominal Power Addition (kVA)	Inrush Current Algorithm	Repetitions
1	2933	858	Inactive	1
2	1779	1154	Inactive	1
3	2933	858	Active	1
4	1779	1154	Active	1
5	2808	3230	Active	4
6	5342	696	Active	4
7	2708	4224	Active	5

Table 8. Field tests description including the previous and added nominal power in kVA, the algorithm status, and the number of repetitions.

6.3. Results Analysis

Two main analyses can be differentiated. On the one hand, the first four cases are useful to give an overview of the inrush current phenomenon and a comparison of the effects of including the BESS inrush current algorithm. On the other hand, the last three cases are used to analyze if significant differences are presented if the circuit breaker is triggered at different instants.

First, the first four cases are going to be analyzed. These four cases correspond to two different configurations. Cases 1 and 3 and cases 2 and 4 correspond to the same configuration respectively. In cases 1 and 2, the control algorithm is deactivated while in the remaining two cases, the algorithm is activated, which permits to develop a side-by-side comparison between cases 1 and 3 and cases 2 and 4, therefore verifying the effects of this algorithm.

Figure 72 and Figure 73 correspond to the comparison of cases 1 and 3 and 2 and 4 respectively. For the 4 cases shown in Figure 72 and Figure 73, the voltage waveform is presented at the top, at a scale of 5 kV/division, and the current waveform is presented at the bottom at a scale of 12.5

A/division. The x axis of the graphs represents the time with a scale of 20 ms/division, which corresponds to a full cycle per division. The red, green, and blue lines represent phases A, B, and C respectively. The vertical red line that is shown for cases 3 and 4 (graphs at the right), represent the circuit breaker closing instant.

Cases 1 and 3 and cases 2 and 4 correspond to the same feeder configuration respectively. However, in cases 1 and 2, the voltage control algorithm is not active while in cases 3 and 4 this algorithm is active.

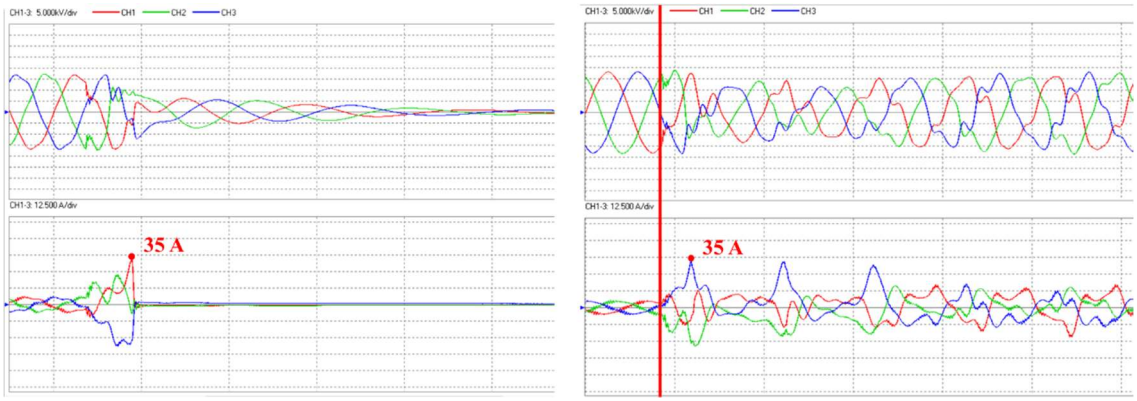

Figure 72. Voltage and current waveforms comparison for cases 1 (left) and 3 (right).

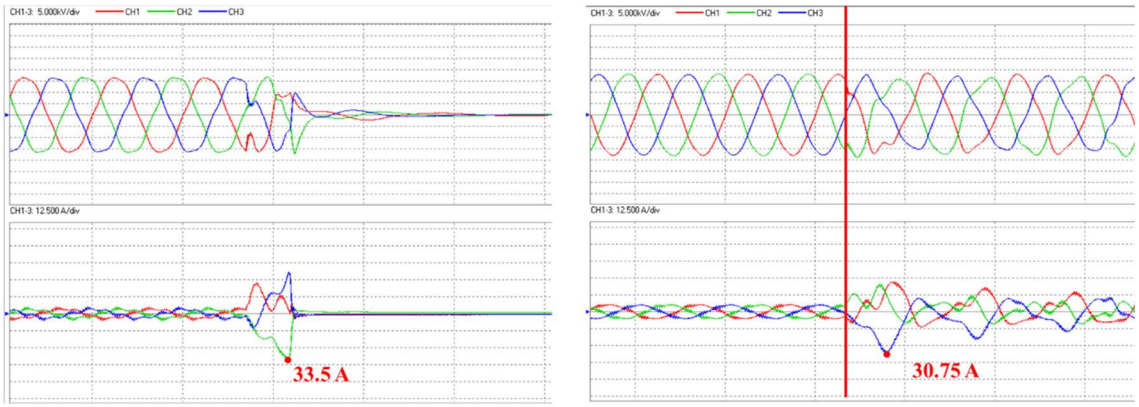

Figure 73. Voltage and current waveforms comparison for cases 2 (left) and 4 (right).

Before comparing these cases, it is interesting to compare the inrush current real reaction to the obtained results from the simulations of section 5. As previously discussed, the inrush phenomenon results in a huge current peak value. In this case, the presented results do not show the total peak current value since the system is disconnected before reaching its maximum current value or the control algorithm limits this value. However, this current increase is depicted in the first four cases. For cases 3 and 4, the relation between the voltage position at each phase and the reached peak current value at each phase, corresponding the maximum current value to the phase which voltage is at its minimum absolute value in the closing instant, can be checked. For instance, for case 3 presented in Figure 73, the voltage at phase 3 (blue line) presents a zero value at the closing instant, and therefore, the maximum value (35 A) also appears at phase 3.

As seen from the two configurations, when the algorithm is not enabled, as the current provided by the battery reaches a certain limit value, the BESS shutdowns, the current falls instantly to zero, the voltage of the island quickly decreases till it reaches a zero value, and therefore, the whole system is de-energized. Thus, the BESS does not support the inclusion of this feeder.

However, when the control algorithm is activated, as the current reaches this limit value, which seems to be around 40 A, the voltage provided by the battery slightly decreases, therefore limiting the current value, supporting the connection of the added feeder. As the current value decreases, the voltage can slowly increase to return to its nominal value. The outcome of the use of this voltage algorithm is the successful connection of the two added feeders, which makes the islanding operation more robust since it allows the connection of new feeders during normal operation without triggering the battery's protection.

The remaining 3 cases also follow the same pattern. For instance, in Figure 74, the peak current time plot for the 7th test is shown. The blue line represents the maximum current value for one of the three phases. Each of the five events shown correspond to the same system configuration. The important thing to highlight from these three last cases is the repetition of the same operation.

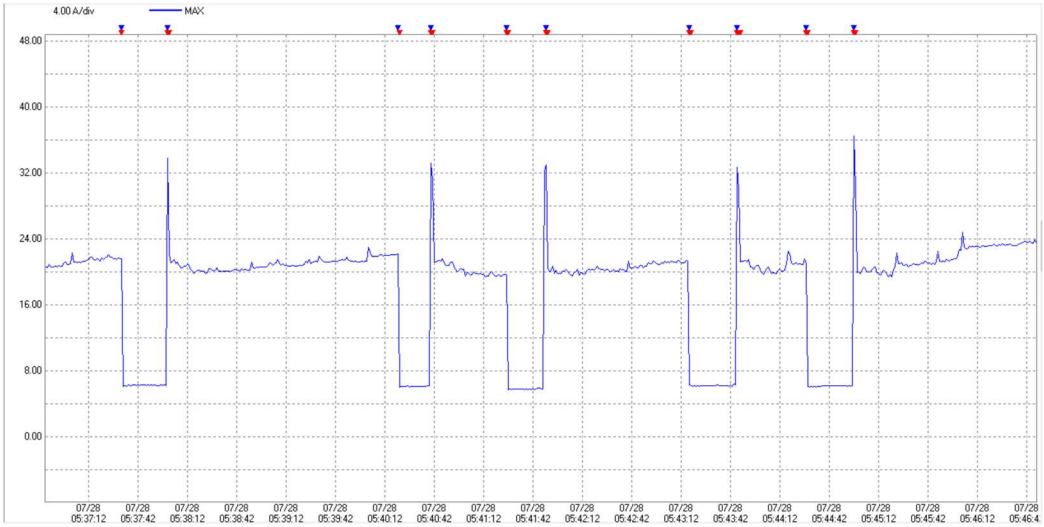

Figure 74. Peak current maximum value time plot for case 7.

However, results presented in Figure 74 are not sufficient to determine the similarity between repetitions, since it only shows the current values of one phase. For each of the five repetitions, the maximum current value has been measured through the event register that enables a further detailed analysis of the current and voltage waveforms when the event takes place. Table 9 collects the maximum current values for each of the remaining three cases for each of the carried-out repetitions.

		Repetition				
		1	2	3	4	5
Case	5	35	38.5	30	32.5	-
	6	32.5	33.75	35	36.25	-
	7	35	37.5	37.5	37.5	37.5

Table 9. Maximum inrush peak current values in A for each of the repetitions of cases 5, 6 and 7.

As seen from the results presented in Table 9, for all the cases, the reached peak current value is similar and close to 35 A in general. This consecutive reached value is a consequence of the activation of the voltage control algorithm, which allows the connection of larger feeders to the systems without triggering the battery protections. However, for the purpose of this thesis,

applying this control to the system leads to a loss of information, since the current is limited and therefore presents very similar values for all the cases.

The objective of these three last tests was to verify if the relation between the voltage status at the circuit breaker opening and closing instants is related to the current peak values at the energization of a feeder through the obtained initial flux cases from the simulations carried out in section 5.2. However, and since the current peak values from the results are modified according to the voltage variation, this relation cannot be verified through the carried out experimental tests.

Two main conclusions are drawn from this section. First, the inrush current behavior analyzed through the theory and the simulations had been verified, since, although the quantitative values could not be compared due to the test limitations, the same qualitative pattern can be observed from the tests results. Secondly, the use of a control that enables the variation of the battery output voltage allows the connection of larger feeders since it limits the current flowing from the BESS, therefore not letting the protections to trigger. In addition, these field test had been a very useful and enriching experience that have served to get closer to the reality behind the inrush issue.

7. ANALYSIS OF POSSIBLE SOLUTIONS

In this section, taking advantage of all the knowledge obtain through the development of the whole thesis, three possible solutions are going to be discussed, including the circuit breaker closing based on an initial flux register, the use of three single-phase circuit breakers to close them independently, and, finally, the voltage variation at the connection instant.

7.1. Flux-Register Based Circuit Breaker Closing

This first possible solution is really a conclusion drawn from section 5.2.3, where it has been proved that the inrush current value is highly dependent of a combination of the initial flux condition and the circuit breaker closing instant.

As long as the residual flux at each phase is known before closing the circuit breaker, the effects of the inrush currents can be minimized, even removed when energizing the transformers. As seen in Table 7 from section 5.2.3, a direct relation between the remaining residual flux and the voltage status at the opening of the circuit breaker can be stated. Therefore, this first solution consists in the installation of a device capable of precisely registering the voltage signal at the opening and closing instants of the circuit breaker.

A device that can be used for this purpose is the phasor measurement unit, also known by its acronym, PMU. A PMU, also known as synchrophasor is a fundamental component in the improvement of the monitoring of the power system.

A PMU generates a three-phase phasor by sampling the measured voltage and current measurements acquired using the respective transformers. The generated voltage and current phasors are a representation of the magnitude and phase angles of the sampled waveform in the complex plane.

The term “synchrophasor” describes a phasor that has been measured and generated an any moment in addition to a time stamp. The accurate generation of this time stamp requires an arranged synchronization cycle to provide each measurement with an exact timing tag. These timing tags are generated using GPS technologies and transmitted over wide communication networks to synchronize the phasor information of the whole power system. Timing requirements are described by IEEE 37.118 standard, which also defines recommendations for PMU measurements through the performance evaluation quantities (such as total vector, frequency and RoCoF errors). The main difference that can be highlighted from the traditional measurements based on a SCADA system comes from the sampling rate. While the SCADA can provide 4 measurements per cycle, a PMU reaches up to 60 measurements per cycle, which facilitates the study of dynamic occurrences in the network [24].

In addition, and in reference to [24], several commercial PMUs are integrated with detection and protection devices such as protection relays, circuit breakers and timers.

Using a PMU, the most efficient connection and energization of the island could be performed by first registering the voltage status when the islanded is disconnected and therefore de-energized, and secondly, and thanks to the use of a PMU integrated circuit breaker, by closing the breaker at the instant that minimizes the inrush effects. Furthermore, this process could be automatized to optimize the circuit breaker closing depending on the registered initial flux case.

However, it is also important to mention that the relation between the voltage and the residual flux values in which all this solution is based, has just been proved in a simulation. Real experimental tests and measurements should be carried out to validate this relation.

In addition, the simulation that had been carried out present certain limitations. Assuming the simulations match perfectly with the real response of the system, the relation between the residual flux and the voltage signal is proven for 12 points, which, although being sufficient for obtaining the 6 different initial flux cases, does not precisely define the boundary between cases. Thereby, it is worth analyzing what would be the impact of a mistaken classification of the initial flux case.

If this classification error would occur, the flux condition would be displaced by just one case due to the abovementioned boundary problem. For instance, let consider that the system is in "case 1" ($\varphi_A=-\varphi_R$, $\varphi_B=0$, $\varphi_C=+\varphi_R$) while really being in "case 2" ($\varphi_A=0$, $\varphi_B=-\varphi_R$, $\varphi_C=+\varphi_R$) before energizing the feeder. While being in the case 1 situation, the best-case scenario would result from energizing the feeder at the 30º step presented in Table 7 from section 5.2.3. However, and since the initial situation would really be case 2, the inrush current would go from the expected almost zero value, to a current value around 90 A. Nevertheless, and considering this error, the inrush current value would be reduced in approximately a 60% from the worst-case scenario (from an approximate value of 220 A to around 90 A).

In conclusion, this could be a very effective method to reduce the inrush current value, or even to remove it if the voltage and flux relation is improved to obtain more precise boundaries between each of the residual flux initial cases.

7.2. Three Single-Phase Circuit Breakers

As reviewed in section 4.1, the best-case scenario for the energization of a transformer takes place when the transformer is connected to the grid while the voltage at its primary side presents its absolute maximum value. Thus, the flux will be minimum, and therefore, the inrush current will also be reduced.

The main problem when considering a three-phase transformer resides in the nature of a balanced three-phase system, where the voltage at each phase is delayed 120º with respect to each other. This fact makes impossible the connection of a three-phase transformer under this best-case scenario condition with a three-phase circuit breaker.

However, in this section, the possibility of changing the three-phase circuit breaker for three single-phase circuit breakers is going to be analyzed. The main objective of this change is to determine if the independent closure of each phase when its respective voltage value is at its absolute maximum value reduces the overall inrush current value for the 6 different initial flux cases.

To prove the effect of using three single-phase circuit breakers, a simple simulation is going to be carried out. As presented in Figure 75, it includes an ideal voltage source, three single-phase circuit breakers, and a 50 kV transformer. Additionally, the flux and the primary side voltage of the transformer had been measured as well as the phase currents flowing into the transformer.

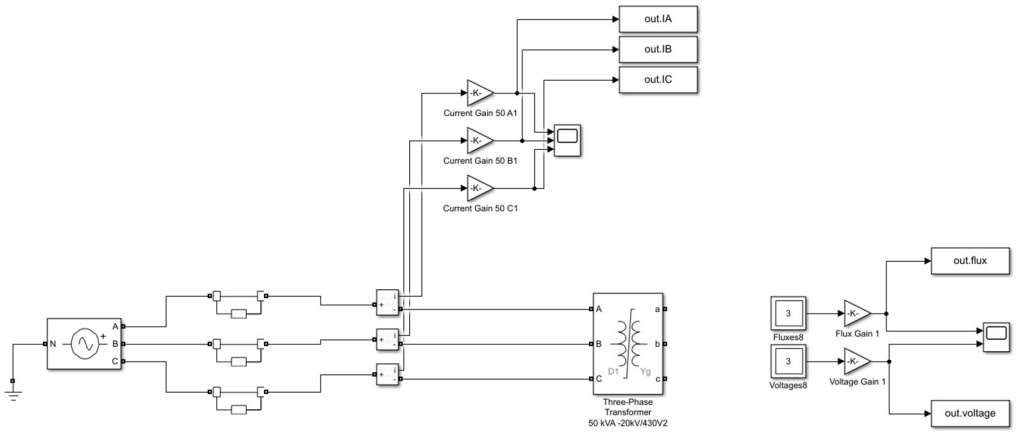

Figure 75. Simulink schema for the three single-phase circuit breaker simulation.

The important point of this solution is that it would not require a previous knowledge of the initial flux condition of the feeder. Instead, the three single-phase circuit breakers would be always closed at the instant, when the corresponding voltage at each phase reaches its highest absolute value. Therefore, the simulation is carried out to analyze the effects of this change by comparing it to the base case that was presented in section 5.2.3, which is based on a three-phase circuit breaker.

As seen in section 5.2.3, there are six possible initial cases depending on how the residual fluxes on each phase remain after the circuit breaker opening. Thus, the interesting point to study is the maximum inrush current value variation through the six different cases while maintaining the same closing configuration for both the three-phase circuit breaker and the three-phase circuit breaker.

Thus, in Table 10 the results from the abovementioned simulations are presented, where, as for previous presented results, the dark red color stands for the highest inrush current value while the dark green color represents the lowest inrush current value. Each of the cases are further detailed in Table 11, where the value of the initial flux is represented by a positive (+), negative (-) or zero (0) residual flux value. From these results, one main conclusion can be drawn; the worst-case scenario inrush current value for the implementation of three single-phase circuit breakers is reduced by an approximate 50% in comparison with the base case.

	Case 1	Case 2	Case 3	Case 4	Case 5	Case 6
Imax Three-Phase Circuit Breaker (pu)	0.016	6.172	10.934	15.253	10.996	5.864
Imax Single-Phase Circuit Breaker (pu)	0.015	3.905	6.895	7.61	5.737	4.975
Reduction (%)	6.25%	36.73%	36.94%	50.11%	47.83%	15.16%

Table 10. Inrush current maximum value for each of the initial flux cases for the single three-phase and three single-phase circuit breakers simulations.

	Case 1	Case 2	Case 3	Case 4	Case 5	Case 6
Flux A	0	+	+	0	-	-
Flux B	-	-	0	+	+	0
Flux C	+	0	-	-	0	+

Table 11. Residual flux condition of each phase for each of the initial cases.

To better understand why this variation in the inrush current takes place, it is helpful to take a further look into the flux and voltage responses as well as its effect on the inrush current with the use of three single-phase circuit breakers and to compare it to the use of a single three-phase circuit breaker. These two cases had been simulated for analogous cases, therefore depicting two comparable simulations.

In Figure 76 and Figure 77 the voltage at the primary side and the flux at the transformer, and the inrush currents generated by the energization of the transformer are shown, respectively, for the base case (a single three-phase circuit breaker).

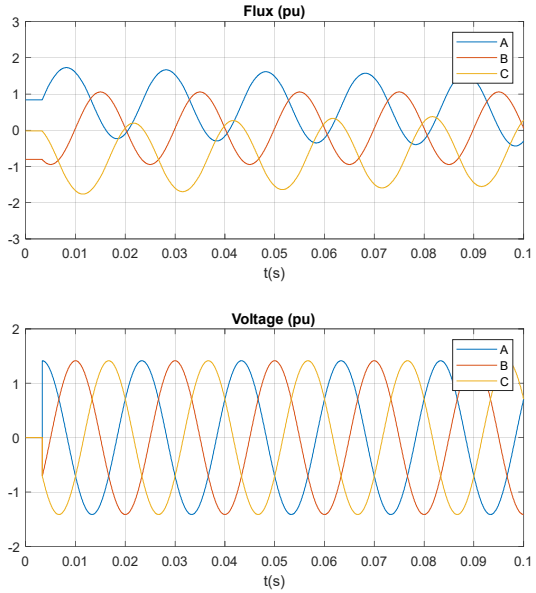

Figure 76. Flux and primary side voltage at the transformer for the single three-phase circuit breaker simulation.

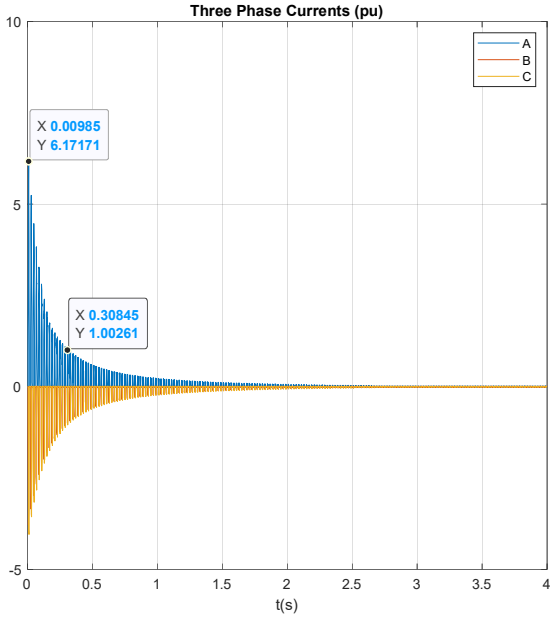

Figure 77. Inrush current value for the single three-phase circuit breaker simulation.

For the base case, as previously seen in other sections, the voltage at the three phases appears at the same time since there is just one circuit breaker activation for the three phases. The flux values in this case reach maximum values per phase of approximately 1.75, 1.7 and 1 pu, resulting in a maximum peak current value of 6.17 pu. Additionally, the time it takes for the current to reach its nominal value is around 0.3 seconds.

In Figure 78 and Figure 79 the voltage at the primary side and the flux at the transformer, and the inrush currents generated by the energization of the transformer are shown, respectively, for the new proposed solution case (three single-phase circuit breaker).

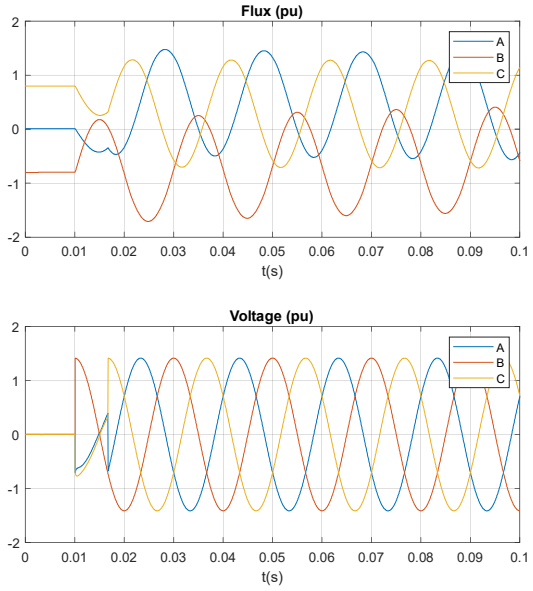

Figure 78. Flux and primary side voltage at the transformer for the three single-phase circuit breakers simulation.

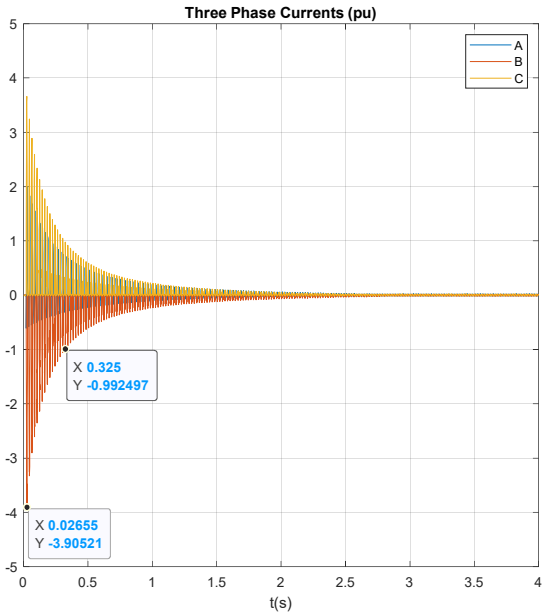

Figure 79. Inrush current values for the three single-phase circuit breakers simulation.

Looking at the presented results for the proposed solution case, the main difference appears within the voltage response. As has been mentioned, the connection of the transformer takes place in three steps, each one coinciding with one circuit breaker closing at each phase. With the first activation (t = 0.0033 s), no voltage signal appears in the simulation since there is not a return path for the current. When the second phase is connected through the circuit breaker activation (t = 0.01 s), and, since Figure 78 shows the line voltage across the primary windings of the transformer, the signal that appears at this second step consist in one of the line voltages at its nominal value, while the other two transformer line voltages presenting a value that matches with the phase nominal value, therefore being these two different voltage values related by the square root of 3. Finally, in the third step, the last circuit breaker is closed (t = 0.0167 s), and thus, the system is finally working as a three-phase system.

The main outcome of the use of three single-phase circuit breakers instead of a single three-phase circuit breaker consist in the voltage reduction at the second step of the process (when two of the phases are connected), where the voltage at two of the three primary windings presents a value that is reduced by a factor of √3. The flux in this second case reaches maximum values per phase of approximately 1.7, 1.4 and 1.25 pu, which, in comparison with the base case, represents an overall flux reduction, that leads to a current maximum peak inrush current decrease to a value of 3.91 pu, which supposes a 37% reduction in the inrush current compared to the base case. Additionally, the extinguishing time is still around 0.35 seconds, therefore, not presenting any significant changes timewise.

7.3. Voltage Variation

In this section, the last proposed solution is going to be analyzed. This last proposal is focused on the voltage variation of the battery energy storage system (BESS), in this case represented by the ideal programmable voltage source found at the Simulink Specialize Power System library.

The ideal way to carry out the voltage variation when energizing the transformer consist in implementing a voltage ramp to increase the voltage value from zero to the nominal value. This implementation is a great option when the first connection is made, either one or more feeders simultaneously. However, while the system is in operation, the voltage cannot fall to zero, because if so, the protections would trigger and the whole system would be disconnected.

Following the Spanish network code [25], the undervoltage limitation is set to a decrease of 15% in the voltage amplitude maintained for, at most, 1.5 seconds. Therefore, these limitations are going to characterize the voltage variation that can be implemented without triggering protections while the system is in operation.

7.3.1. Simple Transformer Case

As for the previous section, and with the purpose of easing the simulation process, for this section, the analyzed solution is going to be carried out on a simplified model. However, this simulation enables the analysis of the effect of the voltage variation in the inrush current value. The model consists basically of an ideal programmable voltage source, a three-phase circuit breaker and the three-phase saturable transformer. Additionally, several Simulink blocks had been implemented to obtain the required measurements. The model used for these simulations is presented in Figure 80.

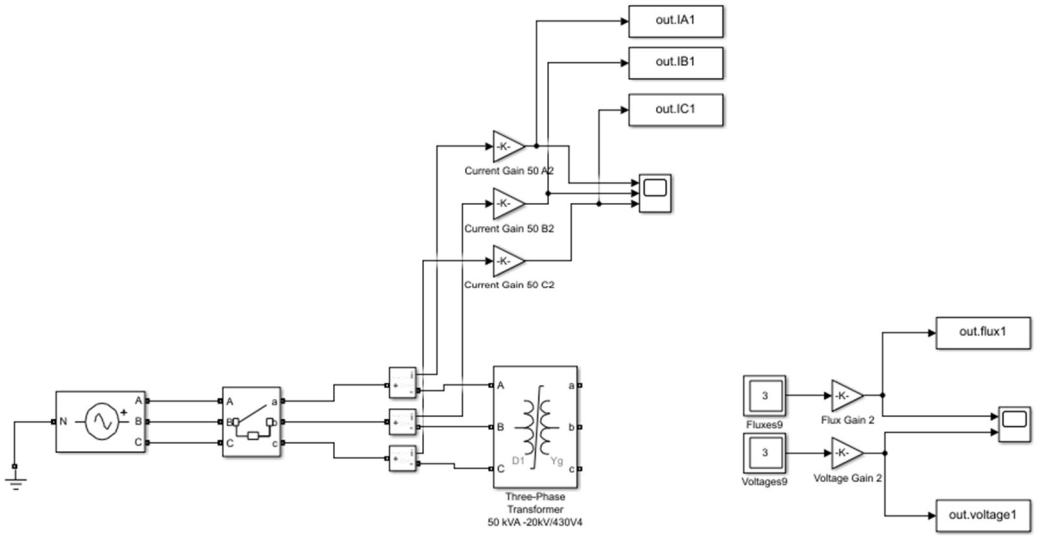

Figure 80. Simulink schema for the voltage time variation simulation.

Two different cases are going to be analyzed under the same simulation model. First, a voltage ramp starting at a zero-voltage value and increasing to the nominal value in 1.5 seconds is going to be implemented to analyze the best-case scenario to energize a transformer. Secondly, an additional voltage ramp is going to be implemented, but, in this case, starting from a voltage value equal to 0.85 pu. This starting point (0.85 pu) will be maintained for 1 second to then be increased in 0.5 seconds up to the nominal value (1 pu) within a ramp shape.

For this voltage variation implementation, the programmable part of the voltage ideal source is going to be used. This block enables de possibility of introducing an amplitude, phase, or frequency voltage time-based variation in several ways, including a ramp, step, modulation, and a table of time-amplitude pairs. Surprisingly, the ramp option is not a good fit for this case, since it only allows to introduce one increasing or decreasing ramp. However, for this simulation the initial status, where the system operates at its nominal values needs to be reached, and therefore a later decrease of the voltage is needed before the implementation of the increasing voltage ramp to be studied. Thus, the selected option has been the time-amplitude pairs table, which enables to stablish a different voltage through time without the need to be just increasing or decreasing. However, the main drawback of this option is that the ramp implementation is carried out through small steps introduced by hand, so the resulting ramp is not as smooth as the ramp option included in the voltage ideal source, which is going to lead to some flux and current peaks, that could easily be removed by introducing a higher number of time-amplitude pairs to the table. For the results presented in this section, the points had been indicated for a 0.05 second step, which is sufficient to analyze the effects of the voltage amplitude variation.

7.3.1.1. Base Case

First, it is important to include the results of the energization of this transformer without any voltage variation as the base case to compare it to the results obtained from the different voltage variations implemented. For this base case, as well as for the other two additional simulations, the circuit breaker has been programmed to emulate the worst-case scenario. Figure 81 shows the voltage at the primary side and the flux at the transformer at the energization instant. The voltage

value is set to its nominal value on an instantaneous step. The flux in each phase reaches a maximum absolute value of 2.354, 2.351 and 1 pu respectively.

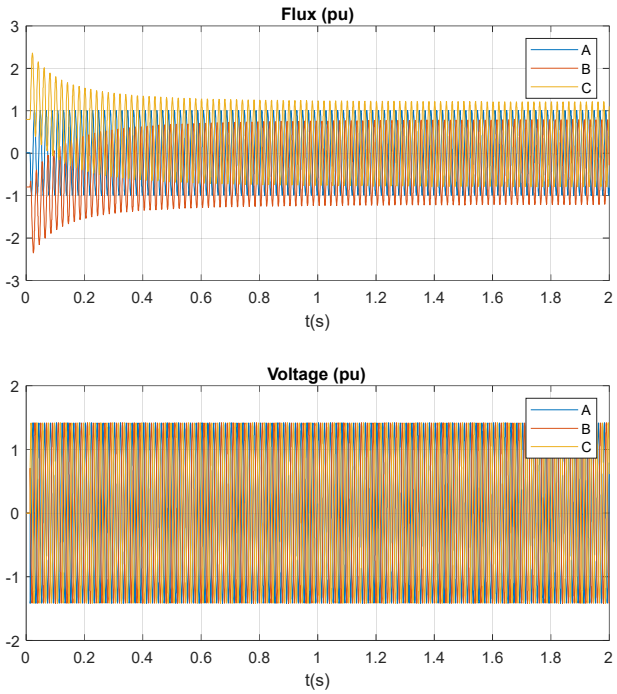

Figure 81. Flux and voltage at the primary side of the transformer for the base case simulation.

Figure 82 shows the current flowing to the transformer in the energization instant. The maximum inrush current value for the base case reaches a maximum value of 14.87 pu.

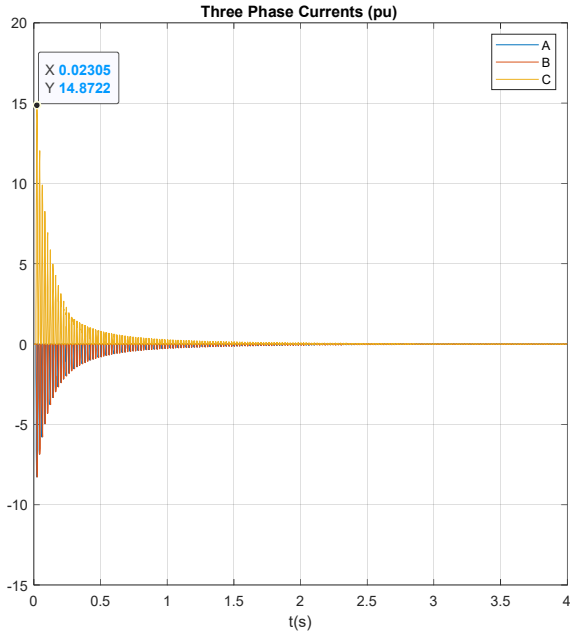

Figure 82. Inrush current values at each phase for the base case simulation.

7.3.1.2. Zero-to-Nominal Voltage Ramp

Now that the base case has been stated, it is time to analyze the effects of the voltage amplitude variation over this case. As abovementioned, two cases are going to be emulated, a ramp increasing from a zero-voltage value up to the nominal value of the system, in addition to a ramp increasing from a voltage value of 0.85 pu up to the nominal voltage value of the system.

For the voltage ramp of the first case, that goes from zero to nominal value in 1.5 seconds. The slope is composed by 30 steps, each one of them supposing an increase of 0.01333 pu. This slow increase in the voltage has a direct impact on the flux at the transformer, that reaches a maximum value of 1.35 pu. These results are shown in Figure 83.

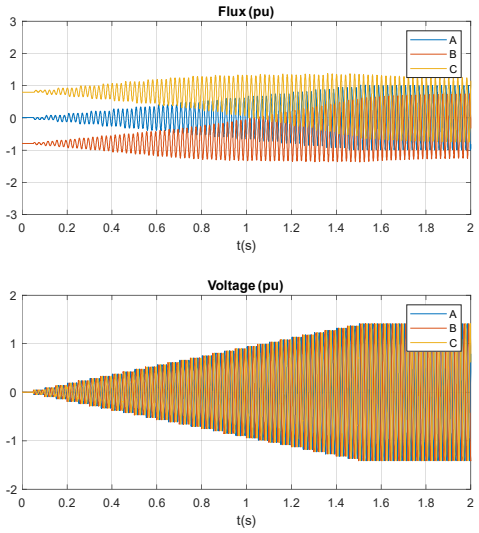

Figure 83. Flux and line voltage at the primary side of the transformer for the voltage time variation starting from a zero-value simulation case.

The impact of this voltage ramp increase in the inrush current is shown in Figure 84. The maximum inrush current reaches a peak value of almost 1.3 pu, which represents a current reduction of a 91% in comparison with the base case.

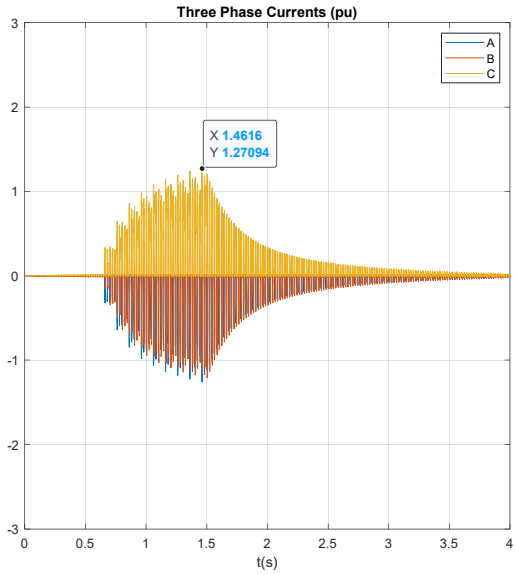

Figure 84. Inrush current values at each phase for the voltage time variation starting from a zero-value simulation case.

7.3.1.3. Voltage Ramp Under Normal Operation

For the second case, the voltage time variation is programmed in two differentiated parts, which in total takes up to 1.5 seconds. For the first second, the voltage value is set to 0.85 pu, which is the minimum value supported by the protections. This part is intended to keep the voltage value at its minimum for as long as possible, so that it gets reflected on the flux value, and ultimately on the inrush current value. For the remaining 0.5 seconds, a voltage increasing ramp has been programmed to reach the nominal value at the end of it. This ramp is composed by 10 voltage steps, which implies an increase of 0.015 pu per step. In this second case, and as can be observed in Figure 85, the flux reduction is lower than for the previous case, reaching a peak flux value of 2.15 pu.

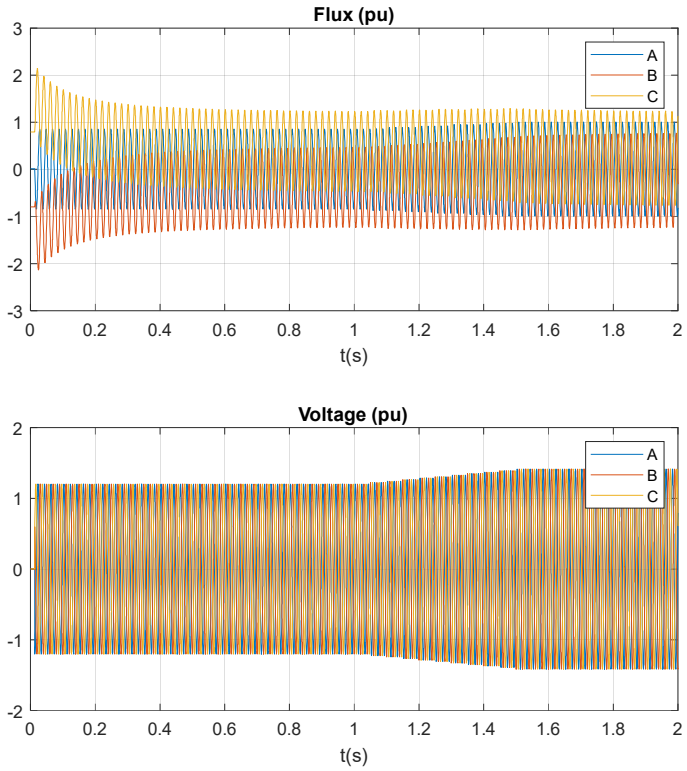

Figure 85. Flux and line voltage at the primary side of the transformer for the voltage time variation starting from 0.85 pu voltage value simulation case.

In comparison with the previous ramp implementation, there is a less noticeable effect on the inrush current value. In this case, the slight flux reduction from the base case (from 2.35 to 2.15 pu), produces a much less significant change in the inrush current value. Figure 86 shows the three-phase current for this second case. The inrush current reaches a peak value of almost 12 pu, which represents a total reduction of a 20% of the base case inrush current.

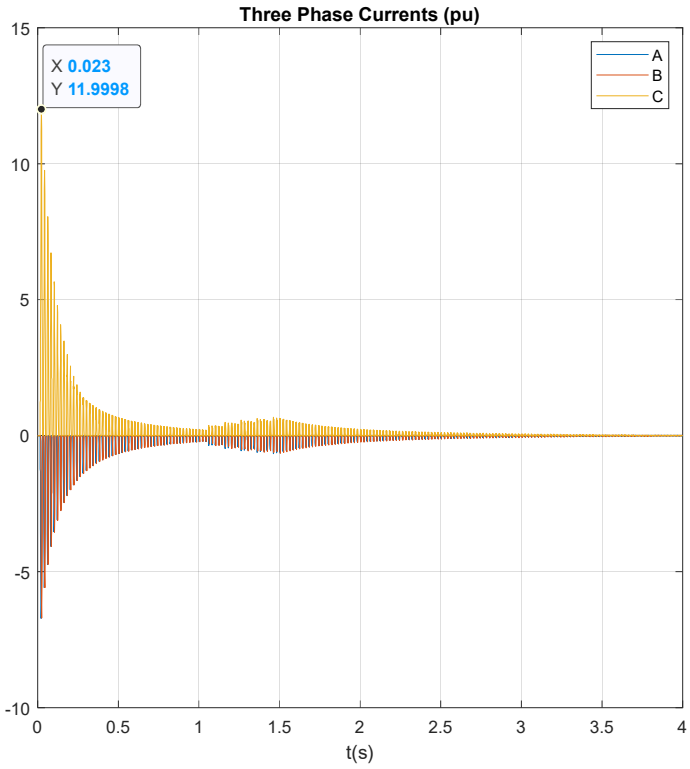

Figure 86. Inrush current values at each phase for the voltage time variation starting from 0.85 pu voltage value simulation case.

The results analyzed show that the optimal way to connect a transformer system would be through the implementation of a voltage ramp starting from a voltage zero value and reaching its nominal value. For this situation, the current reaches a value that remains around the nominal current value (1 pu), representing a 90% reduction from the base case. Therefore, this approach would be optimal to overcome the inrush current issue, by removing the high current peaks that, for this case would reach a value of 15 pu.

On the other hand, the second simulated case shows that, for an operating system under nominal conditions, where the voltage must not decrease under a certain value (a 15% for the analyzed case), the voltage variation through the connection process does not lead to such a significant reduction of the inrush current value, presenting an overall 20% reduction for the energization of a single transformer.

Based on these conclusions, the optimal way to energize a whole island system composed by several feeders would be all at once, since the zero to nominal value ramp could be implemented.

7.3.2. Real Feeder Case

If some other feeder had to be connected, the inrush current reduction effects are not as straight forward as for this first case. However, results are based on a single transformer simulation case, and the effects of applying the same voltage variation to a whole feeder could differ from the results obtained in this section. For this purpose, the voltage variation through time during the energization of a feeder has been implemented to the real feeder emulated in section 5.2.3.

Figure 87 shows the results obtained for the base case, which does not include any voltage variation. The maximum inrush current peak reaches a value of 221 A.

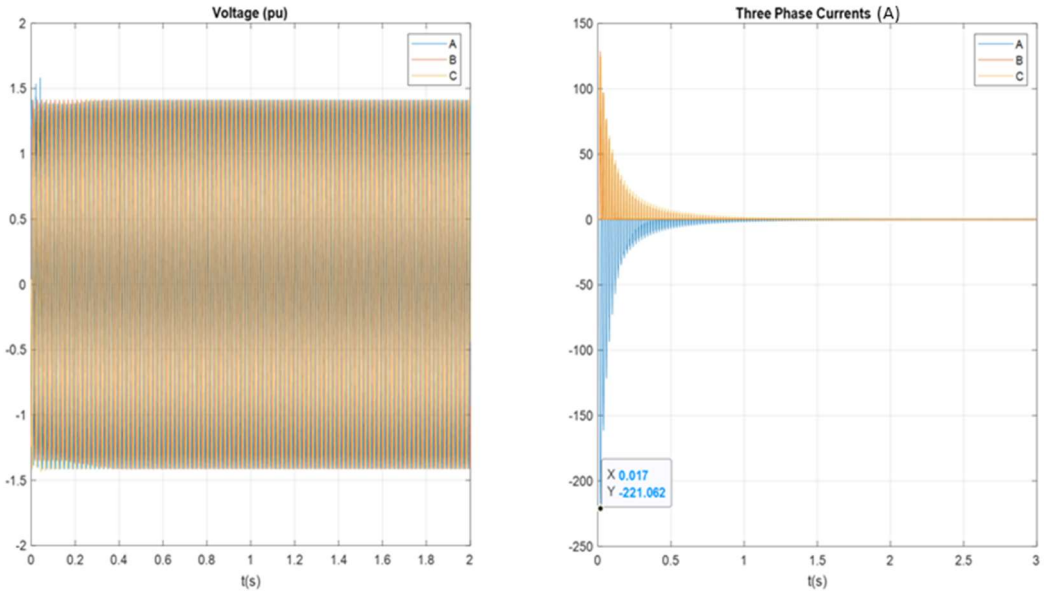

Figure 87. Line voltage and three phase currents at the top of the feeder for the base case simulation.

Figure 88 shows the results of the simulation including the voltage variation, as can be seen at the left plot. The effect of this voltage variation is a reduction of the inrush current reaching a value of almost 180 A, which represents an approximate 20% reduction of the base case.

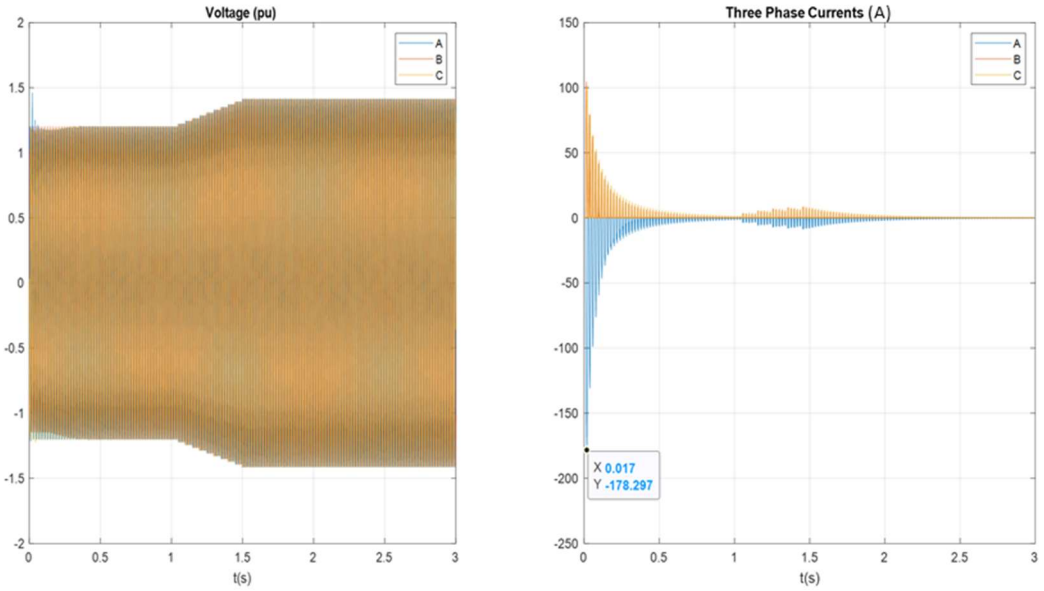

Figure 88. Line voltage and three-phase currents at the top of the feeder for the voltage time variation case simulation.

This last simulation confirms that the same conclusions can be drowned from the results of one transformer and extrapolated to a whole feeder.

Now that the two possible cases had been analyzed, it has been made clear that the most interesting solution is the single voltage ramp increasing from 0 to 1 pu. Therefore, it is also important to study how this voltage variation could be implemented.

In the next part of this section a very simple implementation is going to be analyzed by looking at the highest layer of the introduced changes.

At this point, it is important to remember that the inverter governing the BESS features a voltage source control, therefore stating a voltage reference that the inverter control will try to reach.

Since the voltage is the magnitude that is being controlled, it makes sense to implement this ramp in the voltage loop of the control. At the highest level, the main difference with the scheme presented in section 4.2.2 for a voltage source-controlled inverter, would be the inclusion of an additional element to the voltage reference generation to introduce the voltage variation. This element must be able to differentiate when the system is being energized the first time from the normal operation of the system, thus stablishing two cases: normal operation and energizing operation. Under normal operation, the voltage must be equal to the nominal reference value. However, under the energizing procedure, this element must be able to modify the reference voltage value in a ramp shape. Consequently, the input and output for this element are going to be the reference nominal voltage value and the modified voltage reference value (under certain circumstances), respectively.

As seen in section 4.2.1, with the implementation of the dq-frame to the inverter control, the voltage at the q-axis is set to zero, and therefore only the voltage at the d-axis exists. Thus, the control is equal to imposing a voltage ramp on the d-axis component of the voltage reference.

Therefore, the schematic for the reference voltage value obtention remains as depicted in Figure 89.

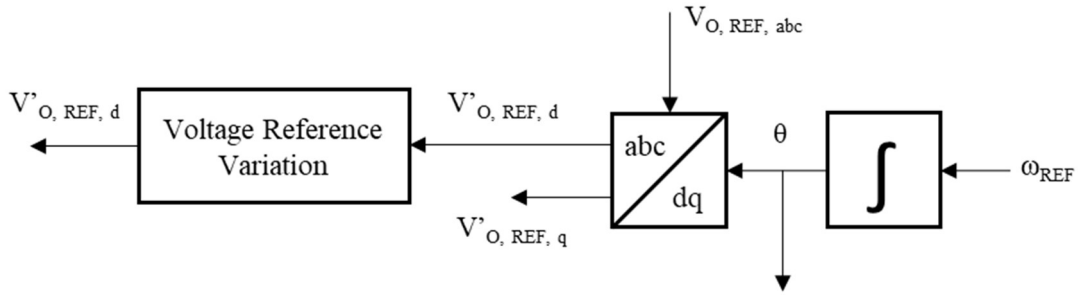

Figure 89. Schematic for the reference voltage value obtention of a voltage source-controlled grid-former inverter.

In this "voltage reference variation" element, the voltage variation must be programmed by defining the operation under the two abovementioned statuses.

If the system is running under normal operation, the voltage reference value must be equal to the reference nominal value by (76).

$$|V'_{o,ref,d}| = |V_{o,ref,d}| \tag{76}$$

However, if the system is running under the energizing operation mode, the voltage reference value must follow the previously described voltage ramp as seen in (77), where t_{slope} represents

the time in seconds for the voltage ramp to reach its nominal value and with the voltage being represented in pu.

$$V'_{o,ref,d} = \begin{cases} \frac{1}{t_{slope}} t, & t \leq t_{slope} \\ |V_{o,ref,d}|, & t > t_{slope} \end{cases} \quad (77)$$

This implementation should be further studied, analyzed, and implemented, but, since the development of this kind of solutions is out of the scope of this project, this brief analysis is enough to get an idea of the type of implementation to be done in the inverter's control.

8. CONCLUSIONS

In this last section, the conclusions, including the methodology, results and future studies are included.

8.1. Methodology

To make clear the followed methodology, it is important to review the thesis development. In the first place, the main objectives of this project were discussed and stablished with both the industrial and academic tutor's help. The main objective of this thesis is the construction of a detailed simulation model capable of predicting the inrush current value that appears when connecting and energizing a feeder, during islanding BESS based operation. With this objective in mind, the first step has been to perform an in-depth study of the physics behind the inrush current phenomenon, with a special focus on the searching of plausible solutions for the Simulink model development. The second step in this process has been to work on a first more basic simulation model consisting only of a single three-phase transformer, with the objective of sizing the transformers that are used for later simulations and to verify the coherence between the simulation operation and the theory reviewed. Once the individual operation of each of the modelled transformers had been checked, it is time to move to the third step of this thesis, which basically consists in building the model of a whole feeder based on a real feeder from the Iberdrola island network at Caravaca de la Cruz, with the objective of analyzing the dynamic response that the connection of this feeder supposes. In this section of the thesis special focus has been set in the initial conditions that lead to the different reached inrush current values. This part of the project is followed by the experimental tests that had been carried out in the Iberdrola BESS facility at Caravaca de la Cruz, which main objective has been to verify the operation of a BESS based island and the response to the connection and energization of a feeder. Additionally, these tests also aim to check the relation between the reached maximum inrush current value and the voltage value at the connection instant. Finally, and supported with all the knowledge acquired through the development of this thesis and the built simulations, three possible solutions have been proposed and analyzed, which have the potential to end with the problem that supposes the inrush current when connecting additional feeders to a BESS based island.

It can be concluded that the used methodology, based in the simulation model construction based on the software Simulink by Matlab supposes a very favorable approach to the development of this project. As it has been proved through previous sections of this thesis, the inrush current value is highly dependent both on the structure of the feeder that is going to be connected and the network status at the opening and closing of the circuit breaker that leads to the connection of the feeder. Therefore, the development of this simulation in a software like Simulink, that enables the construction of different feeders from the use of certain previously built common blocks, as well as easily visualize and analyze the effects presented on the results if the initial status of the network is modified, leads to conclude that the right methodology has been selected.

Furthermore, the nature of the Simulink software, which is based on the block simulation, has also permitted to support the presented possible ideas with results obtained from specific simulations that have sustained the proposed solutions.

8.2. Results

From the results obtained in the different sections of this thesis, the following conclusions can be drawn.

- First, through the combination of the offered tools both in Matlab and Simulink, the simulation of a transformer capable of reproducing the dynamic response that the energization of a feeder supposes has been achieved. Unlike in most of the network applications, where the focus of the transformer operation is set in the steady state operation, this project is focused on the dynamic response of the feeder energization, since the inrush current is a rapidly extinguished phenomenon. The inclusion of the effect of the magnetizing characteristics of the transformer, which includes both the hysteresis and saturation curves, had been successfully achieved, which are the main causes for the inrush current apparition.
- Once the simulations had been satisfactorily build, an analysis of the transformers response when energized has been carried out. With this analysis, it can be verified that the transformers operation truly reproduces the inrush current behavior that has been reviewed in the investigation section of this project. Thus, it can be concluded that the simulations are adapted to the theory analyzed.
- Thirdly, the successful emulation of a real feeder has been achieved, obtaining an accurate estimation of the reached inrush current value that is produced when connecting and therefore energizing a set of transformers connected by the distribution network. Besides, and as has been commented in the previous section, Simulink enables the personalization of the feeder to be connected to the BESS, therefore, a precise inrush current estimation could be done for feeders with different configurations if needed.
- As the results obtained from section 5.2.3 show, the inrush current value is highly dependent of the feeder initial status, which, at the same time depends upon two main parameters: the voltage waveform status at the circuit breaker opening, where a residual flux case is stablished, and the voltage waveform status at the circuit breaker closing instant, which stablishes the reached peak current value. In this thesis, the relation between the initial residual flux case and the voltage status at the circuit breaker opening has been obtained. This relation has led to one of the most surprising conclusions of this thesis. The simulation results show that it is possible to determine the initial flux status of the transformers of a feeder by keeping a voltage status register. Then, and knowing this initial status, it would be possible to trigger the circuit breaker in the optimum instant that could lead to the removal of the inrush current issue.
- Another of the most important conclusions that can be drawn from this thesis development is the strong relation between the inrush current value and the voltage status at the connection instant, which has been proved both by the developed simulations and experimental field tests carried out. On the one hand, simulations have shown that the voltage drop that take place due to the connection of the transformers to the distribution network, lead to a flux reduction that ultimately leads to a reduction in the inrush current value. On the other hand, from the experimental tests at Caravaca de la Cruz, it has been checked the potential use of a voltage variation-based algorithm.
- Finally, and thanks to the experimental test which I have been very lucky to perform at the Iberdrola BESS facility at Caravaca de la Cruz, it can be concluded that the inrush current behavior analyzed through the theory not only matches with the simulations carried out, but also with the results obtained from the field tests.

8.3. Future Studies

The obtained results through the development of this thesis give raise to possible future studies that can be utilized to remove the inrush current effects that hinder the connection of additional feeders when the BESS is operating in islanding mode. But first, the simulation model could take the next step, which consists in the battery simulation by the inclusion of the inverter control into the simulation model of Simulink.

Additionally, at the end of this thesis, in section 7, three possible solutions were proposed and analyzed supported by results obtained from specific built simulations. From these proposals, some conclusions can be drawn.

- The first solution, which is based on the use of PMU integrated circuit breakers, comes from one of the previously discussed conclusions. If the initial feeder status is known, it would be possible to close the circuit breaker in the optimal instant which will reduce or even remove the inrush current effects. For future studies it would be very interesting to verify through more specific and intensive experimental test the obtained relations between the voltage status and the initial residual flux, as well as the inrush current value variation depending on the circuit breaker closing instant that had been obtained through the simulations. This proposal has a lot of potential since it could mean the inrush current phenomenon to be removed.
- The second proposal consists in the utilization of three single-phase circuit breakers instead of a single three-phase circuit breaker. With the independent connection of each phase at its optimum respective instant, and base on the carried-out simulations, a 50% reduction of the inrush current value could be obtained. For future studies, it would be interesting to develop a further analysis of the real behavior of the use of three independent single-phase circuit breakers, since the phases of the transformer are magnetically linked. Furthermore, it would also be interesting to develop an economic viability study for this solution.
- Finally, the third proposal is based in the voltage variation at the feeder energization instant. As previously concluded, there is a high relation between the peak inrush current value and the voltage value. Therefore, this solution leads to a potential current reduction of even a 91%. The operation of a similar solution has been verified through the operation of the algorithm that has been installed in the BESS facility in Caravaca, which is based on a voltage variation to achieve a more robust operation of the island mode, which enables the connection of bigger feeders.

REFERENCES

[1] J. Rocabert, A. Luna, F. Blaabjerg and P. Rodríguez, "Control of Power Converters in AC Microgrids," in IEEE Transactions on Power Electronics, vol. 27, no. 11, pp. 4734-4749, Nov. 2012.

[2] S.V. Kulkarni, S.A. Khaparde. Principles and the Equivalent Circuit in Transformer Engineering. Design, Technology, and Diagnostics (Second Edition, pp. 11-20). CRC Press.

[3] Magnetic Hysteresis Loop including the B-H curve. Electronics Tutorials. URL: https://www.electronics-tutorials.ws/electromagnetism/magnetic-hysteresis.html

[4] S.V. Kulkarni, S.A. Khaparde. Inrush Current in Transformer Engineering. Design, Technology, and Diagnostics (Second Edition, pp. 60-71). CRC Press.

[5] Yacamini, R. and Abu-Nasser, A. The calculation of inrush currents in three-phase transformers, Proceedings IEE, Vol. 133, Pt. B, No. 1, January 1986, pp. 31–40.

[6] Nakra, H. L. and Barton, T. H. Three phase transformer transients, IEEE. PES Winter Meeting, New York, 1974, Paper T-74-243-2.

[7] Westinghouse Electric Corporation. XIV. Exciting and Inrush Currents in Electrical Transmission and Distribution Reference Book (Fourth Edition, pp. 124-130).

[8] Barghamadi, Ebrahim, Senior protection and control engineer at Rayavin Fan (6th of February 2019). Transformer Inrush Current. Linkedin. URL: https://www.linkedin.com/pulse/transformer-inrush-current-ebrahim-barghamadi/

[9] Amir Tokić, Ivo Uglešić, Gorazd Štumberger, "Simulations of Transformer Inrush Current by Using BDF-Based Numerical Methods", Mathematical Problems in Engineering, vol. 2013, Article ID 215647, 10 pages, 2013.

[10] D. Fidel Fernández Bernal (2019). “CAP. 4: El PWM y sus efectos sobre la máquina de inducción”. In Accionamientos eléctricos Universidad Pontificia de Comillas.

[11] Qoria Taoufik, François Gruson, Frédéric Colas, Xavier Kestelyn, Xavier Guillaud, “Current Limiting Algorithms and Transient Stability Analysis of Grid-Forming VSCs”. June 2020.

[12] Iona Serban, Catalin Petrea Ion, “Microgrid control based on a grid-forming inverter operating as virtual synchronous generator with enhanced dynamic response capability”. February 2017.

[13] Amending Regulation (EU) No 548/2014 on implementing Directive 2009/125/EC of the European Parliament and of the Council with regard to small, medium and large power transformers. 25/10/2019. (EU).

[14] Construcciones Eléctricas Jara, "Transformadores de distribución MT/BT – Especificación Técnica", TP-50/24/20 B2-O-PA.

[15] Construcciones Eléctricas Jara, "Transformadores de distribución MT/BT – Especificación Técnica", TC-100/24/20 B2-O-PE.

[16] Construcciones Eléctricas Jara, "Transformadores de distribución MT/BT – Especificación Técnica", TC-250/24/20 B2-O-PE.

[17] Construcciones Eléctricas Jara, "Transformadores de distribución MT/BT – Especificación Técnica", TC-400/24/20 B2-O-PE.

[18] Construcciones Eléctricas Jara, "Transformadores de distribución MT/BT – Especificación Técnica", TC-630/24/20 B2-O-PE.

[19] (2021). "Transmission Line Models". In Control & Protections of Future Networks. University of Strathclyde.

[20] iDE. "Conductores desnudos de aluminio-acero para líneas eléctricas de alta tensión", NI 54.63.01, Nov 2018.

[21] Imedexsa. "Catálogo General. Adaptado al nuevo reglamento RD 223/2008", Serie UNE 207017 Tipo C Atornillada, 2012.

[22] Osprel S.L. "Cálculos Eléctricos GTC", Excel for electric power line calculations, Gonzalo Tejero, 2020.

[23] Rodney Tan (2021). AC Time Overcurrent Relay Block (https://www.mathworks.com/matlabcentral/fileexchange/57521-ac-time-overcurrent-relay-block), MATLAB Central File Exchange. Retrieved July 21, 2021.

[24] Ersan Kabalci, Yasin Kabalci, "Chapter 1 - Introduction to smart grid and internet of energy systems", in Smart Grid to Internet of Energy, pp. 1-62, 2019.

[25] Real Decreto 647/2020, de 7 de julio, por el que se regulan aspectos necesarios para la implementación de los códigos de red de conexión de determinadas instalaciones eléctricas. July 2020. Ministerio para la Transición Ecológica y el Reto Demográfico. Spain.

ANNEX I – SIMULATION ELEMENTS

In this annex, the required elements, and their operation to develop the in-rush current simulations are described. These components include:

- Three-phase transformer.
- Three-phase series RLC branch.
- Three-phase breaker.
- Three-phase voltage source.
- Multimeter.
- Scope.
- Gain.
- Current measurement.
- AC Overcurrent Relay (51).

In Figure 90, all the blocks' representations emulating the abovementioned components in Simulink are presented.

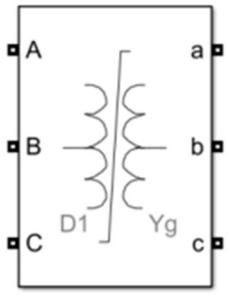	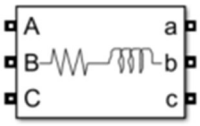	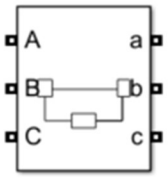
Three-Phase Transformer	Three-Phase RL Series Branch	Three-Phase Breaker
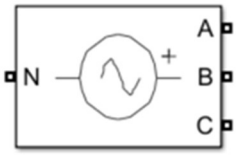	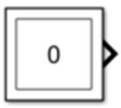	
Three-Phase Voltage Source	Multimeter	Scope
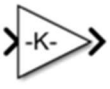		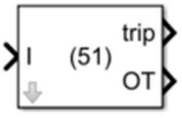
Gain	Current Measurement	AC Overcurrent Relay (51)

Figure 90. Blocks schematic for all the used elements in the Simulink simulation.

Three Phase Transformer

The three-phase transformer is included in the Specialized Power Systems section of the Simscape library from Simulink. The internal operation of this block is based on the previously discussed model shown in Figure 3 at section 4.1. This block enables the possibility to include the hysteresis and saturation curves of the ferromagnetic core material required to emulate both the transient transformer behavior at the energization moment and the steady-state transformer operation.

The hysteresis and saturation curves are added to the model through a Matlab file that is generated thanks to the Powergui tool: "power_hysteresis". This tool enables the user to view and edit the hysteresis characteristic for a saturable transformer by defining:

- The remanent flux (Fr). The point which corresponds to the value that the flux takes when the current goes to zero.
- The coercive current (Ic). The value of the current when the flux is equal to zero. Additionally, the slope at this point is also required (dF/dI).
- And finally, the saturation point (Is, Fs) that indicates the point from which the ferromagnetic core material behaves as an air-cored material.

On the other hand, the saturation curve is also included in this Powergui tool, that it is introduced by the means of two equally-length vectors of current and flux values that define the saturation characteristic. Only the positive side of the saturation curve is required, the negative part is assumed as symmetrical.

Since the objective of this project is to analyze the inrush currents, the focus is set on the saturation characteristic. Therefore, for the hysteresis curve, the default curve shown in Figure 91, which is an extract from the Powergui hysteresis tool, has been used, where it can also be seen the required parameters to specify the characteristic.

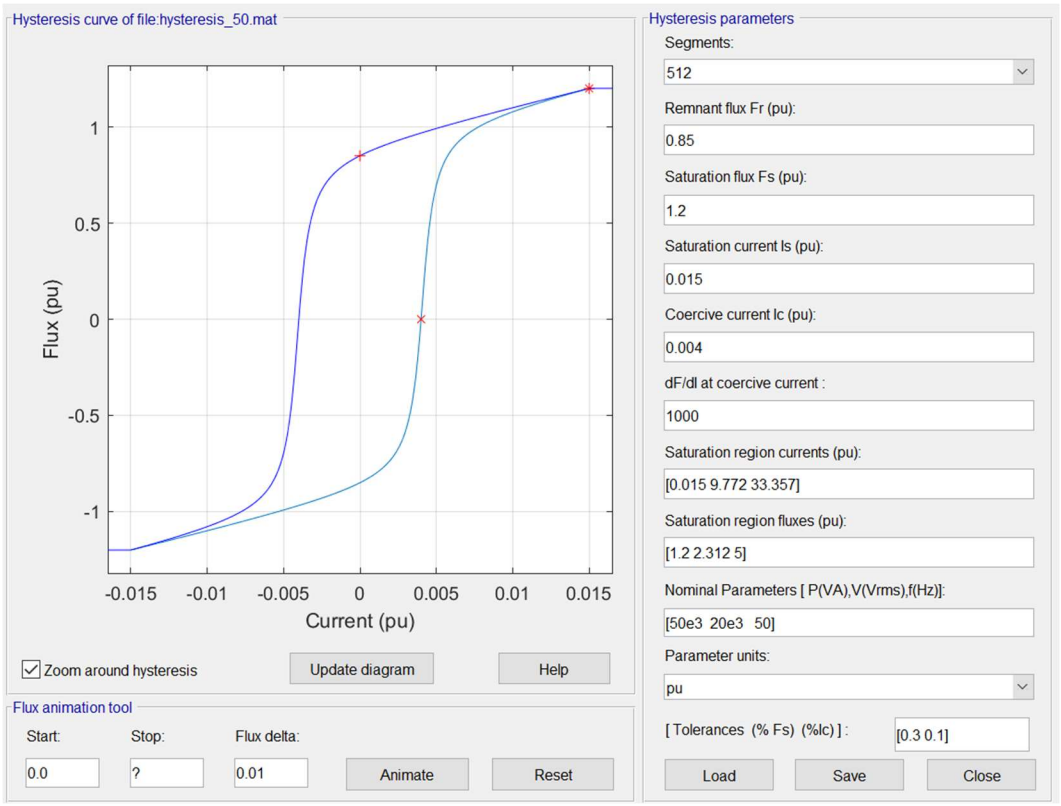

Figure 91. Default hysteresis curve from the Powergui hysteresis curve editing tool.

Before getting into more detail of how the saturation curve has been emulated, it is important to highlight the difference between the B-H and the flux-current curves. On the one hand, the B-H curve shows the relation between the magnetic field in Teslas and the Magnetic Force in Amperes/meters. The B-H curve refers to the material used in the ferromagnetic transformer core material. The core of a power transformer is constructed by adding several ferromagnetic sheets together. There are different B-H curves depending on the quality of the used material and the sheet's width. Nowadays, in the European market, eco-designed transformers, which present low no-load losses, are mandatory under the requirements presented in [13]. These eco-designed transformers are highly dependent on the material quality. The H0 quality is used for the eco-designed transformers, which cores are composed by 0.23 mm width sheets. On the other hand, the flux-current curve depends on the transformer itself since the relation with the B-H curve depends on the magnetic core structure and dimensions. The transformer core dimensions are a very rare information to be included in the transformer's datasheets, and therefore the obtention of the flux-current curves from the B-H curves information is a hard operation.

However, the transformer manufacturers usually include the inrush current value obtained from the electrical tests done to the transformer. Thus, the best approximation to the inrush current is obtained by the information directly found on the transformer datasheet.

To build a complete hysteresis and saturation curve for each of the emulated transformers, the saturation characteristic has been adapted so that the maximum current value obtained in the simulation of each transformer matches inrush current values that appear at the transformer's datasheets [14], [15], [16], [17] and [18].

In addition to the saturation and hysteresis curves, the windings connection, the initial fluxes, the nominal power and frequency, the magnetization resistance and both primary and secondary windings parameters are specified, including the nominal voltage, the series resistance and inductance.

The initial fluxes values are all set to zero to initialize the simulation.

To provide a wide range of possible combinations, five different transformers had been modelled, which characteristics appear in Table 12.

Transformer	**50**	**100**	**250**	**400**	**630**
Windings Connection	Dyn11	Dyn11	Dyn11	Dyn11	Dyn11
Nominal Power (kVA)	50	100	250	400	630
Nominal Frequency (Hz)	50	50	50	50	50
Magnetization Resistance (pu)	185.2	229.9	277.8	310.1	350
V1 Ph-Ph (kV rms)	20	20	20	20	20
R1 (pu)	0.011	0.0088	0.0065	0.0057	0.0052
L1 (pu)	0.0167	0.018	0.0189	0.0192	0.0193
V2 Ph-Ph (V rms)	420	420	420	420	420
R2 (pu)	0.011	0.0088	0.0065	0.0057	0.0052
L2 (pu)	0.0167	0.018	0.0189	0.0192	0.0193
Peak Inrush Current (pu)	15	14	12	12	11

Table 12. Parameters for the five different modelled transformers approved for the medium voltage network usage by Iberdrola.

Finally, the transformer block includes the option to add internal measurements corresponding to the current and voltage at the primary and secondary side, as well as the magnetic flux of the ferromagnetic core.

The transformer parameters are included in the Simulink models through a Matlab file that must be ran each time a simulation is carried out. The Matlab file including all the system and transformer parameters is presented in ANNEX II.

Three-Phase Series RLC Branch

As presented in [19], any high voltage power line can be modelled as a short line whenever its length is below 80 km. Since all the lines that are considered in this analysis are shorter than 80 km, the line can be modelled as a series branch only represented by a resistance and an inductor. Therefore, the use of the Simulink series RLC branch block is suitable for this simulation. This is a simple block that enables the user to simulate any combination of a resistance, an inductance, and a capacitor in series. In this case, the RL branch type has been selected.

The required values for this block are the resistance in ohms and the inductance in Henries.

The selected conductor for these lines has been the LA-56, since it is a suitable conductor for the nominal voltage and maximum power connected to each of the emulated feeders. The maximum power connected to any of the four feeders that are going to be emulated is approximately of 2.5 MVA, which following (78) and for a 20 kV power system, represents a maximum current value of 72.17 Amps.

$$I_{max} = \frac{S_{max}}{\sqrt{3} \cdot U_P} \tag{78}$$

Considering a maximum current of 80 Amps to take account for the effect of the power factor and knowing LA-56 is rated at a maximum current of 202 Amps [20], the usage factor, which is computed as the relation between the maximum current reached in the considered system and the maximum current value supported by the selected conductor, remains at a 40%, being a suitable conductor for these lines. Thus, the parameters of the line used for the RL series branch block are defined by a LA-56 conductor set at a power line tower with the usual dimensions for a nominal voltage of 20 kV [21], resulting in a resistance value of 0.688 Ω/km and an inductance value of 1.378 mH/km computed by [22].

Finally, these parameters are introduced in the block by multiplying the resistance and inductance values with the respective length in km of each of the lines composing each of the four feeders.

Three-Phase Breaker

This Simulink block implements a three-phase circuit breaker, that can be activated both by an external logical signal or by introducing a switching times vector. Some additional parameters are also defined in this block, including the breaker resistance in ohms which corresponds to the resistance when the breaker is closed, the snubber resistance and capacitance, in ohms and farads, respectively. The snubber circuit is an energy-absorbing circuit that is used to suppress the voltage spikes caused by the circuit's inductance when a switch opens. It represents the resistance and capacitance for when the breaker is open.

For this analysis, the three-phase breaker has been simulated as an ideal switch, therefore setting very high values for the snubber components, and a low breaker resistance, specifically, 0.01 Ω.

Three-Phase Voltage Source

This block implements an ideal three-phase zero-impedance voltage source. It presents a common neutral point that is connected directly to the ground. Additionally, this block enables the possibility of amplitude, phase, and frequency variation through time, as well as the inclusion of two harmonics superimposed to the fundamental component.

For this simulation, no time-variation magnitudes or harmonics had been included. The introduced voltage corresponds to the nominal value for the primary side of the simulated transformers, 20 kV and the frequency is set to its nominal value, 50 Hz.

Multimeter

In this simulation, the multimeter block allows to select the transformer internal measurements that the user needs to observe. Three multimeters had been used to look at the three-phase current and voltage at the primary side of the transformer as well as the magnetic flux at the core.

Scope

This block is used to display the generated time-domain signals through the simulation. The scope display features multiple signals and multiple y-axes plots, axis autoscaling, parameters modification and display data after and during simulation. This block is used in combination with the multimeter and with the current measurement.

Gain

The Gain block generates an output by multiplying its input by the specified gain factor. This block includes a multiplication parameter that let the user choose the type of multiplication to be used (element-by-element or matrix multiplication of the input).

For this simulation, the gain block has been used to transform the output signals that are required to be measured from real values to pu, by dividing the gain block's input signal by the respective base values.

The voltage base value is computed as the nominal phase voltage value by (79), however, for the transformer voltage measurement of the primary side, the voltage value coincides with the line value, therefore, in the gain block, the division also includes the square root of three in the base to pu transformation.

$$U_{b1} = U_{N\,ph-n} = \frac{20\ kV}{\sqrt{3}} \tag{79}$$

The flux gain corresponds to the peak flux value, that is computed by (80).

$$\phi_b = \frac{U_{N1\,ph-ph} \cdot \sqrt{2}}{2 \cdot \pi \cdot f_N} \tag{80}$$

Finally, the base primary side current value is computed by dividing the power base value, which corresponds to the nominal power of each of the five transformers, by the voltage base value, that is the same for the five cases, as shown in (81).

$$I_{b1} = \frac{S_b}{U_{b1}} \tag{81}$$

Current Measurement

This block implements an ideal current measurement that works as an amperemeter, which need to be connected in series with the circuit that is going to be measured. This block is used in combination with the scope to visualize the current signal variation through time.

AC Overcurrent Relay (51)

This block, obtained from [23], implements an AC overcurrent relay with the possibility to vary several parameters to fit different protection relays. This block requires the instantaneous three-phase current values as an input and present the tripping signal and the operating time as an output.

This relay provides the option to operate wither with a Definite Minimum Time (DMT) or Inverse Definite Minimum Time (IDMT) trip characteristic. For the IDMT relay, this block offers different trip characteristics, including IEC standard, very, long time, extremely, and ultra-inverse curves, as well as IEEE moderately, very, and extremely inverse curves, which basically changes the shape of the curve, changing the triggering of the protection. The IDMT overcurrent relay present two main settings, that include the Plug Setting (PS) to configure the pickup current by (82), where I_{relay} corresponds to the nominal current value of the protection relay, which usually coincides with the nominal current at the secondary side of the transformer, and the Time Multiplier Setting (TMS), to configure the triggering delay by (83), where α and β are defined by the characteristic type indicated, and I_r is computed as (84), where I_f' corresponds to the fault current at the secondary side of the protection transformer.

$$I_{pickup} = I_{relay} \cdot PS \tag{82}$$

$$t = TMS \cdot \frac{\alpha}{I_r^{\beta} - 1} \tag{83}$$

$$I_r = \frac{I_f'}{I_{pickup}} \tag{84}$$

The PS is expressed in percentage and usually takes a value in between 25 and 200% with 25% steps, while the TMS usually takes a value in between 0 and 1 in 0.05 steps. The PS and the TMS mainly displace the triggering curve horizontally and vertically, respectively, as shown in Figure 92.

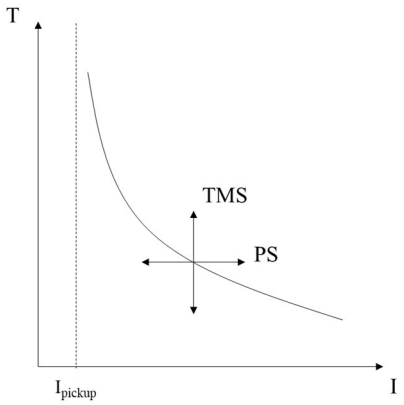

Figure 92. Standard IDMT overcurrent relay curve with the effects of the TMS and PS variation.

Additionally, the nominal current transformer values and the nominal frequency are introduced.

The original code implementing the operation of the relay has been slightly modified to adjust the operation of the relay to a more realistic operation of the protection. First, the inclusion of the absolute current value ensures that the current that is being considered for the relay to trigger is the maximum possible value, since in the original code, just the positive values were being considered. Besides, in the original code, once the pickup current was reached, the relay waited for a definite time of 0.2 seconds to trigger letting the current to theoretically stablish at its maximum peak value. Then, the operating time was computed at that instant with the corresponding current value. This implementation did not consider a possible reduction of the current before the protection could trigger. Thus, the second modification of the code includes the operating time at each moment to compute the triggering signal instead of the fixed waiting value.

The Matlab file where the operation of the IMDT relay is programmed, including all the above-mentioned changes is included in ANNEX III.

ANNEX II – MATLAB INIZIALIZATION FILE

```
clear all;
clc;

%% Common Partameters to all simulation

f = 50;              % Nominal frequency in Hz
V1 = 20e3;           % Nominal Ph-Ph winding 1 RMS voltage
V2 = 420;            % Nominal Ph-Ph winding 2 RMS voltage

Ub1 = V1/sqrt(3);    % Base voltage value for the 20 kV side


%% Data Transformer 50 20

load('hysteresis_50.mat');

Sn_50 = 50e3;            % Nominal apparent power in VA
Rcc_50 = 2.2/100;        % Short-circuit resistance in pu
Xcc_50 = 3.34/100;       % Short-circuit reactance in pu
P0_50 = 90;              % No-load losses in W

Sb_50 = Sn_50/3;         % Base values used for the simulation
Fb_50 = V1*sqrt(2)/(2*pi*f);
IexcB_50 = Sb_50*sqrt(2)/Ub1;
Ib1_50 = Sb_50/Ub1;
Zbase1_50 = Ub1/Ib1_50;
Lbase1_50 = Zbase1_50/(2*pi*f);

p0_50 = P0_50/Sb_50;     % Transformer parameters
R1_50 = Rcc_50/2;
R2_50 = R1_50;
L1_50 = (Xcc_50/2);
L2_50 = L1_50;
Rfe_50 = 1/p0_50;

%% Data Transformer 100 20

load('hysteresis_100.mat');

Sn_100 = 100e3;          % Nominal apparent power in VA
Rcc_100 = 1.75/100;       % Short-circuit resistance in pu
Xcc_100 = 3.60/100;      % Short-circuit reactance in pu
P0_100 = 145;            % No-load losses in W

Sb_100 = Sn_100/3;       % Base values used for the simulation
Fb_100 = V1*sqrt(2)/(2*pi*f);
IexcB_100 = Sb_100*sqrt(2)/Ub1;
Ib1_100 = Sb_100/Ub1;
Zbase1_100 = Ub1/Ib1_100;
Lbase1_100 = Zbase1_100/(2*pi*f);
```

```
p0_100 = P0_100/Sb_100; % Transformer parameters
R1_100 = Rcc_100/2;
R2_100 = R1_100;
L1_100 = (Xcc_100/2);
L2_100 = L1_100;
Rfe_100 = 1/p0_100;
%% Data Transformer 250 20

load('hysteresis_250.mat');

Sn_250 = 250e3;          % Nominal apparent power in VA
Rcc_250 = 1.3/100;       % Short-circuit resistance in pu
Xcc_250 = 3.78/100;      % Short-circuit reactance in pu
P0_250 = 300;            % No-load losses in W

Sb_250 = Sn_250/3;       % Base values used for the simulation
Fb_250 = V1*sqrt(2)/(2*pi*f);
IexcB_250 = Sb_250*sqrt(2)/Ub1;
Ib1_250 = Sb_250/Ub1;
Zbase1_250 = Ub1/Ib1_250;
Lbase1_250 = Zbase1_250/(2*pi*f);

p0_250 = P0_250/Sb_250; % Transformer parameters
R1_250 = Rcc_250/2;
R2_250 = R1_250;
L1_250 = (Xcc_250/2);
L2_250 = L1_250;
Rfe_250 = 1/p0_250;

%% Data Transformer 400 20

load('hysteresis_400.mat');

Sn_400 = 400e3;          % Nominal apparent power in VA
Rcc_400 = 1.15/100;       % Short-circuit resistance in pu
Xcc_400 = 3.83/100;      % Short-circuit reactance in pu
P0_400 = 430;            % No-load losses in W

Sb_400 = Sn_400/3;       % Base values used for the simulation
Fb_400 = V1*sqrt(2)/(2*pi*f);
IexcB_400 = Sb_400*sqrt(2)/Ub1;
Ib1_400 = Sb_400/Ub1;
Zbase1_400 = Ub1/Ib1_400;
Lbase1_400 = Zbase1_400/(2*pi*f);

p0_400 = P0_400/Sb_400; % Transformer parameters
R1_400 = Rcc_400/2;
R2_400 = R1_400;
L1_400 = (Xcc_400/2);
L2_400 = L1_400;
Rfe_400 = 1/p0_400;

%% Data Transformer 630 20

load('hysteresis_630.mat');
```

```
Sn_630 = 630e3;          % Nominal apparent power in VA
Rcc_630 = 1.03/100;      % Short-circuit resistance in pu
Xcc_630 = 3.86/100;      % Short-circuit reactance in pu
P0_630 = 600;            % No-load losses in W

Sb_630 = Sn_630/3;       % Base values used for the simulation
Fb_630 = V1*sqrt(2)/(2*pi*f);
IexcB_630 = Sb_630*sqrt(2)/Ub1;
Ib1_630 = Sb_630/Ub1;
Zbase1_630 = Ub1/Ib1_630;
Lbase1_630 = Zbase1_630/(2*pi*f);

p0_630 = P0_630/Sb_630; % Transformer parameters
R1_630 = Rcc_630/2;
R2_630 = R1_630;
L1_630 = (Xcc_630/2);
L2_630 = L1_630;
Rfe_630 = 1/p0_630;

%% Battery Transformer Data

Sn_BAT = 2000e3;             % Batery nominal power in VA
V1_BAT = 400;                % Primary side voltage
V2_BAT = 20e3;               % Secondary side voltage

X_BAT = 5.93/100;            % Series inductance in pu.
R_BAT = 1.18/100;            % Series resistance in pu.
P0_BAT = 1250.5;             % No-load losses in W.
I0_BAT = 0.1/100;            % No-load current in pu.

p0_BAT = P0_BAT/(Sn_BAT);    % Base values used for the
simulation
Vb_BAT = V2_BAT/sqrt(3);
Ib_BAT = Sn_BAT/(sqrt(3)*V2_BAT);
Zb_BAT = Vb_BAT/Ib_BAT;
Lb_BAT = Zb_BAT/(2*pi*f);

RBAT = R_BAT*Zb_BAT;
LBAT = X_BAT*Lb_BAT;

R1_BAT = R_BAT/2;            % Battery transformer parameters
R2_BAT = R_BAT/2;
X1_BAT = X_BAT/2;
X2_BAT = X_BAT/2;
Rfe_BAT = 1/p0_BAT;
Xfe_BAT = 1/sqrt(I0_BAT^2-p0_BAT^2);
```

ANNEX III – IDMT CONFIGURATION MATLAB FILE

```
function [TT, OT] =
fcn(clk,Irms,CTpri,CTsec,PS,TMS,k,alpha,B,TDS) %k y alpha son
los pesos de la IDMT que dependen del tipo de relay

persistent RelayState TripTime OperatingTime PickupTime
% Local variables which value is maintained in between calls.

if isempty(RelayState)       % If RelayState has not been
    RelayState = 0;          % inizialized, RelayState goes
    TripTime = inf;          % to zero and the tripping and
    OperatingTime = inf;     % Operating time go to infinite
    PickupTime = 0;
end

CT = max(abs(Irms/(CTpri/CTsec)));
Pickup = (PS*0.25)*CTsec;            % PS is multiplied by 0.25
                                     % since the PS obtained from
                                     % Simulink goes from 1 to 8.

if (RelayState == 0)&&(CT > Pickup)
    PickupTime = clk;
    RelayState = 1;
end

if (RelayState == 1)
    if k == 0
        OperatingTime = TDS;
    else
        PMS = CT/Pickup;         % Calculate Plug Multiplier
        OperatingTime = ((k/((PMS^alpha)-1))+B)*(TMS*0.05);
        % Determine Definite Inverse Minimum Time
    end
end

if (RelayState == 1)
    if (OperatingTime > 0)&&(clk > (PickupTime+OperatingTime))
    TripTime = PickupTime + OperatingTime;
    RelayState = 2;
    elseif(OperatingTime < 0)
    RelayState = 0;
    end
end

TT = TripTime;
if (OperatingTime > 0)
OT = OperatingTime;
else
OT = inf;
end
```